UNIVERSITY OF CANTERBURY

Department of Physics and Astronomy

CHRISTCHURCH NEW ZEALAND


# Supersymmetric Dark Matter in IceCube

by

Hamish Silverwood

MSc Thesis

# Supersymmetric Dark Matter in IceCube

Hamish G. M. Silverwood

MSc Thesis 2010-2012
Supervisors: Prof. Jenni Adams & Dr Anthony Brown

## Abstract

The Minimally Supersymmetric Standard Model (MSSM) provides us with a WIMP dark matter candidate particle, the neutralino. Neutralinos from the dark matter halo can potentially become captured by the sun and concentrated in the core, where they can undergo self-annihilation and so produce a distinct neutrino signal. The IceCube Neutrino Observatory has the potential to detect this neutrino signal and thus give indirect evidence of the presence and properties of neutralino dark matter. Although the full, unconstrained MSSM has 105 parameters this can be reduced to 25 parameters by the application of physically motivated assumptions. Scans of this MSSM-25 parameter space are conducted using the `DarkSUSY` software package and an adaptive scanning technique based on the Monte-Carlo VEGAS algorithm. The IceCube exclusion confidence level is then calculated for a set of points produced by these scans. Results indicate that the detection capability of IceCube exceeds that of current direct detection methods in certain regions of the parameter space. The use of a 25 dimensional parameter space reveals that there are new regions of observables with high exclusion confidence levels compared to earlier simulations performed with a seven dimensional parameter space.

# Contents

# List of Figures

# List of Tables

.

# Chapter 1

# Introduction

Supersymmetric dark matter lies at the intersection of questions regarding the very big and the very small. Observations of the universe indicate that the majority of matter consists not of the regular, luminous matter that we are made of but instead is made up of *dark matter*. Evidence indicates that it only interacts via the weak and gravitational forces, and is thus 'dark' because it does not interact with photons. Supersymmetry came about as a solution to problems at the very small scale of particle physics and happens to supply a candidate for dark matter, known as the *neutralino*.

Supersymmetry comes in many different versions, but this research focuses on just one, the Minimally Supersymmetric Standard Model (MSSM). The full MSSM has 105 free parameters, but through the judicious application of informed assumptions this number can be reduced. In this research we focus on a version of the MSSM with 25 free parameters, unsurprisingly known as the MSSM-25.

The aim of this research is to explore the MSSM-25 parameter space from the perspective of indirect dark matter detection with the IceCube Neutrino Observatory. This method of dark matter detection aims to observe the neutrinos produced by concentrations of neutralino dark matter in the sun. Previous analyses have utilised only the four parameter Constrained MSSM (CMSSM) [78], the seven parameter MSSM-7 [84], or the 19 parameter phenomenological MSSM (pMSSM) [19]. One goal of this research is to make a comparison between the MSSM-25 and the MSSM-7; the MSSM-7 is chosen for comparison because there is a data base of points available which was produced via similar methods to those used in this research.

## 1.1 Outline

We begin in Chapter 2 by describing the observational evidence for dark matter and the restrictions imposed by these observations upon its properties. The need for dark matter first became apparent in the 1930s from observations of galaxy clusters. Further evidence mounted from galactic rotation curves, large scale structure formation, the abundance of certain elements in the universe and gravitational lensing. Strong evidence and precise limits on the density of dark matter in the universe came from observations of the Cosmic Microwave Background by the Wilkinson Microwave Anisotropy Probe. Finally we present an outline of potential dark matter candidates.

The small end of the scale is described in Chapter 3, where we introduce Supersymmetry (SUSY). The Standard Model serves as the foundation for SUSY, and so it is outlined first. The math-

ematical framework of SUSY is then discussed, followed by a more focused look at the MSSM, its particle content and mass spectrum. We then describe the assumptions used to reduce the full set 105 parameters down to 25. The chapter is concluded by a discussion on how SUSY supplies a dark matter candidate particle.

Chapter 4 explains the methods by which we aim to detect dark matter. The first broad class of methods is indirect detection, under which comes detection with IceCube. We first describe the process by which neutralinos accumulate in the sun and produce a neutrino signal, followed by a description of the IceCube detector itself. Other indirect detection methods are also discussed. The second part of Chapter 4 covers direct detection methods, where the aim is to observe the interaction of a dark matter particle with the detector itself.

In Chapter 5 we introduce the statistical tools we will use to analyse our simulations. We begin with an overview of frequentist and Bayesian statistics, and then construct the equations we will use to calculate exclusion confidence levels for the points of the parameter space.

The computational details of the simulations we perform are described in Chapter 6. We describe the `DarkSUSY` package used for this research and the modifications required to make it compatible with 25 parameter models. The algorithm we use to select points in the parameter space is introduced, followed by a description of the FORTRAN programme that is built around it, `adscan_mssm25`. Finally, details of the simulations that were run are given.

Finally, in Chapter 7, the results of the simulations are analysed, and in Chapter 8 the conclusion of the thesis is presented.

Note: this version includes limited additions and corrections incorporated after submission and marking. Regarding Chapter 5 the reader is referred to [72] for a more complete treatment.

# Chapter 2

# Dark Matter

Dark matter is a broad term that encompasses matter whose existence we can infer through its gravitational effects but cannot yet detect and identify using direct observations. It can be subdivided into two classes: baryonic and non-baryonic dark matter. Baryonic dark matter is made up of baryons (e.g. protons and neutrons) and includes such objects as cold failed stars and 'invisible' gas clouds. We understand the physics of the particles involved, but simply cannot see them. On the other hand, non-baryonic dark matter consists of particles whose exact nature is unknown and which are the products of new physics.

This chapter gives a brief outline of the evidence we have for the existence of dark matter and the constraints this evidence places on potential candidates.

## 2.1 The Need for Dark Matter

### 2.1.1 Galactic Motion

The first indication of unseen mass came from Fritz Zwicky in 1933. His measurements of the velocities of galaxies in the Virgo and Coma clusters showed there was insufficient stellar mass within the galaxies to provide the gravitational pull necessary to hold the clusters together [87; 88]. In other words, if galaxies contained nothing but stars then the galaxy clusters should have been flung apart long ago. These observations implied that the amount of unseen matter, now christened *dark matter*, would have to exceed the amount of luminous matter by at least ten times [24].

Further evidence for missing mass comes from observations of galactic rotations. In short the matter we can see is insufficient to provide the gravitational attraction necessary to hold the galaxy together [67; 68]. The outer stars are rotating at such a high velocity, that if it were not for additional, unseen mass, they would decouple from the galaxy and move off into the inter-galactic void. Observations can also be made using 21-cm wavelength radio emissions from the neutral hydrogen that lies beyond the optically visible part of the galaxy; the circular velocity of this hydrogen is also abnormally high [24]. These rotational anomalies were first noted by Horace Babcock in 1939, and further evidence mounted until by the 1970s it was accepted that it was impossible to explain the observed galactic rotations using only the known stellar populations [24].

When circular velocity data is plotted against radial distance to give *rotation curves*, as is done so for the M33 dwarf spiral galaxy in Figure 2.1, a flat relationship is found at large distances, in contrast to a rise and decline as predicted by models incorporating only luminous matter and

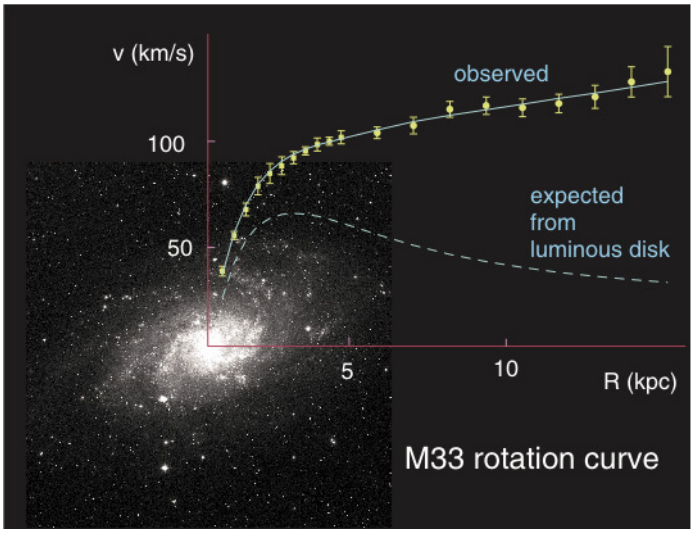


Figure 2.1: Rotation Curve for the M33 dwarf spiral galaxy. Image from [9].

Newtonian gravity. Newtonian dynamics predicts the circular velocity to be

$$v(r) = \sqrt{\frac{GM(r)}{r}} \qquad \text{where} \qquad M(r) \equiv 4\pi \int \rho(r) r^2 \mathrm{d}r \tag{2.1}$$

and $\rho(r)$ is the mass density profile. If we consider only luminous matter then $v(r)$ should drop at a rate proportional to $1/\sqrt{r}$ beyond the optical disc. However $v(r)$ is constant, implying the existence of a spherical halo with $M(r) \propto r$ and $\rho \propto 1/r^2$ [11].

### 2.1.2 Cosmology and the Evolution of the Universe

#### Structure Formation

We have seen that dark matter is necessary to explain the motion of galaxies and galaxy clusters, but it is also necessary for the development of even larger structures. Galaxy clusters are arranged into a sponge-like structure of filaments and walls surrounding large voids [53]. This large scale structure has been revealed by surveys of the universe, such as the 2-degree Field Galaxy Redshift Survey [17] and the Sloan Digital Sky Survey [76]. These structures have their origin in irregularities in the matter distribution of the early universe. Regions with a higher density of matter will exert a greater gravitational pull and draw more matter inwards. Density will increase and thus so will gravitational attraction, pulling yet more matter in [53]. Simulations of this structure formation demonstrate a need for large amounts of dark matter, the bulk of which must be *cold* (non-relativistic) and *non-dissipative* (i.e. it does not dissipate energy at a high rate). If the dark matter is cold it can clump together on small scales under the influence of gravity and thus seed galaxy formation. If it is non-dissipative it will not collapse with the normal luminous matter and produce galactic discs that are larger and more abundant than those we observe [69].

These requirements from structure formation give us the first inkling that baryonic dark matter cannot solve our missing mass problems on its own; it is made up of the same type of particles, baryons, and as luminous matter, so does not have the necessary properties for structure formation. The non-dissipative requirement implies that any non-baryonic dark matter candidate particle must have no interactions of electromagnetic strength or above. Any such interactions would result in excessive amounts of energy being lost by the dark matter to luminous matter

and photon radiation, causing the dark matter to collapse inwards and form disks along with the luminous matter [69]. This would cause problems not only with structure formation but also the spherical halo of dark matter necessary for correct galactic rotation curves.

Data from recent surveys of large scale structure indicates a total matter density, that is the density of luminous and dark matter combined, of $\Omega_{\rm m} \approx 0.29$ [62], where $\Omega_x = \frac{\rho_x}{\rho_{\rm c}}$ for some component $x$ of the universe. $\rho_c$ is the critical density, defined as

$$\rho_c = \frac{3H^2}{8\pi G}, \tag{2.2}$$

where $H$ is the Hubble parameter and $G$ is the gravitational constant [53].

### Big Bang Nucleosynthesis

According to the Big Bang model, once the universe had cooled to a temperature on the order of a MeV, protons and neutrons fused to form the nuclei of light elements. This process is known as Big Bang Nucleosynthesis (BBN). By measuring the abundances of these light elements in the early universe we can get an estimate of the total amount of baryonic matter present in the universe. This gives us an independent measure of $\Omega_{\rm b}$, the baryonic matter density parameter of the universe, which we can use to bolster our estimates of the $\Omega_{\rm DM}$, the non-baryonic dark matter density parameter of the universe, supplied by structure formation data. Results from BBN give $\Omega_{\rm b} \approx 0.04$ [46] and combining this with the total matter density $\Omega_m \approx 0.29$, derived from large scale structure formation, we can conclude that the density of dark matter is $\Omega_{\rm DM} \approx 0.25$. Thus the baryonic matter that we and our world are made of, far from being 'normal matter', is comparatively rare and special.

### Cosmic Microwave Background Anisotropies

For a period of time the early universe was dense enough to consist of an ionised plasma, a sea of free nuclei and electrons with photons of energy sufficient to ionise any atoms that might form. The photons interacted strongly with the electrons via Thompson scattering, and so the mean free path of any photon was short. The universe was opaque - photons could not travel long distances without being scattered. However as the universe expanded and cooled the photon energy dropped below the ionization energy and atoms began to form. Without free electrons to scatter off the photons could now travel large distances unimpeded. This process is known as recombination, and the last photons scattered off the ionized plasma are still travelling through the universe today. Since their emission the universe has expanded further resulting in them cooling to microwave energies [53]. This is the Cosmic Microwave Background (CMB), first detected in 1965 by Penzias and Wilson [61].

The CMB is very smooth and isotropic, with fractional irregularity in the temperature being [53]

$$\frac{\delta T}{T} \sim 10^{-5}. \tag{2.3}$$

However the anisotropies that do exist yield a wealth of information. Taking the power spectrum of the temperature shows a series of peaks and troughs, which are the product of acoustic oscillations in the ionized plasma just before decoupling takes place. By analysing the size and position of these peaks and troughs we can derive very precise measurements of the baryonic and non-baryonic matter densities [45]. The 7-year Wilkinson Microwave Anisotropy Probe results give $\Omega_{\rm b} = 0.0455 \pm 0.0028$ and $\Omega_{\rm DM} = 0.228 \pm 0.027$ [51], figures that are in excellent agreement

with those derived from structure formation and BBN.

For this research we work with a slightly different parameter derived from WMAP results, namely the dark matter relic density, which is the dark matter density multiplied by the dimensionless Hubble constant $h$ (defined as $H_0 = 100h$ km s$^{-1}$Mpc$^{-1}$) squared. The 7-year WMAP measurements [51] give

$$\Omega_{\mathrm{DM}} h^2 = 0.1120 \pm 0.0056. \tag{2.4}$$

### 2.1.3 Gravitational Lensing

Under general relativity concentrations of mass cause the surrounding space to distort, which in turn causes passing light rays to bend. Given the right geometry this can cause light from distant sources to be focused towards an observer by intermediate concentrations of mass, making the source appear brighter than it otherwise would. This *graviational lensing* can be caused by both luminous and dark matter [56], and so gives us another avenue for the observation of dark matter.

The presence of intermediate concentrations of dark matter can be inferred by comparing the strength of the gravitational lensing of a distant source to the known concentration of intermediate luminous matter. Several studies based on this method confirm the presence of dark matter and give details on its distribution [56; 80].

Observations of the galaxy cluster 1E 0657-558, better known as the Bullet Cluster, give spectacular evidence for dark matter through weak gravitational lensing [16]. The Bullet Cluster is the result of a collision between two clusters. The intracluster plasmas associated with each cluster, shown in pink in Figure 2.2, have collided and exerted friction on each other, giving the right hand plasma cloud its bullet shape. However the weakly interacting dark matter halos, shown in blue and detected through gravitational lensing, have passed through each other essentially undisturbed.

### 2.1.4 Dark Energy

The standard model of cosmology is known as the *Lambda*-CDM model. The 'CDM' is the Cold Dark Matter component of the universe discussed above. The $\Lambda$ refers to the apparent accelerating expansion of the universe shown by measurements of Type IA supernovae [66; 58]. In the $\Lambda$-CDM model is acceleration is explained invoking the existence of *dark energy*, whose exact nature is left undefined. For this research we assume the $\Lambda$-CDM model.

The presence of dark energy is, however, by no means certain; there are alternative cosmological models where the acceleration of the universe is an observational effect due to the inhomogeneous structure of the universe [85; 86].

## 2.2 Dark Matter Candidates

In gathering evidence for dark matter we have also placed limits on what its properties can be. Results from the WMAP satellite show that non-baryonic matter in the universe outweighs baryonic matter by five to one, and searches for baryonic dark matter objects such as MACHOs (Massive Astrophysical Compact Halo Objects) in galaxies limit their contribution to the halo mass to less than 20% [74], leading us to conclude that the vast majority of dark matter in non-baryonic. Henceforth the label 'dark matter' will apply only to non-baryonic dark matter.

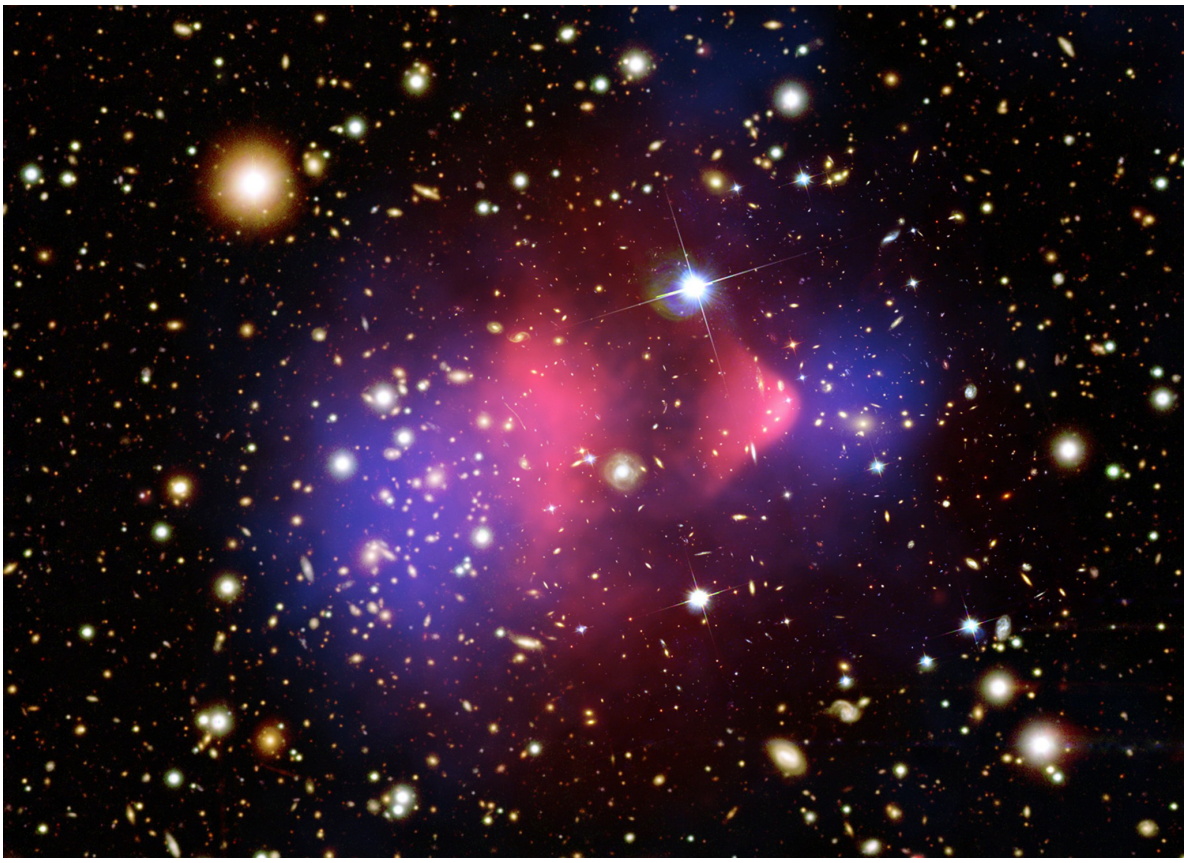

Figure 2.2: Composite image of the Bullet Cluster, showing the dark matter lensing mass in blue and the X-ray emitting intracluster plasma in pink. X-ray data: NASA/CXC/CfA/[54]; Lensing Map: NASA/STScI; ESO WFI; Magellan/U.Arizona/[16]; Optical: NASA/STScI; Magellan/U.Arizona/[16]

Standard model neutrinos were initially suggested as a possible dark matter candidate, however due to their relativistic speeds they cannot be considered 'cold' and their utilization as dark matter would prevent the formation of galaxies [24]. Moreover, analysis of CMB anisotropies combined with large-scale structure data suggests a neutrino relic density in the universe of $\Omega_\nu h^2 < 0.0067$ [11], far below the necessary dark matter relic density.

The most promising class of candidates are known as Weakly Interacting Massive Particles (WIMPs). These particles interact with Standard Model particles only via the weak force (and gravity) and are by definition non-baryonic and electrically neutral. The term WIMP applies to a general phenomenological class rather than a specific particle though. Specific theoretical examples of WIMPs include additional heavy Higgs bosons [8] and particles arising from Kaluza-Klein theories, where Standard Model particles are allowed to propagate into one or more compact extra dimensions [73]. Another WIMP candidate arises out of supersymmetry, which posits the existence of an entirely new class of particles called the *superparticles*, or *sparticles* for short. In the next chapter we explore this theory in greater depth and investigate the WIMP dark matter candidate it produces, the *Lightest Supersymmetric Particle*.

# Chapter 3

# Supersymmetry

The Standard Model (SM) has been our guide to particle physics since its genesis in the 1970s. It describes a menagerie of fundamental particles and the interactions between them. Although it has proved to be a remarkably accurate theory there are still holes and problems, and as will be described, the solution to these difficulties is the motivation behind Supersymmetry.

We begin by outlining the Standard Model, the particles it contains and the problems it has. The basic theory of Supersymmetry is then introduced, followed by a description of the Minimally Supersymmetric Standard Model and its phenomenology.

## 3.1 The Standard Model

There are three fundamental interactions between the SM particles; in decreasing order of strength they are the strong force, the electromagnetic force, and the weak force. The latter two unify into a single electroweak force above a certain energy threshold - this will be discussed in greater detail in Subsection 3.1.1. One glaring omission from the forces described by the SM is gravity. There is currently no workable theory of quantum gravity and so it cannot be incorporated into the SM. However gravity is far too weak to give measurable contributions at energies currently attainable by experiment.

The two main groups of fundamental particles described by the SM are the fermions, which have a half integer spin and the bosons, which have integer spin. The fermions of the SM all have spin of $1/2$, and can be further subdivided into leptons, which interact via the electromagnetic and weak forces, and the quarks, which interact via the electromagnetic, weak and strong forces. The first generation of the lepton group consists of the electron, $e^-$, and the electron neutrino, $\nu_e$. The quark group consists of the up quark, $u$, and the down quark, $d$. This pattern of two leptons and two quarks is replicated twice, each at higher masses. The second generation consists of the muon, $\mu$, the muon neutrino, $\nu_\mu$, the charm quark, $c$, and the strange quark, $s$, while the third generation consists of the tau, $\tau$ (also known as the tauon), the tau neutrino, $\nu_\tau$, the top quark, $t$, and the bottom quark, $b$.

The other major category of SM particles are the integer spin bosons. Within this group there are the spin-1 gauge bosons and the spin-0 Higgs bosons. The gauge bosons are the force carrier particles; they are the quanta of the fields that produce interactions in the SM. The strong force is carried by the gluons $g$, the weak force by the $W^\pm$ and $Z^0$ bosons, and the electromagnetic force by photon, $\gamma$.

| | Leptons | | Quarks | |
|---|---|---|---|---|
| First Generation | $e^-$ | $\nu_e$ | $u$ | $d$ |
| Second Generation | $\mu^-$ | $\nu_\mu$ | $c$ | $s$ |
| Third Generation | $\tau^-$ | $\nu_\tau$ | $t$ | $b$ |

Table 3.1: Standard Model Fermions

The organization the SM brings to the myriad of particles has its mathematical underpinnings in group theory. The gauge bosons, and hence the interactions, are described by the symmetry group

$$SU_c(3) \times SU_L(2) \times U_Y(1). \tag{3.1}$$

The eight generators of $SU_c(3)$ are associated with the eight gluons; the subscript $c$ denotes *colour*, and by itself $SU_c(3)$ is the basis of Quantum Chromodynamics (QCD), the theory of strong interactions. The $SU_L(2) \times U_Y(1)$ part describes the electroweak sector, the unification of electromagnetic and weak interactions, and its four generators, $W^a_\mu$ $(a = 1, 2, 3)$ from the $SU_L(2)$ part and $B_\mu$ from the $U_Y(1)$ part, are the ingredients from which the familiar $W^\pm$, $Z^0$ and $\gamma$ bosons are made. The way in which the fermions interact with each of these groups defines how it interacts with the forces themselves. For instance, any particle that transforms under the action of $SU_c(3)$ group operators couples with the gluons and is said to have a $SU_c(3)$ charge, more commonly known as a colour. If a particle does not transform under the action of a $SU_c(3)$ operator it is uncoloured and does not interact via the strong force.

The subscript L on the $SU_L(2)$ group is indicative of SM features that will be important in latter discussions. Fermions have an inherent property known as *chirality*, taking on one of two values: left (handed) or right (handed). Quarks and charged leptons and their respective antiparticles can be either left or right, but in the SM neutrinos can only be left handed and antineutrinos only right handed. Right handed neutrinos (or left handed antineutrinos) have yet to be detected and are absent from the SM but feature in several theoretical extensions to the standard model, such as models involving the see-saw mechanism and sterile neutrinos [36].

The subscript L denotes that only left handed fermions transform under the action of $SU_L(2)$ [14] and thus only left handed fermions couple to the $SU(2)_L$ gauge bosons [63]. This is achieved by grouping the left handed leptons and quarks of each generation into $SU_L(2)$ *doublets* while leaving the right handed leptons and quarks remain as $SU_L(2)$ *singlets* [63]. For example, in the first generation we would have two doublets,

$$E_L = \begin{pmatrix} \nu_e \\ e^-_L \end{pmatrix} \qquad \text{and} \qquad Q_L = \begin{pmatrix} u_L \\ d_L \end{pmatrix} \tag{3.2}$$

and three singlets

$$e^-_R \qquad u_R \qquad d_R. \tag{3.3}$$

As there are only left handed neutrinos in the Standard Model we drop the L subscript on the neutrino.

### 3.1.1 Electroweak Unification and the Higgs Mechanism

The mathematical structure given above assumes the unification of the electromagnetic and weak forces; $SU_L(2) \times U_Y(1)$ describes the unified electroweak sector, not the separate electro-

magnetic and weak sectors. The process of going from the unified electroweak theory to distinct weak and electromagnetic theories breaks the $SU_L(2) \times U_Y(1)$ symmetry group to the $U_{EM}(1)$ electromagnetic symmetry group, and is known as the Higgs mechanism. It gives mass to three of the gauge bosons, $W^{\pm}$ and $Z^0$, but the photon $\gamma$ remains massless as its $U_{EM}(1)$ gauge symmetry remains unbroken.

Above a certain energy level, the *electroweak scale*, the gauge group $SU_L(2) \times U_Y(1)$ remains unbroken. Its four generators, $W^a_\mu$ $(a = 1, 2, 3)$ and $B_\mu$, are associated with four massless bosons [14]. As we descend in energy the symmetry is broken. In general symmetry breaking of this kind is called *spontaneous symmetry breaking*.

The exact process by which this symmetry is broken is known as the Higgs mechanism. A full description of the Higgs mechanism is beyond the scope of this thesis but a number of details are relevant. As part of the Higgs mechanism another boson is introduced, called the Higgs boson. In contrast to the other bosons, it is a spin-0 particle. It is represented by a single complex scalar doublet (left) with a complex conjugate (right) [3; 7]:

$$\phi = \begin{pmatrix} \phi^+ \\ \phi^0 \end{pmatrix}, \qquad \phi_{\mathbf{C}} \equiv \mathrm{i}\tau_2 \phi^{\dagger T} = \begin{pmatrix} \bar{\phi}^0 \\ -\phi^- \end{pmatrix} \tag{3.4}$$

where $\tau_2$ is the second Pauli matrix.

In the process of applying the Higgs mechanism the charged bosons $W^1_\mu$ and $W^2_\mu$ from $SU_L(2)$ become the $W^+$ and $W^-$ bosons, while the neutral boson $W^3_\mu$ from $SU(2)_L$ mixes with the neutral boson $B_\mu$ from $U_Y(1)$ to produce the $Z^0$ boson and the photon $\gamma$. The mixing is described by the the following mixing matrix [26]:

$$\begin{pmatrix} W^3_\mu \\ B_\mu \end{pmatrix} = \begin{pmatrix} \cos\theta_W & \sin\theta_W \\ -\sin\theta_W & \cos\theta_W \end{pmatrix} \begin{pmatrix} Z^0_\mu \\ A_\mu \end{pmatrix} \tag{3.5}$$

where $\theta_W$ is the Weinberg angle (also known as the electroweak mixing angle) and $A_\mu$ is the electromagnetic field, the quanta of which is the photon $\gamma$. The energy at which electroweak unification occurs is currently unknown, but it is expected to be around the Fermi scale of $\approx 246$ GeV [49]. Later discussions will rely upon the distinction between unbroken and broken electroweak symmetry as we can see that the SM particle content is dependent on whether we are above or below the electroweak scale.

### 3.1.2 Problems with the Standard Model

The Standard Model has several limitations, but one in particular, the *hierarchy problem*, serves as motivation for Supersymmetry. In order for the Higgs mechanism to produce $W^{\pm}$ and $Z^0$ boson masses that fit with observations it must have a $(\text{mass})^2$ term on the order of $(100\text{GeV})^2$ [63]. However this mass can be pushed to much larger scales by contributions from radiative corrections, which are loops of other particles included in the middle of the Higgs boson propagator. The mass can be kept at the required level using only tools found in the Standard Model, but this requires parameters to be fine tuned to 33 decimal places [14]. Such an incredible level of fine tuning is considered highly unlikely, and so we look for theories that can restrain the $(\text{mass})^2$ term to the necessary level in a more robust and natural manner.

## 3.2 Basic SUSY Theory

The majority of Sections 3.2 and 3.3 follows [3], and references to the original sources can be found therein.

Supersymmetry posits the existence of a symmetry linking the two previously distinct groups of particles, the bosons and fermions. However if such a symmetry existed between the current set of Standard Model particles then its effects would have already been observed. Thus we have to introduce a new set of particles, the *superparticles* (or sparticles for short). For each SM fermion there is a *sfermion* superpartner, denoted by the fermion name with the prefix *s*. For each SM boson there is a *bosino* superpartner, denoted by the boson name with a suffix of *ino*. The only difference between a particle and its sparticle superpartner is spin; as one is fermionic and the other bosonic their spins will differ by one half. A sparticle will transform under the Standard Model gauge group $SU_c(3) \times SU_L(2) \times U_Y(1)$ in exactly the same manner as its particle partner. For instance, if a coloured particle will have a coloured superpartner, and both will transform in the same way under $SU_c(3)$.

As we do not see these sparticles amongst the spectrum of currently observed particles any supersymmetric theory we construct must also contain a mechanism by which supersymmetry is broken and the sparticles receive masses much greater than their SM partners [7]. Symmetries can be broken either by adding explicit symmetry breaking terms into the Lagrangian of the system, or by spontaneous symmetry breaking, an example of which is the symmetry breaking described by the Higgs mechanism (Subsection 3.1.1). The optimal way to introduce spontaneous symmetry breaking into supersymmetric theories is not agreed upon, but for practical applications one generally introduces explicit symmetry breaking terms which parameterise the low energy effects of the unidentified breaking mechanism, which is assumed to operate at a much higher energy scale.

The introduction of the sparticle superpartners offers a solution to the Hierarchy problem outlined in Subsection 3.1.2. Roughly speaking, for every radiative correction generated by a SM particle loop in the middle of the Higgs propagator, an equal and opposite radiative correction is generated by a loop of the corresponding sparticle. This mechanism restrains the Higgs mass without requiring high levels of fine tuning.

The mathematical foundation of Supersymmetry is the Super-Poincaré algebra. The regular Poincaré algebra is the basis of relativistic quantum field theories. It incorporates the six generators $M^{\mu\nu}$ of the Lorentz group, describing boosts and rotations, and the four generators $P^{\lambda}$ of the space-time translation group [7]. The algebraic structure is defined by the commutation relations between these generators; e.g. what the commutators $[P^{\lambda}, P^{\mu}]$, $[M^{\mu\nu}, P^{\lambda}]$, and $[M^{\mu\nu}, M^{\rho\sigma}]$ are equal to.

The Poincaré algebra is expanded to the super-Poincaré group by the addition of $N$ new supersymmetric generators $Q^A_\alpha$ $(A = 1, ..., N)$. These generators are inherently different from those of the Poincaré algebra because the algebraic structure between them is described by anti-commutators rather than commutators, and they are thus fermionic objects. The relations between supersymmetric generators and Poincaré generators is described by commutators though. So the structure of the super-Poincaré algebra is determined by the commutations relations for $[P^{\lambda}, P^{\mu}]$, $[M^{\mu\nu}, P^{\lambda}]$, and $[M^{\mu\nu}, M^{\rho\sigma}]$, $[P^{\mu}, Q^A_\alpha]$, $[M^{\mu\nu}, Q^A_\alpha]$, and the anti-commutation relations $\{Q^A_\alpha, Q^B_\beta\}$.

## 3.3 Minimally Supersymmetric Standard Model

As the name suggests, the Minimally Supersymmetric Standard Model takes the Standard Model, and adds the minimal amount of new physics in order to make it supersymmetric. It is an $N = 1$ supersymmetry theory [14], and so adds only one more generator to the Poincaré algebra.

### 3.3.1 Particle Content and Organization

Each standard model particle receives its own sparticle superpartner, and they are then organized into *supermultiplets*. The gauge bosons and their bosino superpartners form gauge supermultiplets, while the fermions and their sfermion superpartners form chiral supermultiplets (as the fermions are chiral, e.g. left and right handed.) We now work our way through the SM particle spectrum and discuss their respective superpartners.

#### Gauge Bosons and Bosinos

The supersymmetry breaking scale is expected to be considerably above the electroweak symmetry breaking scale [82], so we generally give superpartners to the $W^a_\mu$ and $B_\mu$ bosons of the unified electroweak sector rather than the $W^\pm$, $Z^0$ and $\gamma$ bosons. The gauge bosinos are collectively known as gauginos, and all have spin 1/2. The first gauge supermultiplet consists of the $W^a_\mu$ bosons and their superpartners $\tilde{W}^a_\mu$, and the second consists of the $B_\mu$ boson and its superpartner $\tilde{B}_\mu$. The $\tilde{W}^a_\mu$ gaugino is called a *wino* and $\tilde{B}_\mu$ is called a *bino*. The superpartner of the gluon $g$ is the *gluino* $\tilde{g}$, and together they make up the third gauge supermultiplet of the MSSM.

#### Higgs Bosons and Higgsinos

The use of the plural form in the title hints at the added complication we find in the Higgs sector of supersymmetric theories. In the standard model Yukawa interactions can involve both a field and its charge conjugate. However the Yukawa interactions in the MSSM cannot simultaneously involve both a complex scalar field $\phi$ and its hermitian conjugate $\phi^\dagger$ and preserve their invariance under SUSY. Thus we must replace the single Higgs doublet and its complex conjugate with two separate Higgs doublets to keep the MSSM Yukawa interactions SUSY-invariant. Each of these doublets receives its own spin 1/2 *Higgsino* superpartner doublet and we get two Higgs/Higgsino chiral supermultiplets, named $H_u$ and $H_d$:

$$H_u : \begin{pmatrix} H_u^+ \\ H_u^0 \end{pmatrix}, \begin{pmatrix} \tilde{H}_u^+ \\ \tilde{H}_u^0 \end{pmatrix} \qquad \text{and} \qquad H_d : \begin{pmatrix} H_d^0 \\ H_d^- \end{pmatrix}, \begin{pmatrix} \tilde{H}_d^0 \\ \tilde{H}_d^- \end{pmatrix} \tag{3.6}$$

As we shall see when we encounter an object called the *superpotential* in Subsection 3.3.2 the Higgs doublets $H_u$ and $H_d$ are denoted with subscripts $u$ and $d$ because they couple with up- and down-type supermultiplets respectively.

#### Charginos and Neutralinos

We now have four charged gauginos, $\tilde{W}^1_\mu$, $\tilde{W}^2_\mu$, $\tilde{H}_u^+$, and $\tilde{H}_d^-$, and four neutral gauginos, $\tilde{W}^3_\mu$, $\tilde{B}_\mu$, $\tilde{H}_u^0$, $\tilde{H}_d^0$. The former are called *charginos* and the latter *neutralinos*. The chargino gauge-eigenstates listed here mix amongst themselves to form mass eigenstates $\tilde{\chi}_1^\pm$, $\tilde{\chi}_2^\pm$, and similarly the neutralino gauge-eigenstates mix to form mass eigenstates $\tilde{\chi}_1^0$, $\tilde{\chi}_2^0$, $\tilde{\chi}_3^0$, and $\tilde{\chi}_4^0$. This mixing is described in further detail in Subsection 3.3.3.

**Leptons and Sleptons**

In the standard model we have right- and left-handed electrons, muons and taus, and a left handed neutrino for each generation. The superpartners of the leptons are collectively known as *sleptons* and are all spin-0 particles. Electrons, muons and taus have partners called *selectrons*, *smuons* and *staus* respectively, and the neutrino is paired with a *sneutrino*. The sleptons are spin-0 particles and so do not have helicity, meaning any left or right label is technically superfluous. However each lepton helicity state receives its own superpartner, so we retain the labeling to keep track of which slepton matches with which lepton.

The left-handed electrons, muons and taus each form an $SU_L(2)$ doublet with their respective neutrinos, and as supersymmetry preserves this structure, their superpartners will also be arranged into $SU_L(2)$ doublets. These doublets form the three left-type chiral supermultiplets:

$$L_1 : \quad \begin{pmatrix} \nu_{e\mathrm{L}} \\ e_{\mathrm{L}} \end{pmatrix}, \begin{pmatrix} \tilde{\nu}_{e\mathrm{L}} \\ \tilde{e}_{\mathrm{L}} \end{pmatrix} \tag{3.7}$$

$$L_2 : \quad \begin{pmatrix} \nu_{\mu\mathrm{L}} \\ \mu_{\mathrm{L}} \end{pmatrix}, \begin{pmatrix} \tilde{\nu}_{\mu\mathrm{L}} \\ \tilde{\mu}_{\mathrm{L}} \end{pmatrix} \tag{3.8}$$

$$L_3 : \quad \begin{pmatrix} \nu_{\tau\mathrm{L}} \\ \tau_{\mathrm{L}} \end{pmatrix}, \begin{pmatrix} \tilde{\nu}_{\tau\mathrm{L}} \\ \tilde{\tau}_{\mathrm{L}} \end{pmatrix}. \tag{3.9}$$

The right-handed electrons, muons and taus could simply be arranged into chiral supermultiplets with their respective superpartners, but the Lagrangian machinery outlined in Subsection 3.3.2 below is developed in terms on left-type supermultiplets. So to mould these right-type supermultiplets into this framework we view them instead as the charge conjugates of left-type antiparticle fields:

$$\bar{e}_1 : \quad \bar{e}_L = (e_R)^c, \;\; \tilde{\bar{e}}_L = \tilde{e}_R^\dagger \tag{3.10}$$

$$\bar{e}_2 : \quad \bar{\mu}_L = (e_R)^c, \;\; \tilde{\bar{\mu}}_L = \tilde{\mu}_R^\dagger \tag{3.11}$$

$$\bar{e}_3 : \quad \bar{\tau}_L = (e_R)^c, \;\; \tilde{\bar{\tau}}_L = \tilde{\tau}_R^\dagger. \tag{3.12}$$

**Quarks and Squarks**

The supersymmetric partners of the quarks are the *squarks*; *sup*, *sdown*, *scharm*, *sstrange*, *stop* and *sbottom* squarks for the up, down, charm, strange, top and bottom quarks respectively. Just as with the lepton and slepton case above the $SU_L(2)$ doublet structure of the quarks is preserved in the squarks. So we have three left-type chiral supermultiplets:

$$Q_1 = \begin{pmatrix} u_{\mathrm{L}} \\ d_{\mathrm{L}} \end{pmatrix}, \begin{pmatrix} \tilde{u}_{\mathrm{L}} \\ \tilde{d}_{\mathrm{L}} \end{pmatrix} \tag{3.13}$$

$$Q_2 = \begin{pmatrix} c_{\mathrm{L}} \\ s_{\mathrm{L}} \end{pmatrix}, \begin{pmatrix} \tilde{c}_{\mathrm{L}} \\ \tilde{c}_{\mathrm{L}} \end{pmatrix} \tag{3.14}$$

$$Q_3 = \begin{pmatrix} t_{\mathrm{L}} \\ b_{\mathrm{L}} \end{pmatrix}, \begin{pmatrix} \tilde{t}_{\mathrm{L}} \\ \tilde{b}_{\mathrm{L}} \end{pmatrix}, \tag{3.15}$$

and six right-type chiral supermultiplets, represented as the charge conjugates of left-type supermultiplets, just as with the right-type leptons.

$$\bar{u}_1: \quad \bar{u}_L = (u_R)^c, \;\; \tilde{\bar{u}}_L = \tilde{u}_R^\dagger \tag{3.16}$$

$$\bar{d}_1: \quad \bar{d}_L = (d_R)^c, \;\; \tilde{\bar{d}}_L = \tilde{d}_R^\dagger \tag{3.17}$$

$$\bar{u}_2: \quad \bar{c}_L = (c_R)^c, \;\; \tilde{\bar{c}}_L = \tilde{c}_R^\dagger \tag{3.18}$$

$$\bar{d}_2: \quad \bar{s}_L = (s_R)^c, \;\; \tilde{\bar{s}}_L = \tilde{s}_R^\dagger \tag{3.19}$$

$$\bar{u}_3: \quad \bar{t}_L = (t_R)^c, \;\; \tilde{\bar{t}}_L = \tilde{t}_R^\dagger \tag{3.20}$$

$$\bar{d}_3: \quad \bar{b}_L = (b_R)^c, \;\; \tilde{\bar{b}}_L = \tilde{b}_R^\dagger. \tag{3.21}$$

### 3.3.2 Elements of the MSSM Lagrangian

The MSSM has many free parameters, and the overall goal of this research is exploration of this parameter space. We now introduce the elements of the MSSM Lagrangian that contain these parameters. These are the superpotential and the soft SUSY breaking terms. A full derivation of the MSSM Lagrangian can be found in [3] and [50].

The *superpotential* $W$ is used in constructing the interaction Lagrangian, and for the MSSM it is defined as

$$W = y_{\mathrm{u}}^{ij}\bar{u}_i Q_j \cdot H_{\mathrm{u}} - y_{\mathrm{d}}^{ij}\bar{d}_i Q_j \cdot H_{\mathrm{d}} - y_{\mathrm{e}}^{ij}\bar{e}_i L_j \cdot H_{\mathrm{d}} + \mu H_{\mathrm{u}} \cdot H_{\mathrm{d}} \tag{3.22}$$

where $y_{\mathrm{u}}^{ij}$, $y_{\mathrm{d}}^{ij}$, and $y_{\mathrm{e}}^{ij}$ are the $3 \times 3$ SM Yukawa coupling matrices, and $\mu$ is the coupling parameter between the two Higgs supermultiplets. $\mu$ is the first of our MSSM parameters.

The remainder of the MSSM parameters come from the explicit soft supersymmetry breaking terms which we use to parameterise the low energy effects of the unknown, high energy supersymmetry breaking mechanism. 'Soft' means that the terms added do not introduce new divergences into the model which could potentially prevent the MSSM from solving the hierarchy problem [3]. The soft SUSY breaking terms are:

$$\mathcal{L}_{\mathrm{soft}} = -\frac{1}{2}\left(M_1 \tilde{B} \cdot \tilde{B} + M_2 \tilde{W}^a \cdot \tilde{W}^a + M_3 \tilde{g}^a \cdot \tilde{g}^a + \mathrm{h.c.}\right) \qquad \text{Gaugino Masses} \tag{3.23}$$

$$- m_{\tilde{Q}ij}^2 \tilde{Q}_i^\dagger \cdot \tilde{Q}_j - m_{\tilde{\mathrm{u}}ij}^2 \tilde{\bar{u}}_{\mathrm{L}i}^\dagger \tilde{\bar{u}}_{\mathrm{L}j} - m_{\tilde{\bar{d}}ij}^2 \tilde{\bar{d}}_{\mathrm{L}i}^\dagger \tilde{\bar{d}}_{\mathrm{L}j} \qquad \text{Squark Mass}^2 \text{ Terms} \tag{3.24}$$

$$- m_{\tilde{L}ij}^2 \tilde{L}_i^\dagger \cdot \tilde{L}_j - m_{\tilde{\bar{e}}ij}^2 \tilde{\bar{e}}_{\mathrm{L}i}^\dagger \tilde{\bar{e}}_{\mathrm{L}j} \qquad \text{Slepton Mass}^2 \text{ Terms} \tag{3.25}$$

$$- m_{H_{\mathrm{u}}}^2 H_{\mathrm{u}}^\dagger \cdot H_{\mathrm{u}} - m_{H_{\mathrm{d}}}^2 H_{\mathrm{d}}^\dagger \cdot H_{\mathrm{d}} - (bH_{\mathrm{u}} \cdot H_{\mathrm{d}} + \mathrm{h.c.}) \qquad \text{Higgs Mass}^2 \text{ Terms} \tag{3.26}$$

$$\begin{aligned} &- a_{\mathrm{u}}^{ij} \tilde{\bar{u}}_{\mathrm{L}i} \tilde{Q}_j \cdot H_{\mathrm{u}} + a_{\mathrm{d}}^{ij} \tilde{\bar{d}}_{\mathrm{L}i} \tilde{Q}_j \cdot H_{\mathrm{d}} + a_{\mathrm{e}}^{ij} \tilde{\bar{e}}_{\mathrm{L}i} \tilde{L}_j \cdot H_{\mathrm{d}} + \mathrm{h.c.} \\ &- c_{\mathrm{u}}^{ij} \tilde{\bar{u}}_{\mathrm{L}i} Q_j \cdot H_{\mathrm{d}}^\dagger + c_{\mathrm{d}}^{ij} \tilde{\bar{d}}_{\mathrm{L}i} \tilde{Q}_j \cdot H_{\mathrm{u}}^\dagger + c_{\mathrm{e}}^{ij} \tilde{\bar{e}}_{\mathrm{L}i} \tilde{L}_j \cdot H_{\mathrm{u}} + \mathrm{h.c.} \end{aligned} \qquad \text{Triple Scalar Couplings} \tag{3.27}$$

We can see that all the terms in Equations 3.23 - 3.27 explicitly break SUSY as they do not simultaneously involve both particle and superparticle, e.g. Equation 3.24 has squarks but no quarks. In Equation 3.27 we have two sets of trilinear coupling matrices, $\mathbf{a}_{\mathrm{u}}$, $\mathbf{a}_{\mathrm{d}}$, $\mathbf{a}_{\mathrm{e}}$ and $\mathbf{c}_{\mathrm{u}}$, $\mathbf{c}_{\mathrm{d}}$,

$\mathbf{c}_\mathrm{e}$. The latter set is generally omitted, with the couplings set to zero, as the couplings they describe are either absent or very small in many SUSY-breaking models.

This Lagrangian has a large number of free parameters and all but one appear exclusively in the soft SUSY breaking terms. In the gaugino sector of soft SUSY breaking we have three mass parameters, $M_1$, $M_2$, and $M_3$. The Higgs sector at first glance has four free parameters; $\mu$ from the superpotential Equation 3.22, and $m^2_{H_\mathrm{u}}$, $m^2_{H_\mathrm{d}}$, and $b$ from the soft SUSY breaking Higgs sector. However with the application of the MSSM Higgs mechanism (see Chapter 10 of [3]) this is reduced to three; $\mu$, $\tan\beta$, and $m_A$ where

$$\tan\beta = \frac{v_u}{v_d} \qquad \text{and} \qquad m_A = \sqrt{\frac{2b}{\sin 2\beta}}. \tag{3.28}$$

$v_u$ and $v_d$ are the vacuum expectation values acquired by the neutral components of the fields of the $H_u$ and $H_d$ supermultiplets respectively during the application of the Higgs mechanism.

The $3\times3$ sfermion mass parameter matrices[1] of Equations 3.24 and 3.25 are in general complex but must also be Hermitian so that the Lagrangian is real [3]. Thus each sfermion mass parameter matrix has a maximum of nine free parameters, giving us a total of 45 free parameters from the sfermion sector. The complex $3\times3$ triple scalar coupling matrices $\mathbf{a}_\mathrm{u}$, $\mathbf{a}_\mathrm{d}$, $\mathbf{a}_\mathrm{e}$, each have nine real and nine imaginary free parameters, yielding 54 in total from this sector. In all we now have 105 free parameters. Reducing this to a more manageable number will be discussed in Subsection 3.3.4.

### 3.3.3 Masses of the MSSM Sparticles

Here we give a brief outline of how the masses of the sparticles are calculated from the MSSM parameters. We follows [3] closely, and a more detailed derivation of the mass calculations can be found in Chapter 11 of this book.

#### Gluino Masses

Calculation of the gluino masses is the simplest case in the MSSM; as the gluino is the only colour octet fermion and the $SU(3)_c$ symmetry remains unbroken, the gluino cannot mix with any other MSSM particles. Its mass is generated by the soft SUSY breaking gluino mass term in Eq. 3.23:

$$\frac{1}{2}M_3\tilde{g}^a\cdot\tilde{g}^a + \text{h.c.} \tag{3.29}$$

So the resultant gaugino mass is the same as the initial parameter $M_3$;

$$M_{gluino} = M_3 \tag{3.30}$$

#### Neutralino Masses

If it were not for electroweak symmetry breaking (Section 3.1.1) we could, just as we did with the gluinos, simply read off the masses of the neutralinos from the soft SUSY breaking mass

[1] The use of 'mass parameter matrices' is important. The masses of individual particles is in general found by calculating the eigenvalues of the particle's mass matrix. As laid out in Subsection 3.3.3 the mass parameter matrices are not the same as the mass matrices; the former is part of the calculation of the latter. For clarity mass parameter matrices will be denoted with a lower case $\mathbf{m}$ while mass matrices will be denoted with an upper case $\mathbf{M}$.

terms of Equation 3.23 [3]:

$$-\frac{1}{2}M_1\tilde{B}\cdot\tilde{B}-\frac{1}{2}M_2\tilde{W}^0\cdot\tilde{W}^0 \tag{3.31}$$

However the Higgs mechanism produces bilinear combinations of one of $(\tilde{B},\tilde{W}^0)$ with one of $(\tilde{H}_u^0,\tilde{H}_d^0)$, and so creates off diagonal entries in the neutralino mass matrix. The mass matrix becomes

$$\mathbf{M}_{\tilde{G}^0}=\begin{pmatrix} M_1 & 0 & -c_\beta s_W m_Z & s_\beta s_W m_Z \\ 0 & M_2 & c_\beta c_W m_Z & -s_\beta c_W m_Z \\ -c_\beta s_W m_Z & c_\beta c_W m_Z & \delta_{33} & -\mu \\ s_\beta s_W m_Z & -s_\beta c_W m_Z & -\mu & \delta_{44} \end{pmatrix} \tag{3.32}$$

where $c_W=\cos\theta_W$, $s_W=\sin\theta_W$, $c_\beta=\cos\beta$, $s_\beta=\sin\beta$, and $m_Z$ is the mass of the $Z^0$ boson. $\delta_{33}$ and $\delta_{44}$ are radiative corrections that are important when two higgsinos have similar masses [37], with explicit expressions given in [23].

After diagonalizing the matrix of Equation 3.32 the diagonal entries (which are also the eigenvalues of the matrix) give expressions for the masses of each neutralino.

**Chargino Masses**

In a gauge-eigenstate basis defined by

$$\tilde{g}^+=\begin{pmatrix}\tilde{W}^+\\ \tilde{H}_{\mathrm{u}}^+\end{pmatrix} \tag{3.33}$$

$$\tilde{g}^-=\begin{pmatrix}\tilde{W}^-\\ \tilde{H}_{\mathrm{u}}^-\end{pmatrix} \tag{3.34}$$

the chargino mass term can be written as [3]

$$-\frac{1}{2}\left(\tilde{g}^{+T}\mathbf{M}_{\tilde{G}^\pm}^T\cdot\tilde{g}^-+\tilde{g}^{-T}\mathbf{M}_{\tilde{G}^\pm}\cdot\tilde{g}^+\right)+\text{h.c.} \tag{3.35}$$

where $\mathbf{M}_{\tilde{G}^\pm}$ is the chargino mass matrix:

$$\mathbf{M}_{\tilde{G}^\pm}=\begin{pmatrix} M_2 & \sqrt{2}s_\beta m_W \\ \sqrt{2}c_\beta m_W & \mu \end{pmatrix}. \tag{3.36}$$

To extract expressions for the chargino masses we must diagonalize the mass matrix. However $\mathbf{M}_{\tilde{G}^\pm}^T\neq\mathbf{M}_{\tilde{G}^\pm}$ (unless $\tan\beta=1$) and both are used in the mass term 3.35, so two distinct $2\times2$ matrices will be required. We start by defining the mass-eigenstate basis:

$$\tilde{\chi}^+=\begin{pmatrix}\tilde{\chi}_1^+\\ \tilde{\chi}_1^+\end{pmatrix}=\mathbf{V}\tilde{g}^+ \tag{3.37}$$

$$\tilde{\chi}^-=\begin{pmatrix}\tilde{\chi}_1^-\\ \tilde{\chi}_1^-\end{pmatrix}=\mathbf{U}\tilde{g}^- \tag{3.38}$$

where $\mathbf{U}$ and $\mathbf{V}$ are unitary $2\times2$ matrices. Substituting Equations 3.37 and 3.38 into Equation 3.35 gives us

$$-\frac{1}{2}\left(\tilde{\chi}^{+T}\mathbf{V}^*\mathbf{M}_{\tilde{G}^\pm}^T\mathbf{U}^\dagger\tilde{\chi}^-+\tilde{\chi}^{-T}\mathbf{U}^*\mathbf{M}_{\tilde{G}^\pm}\mathbf{V}^\dagger\tilde{\chi}^+\right). \tag{3.39}$$

To perform the diagonalization we set the right hand matrices as

$$\mathbf{U}^*\mathbf{M}_{\tilde{G}^\pm}\mathbf{V}^\dagger = \begin{pmatrix} m_{\tilde{\chi}_1^\pm} & 0 \\ 0 & m_{\tilde{\chi}_2^\pm} \end{pmatrix}. \tag{3.40}$$

Then note that for the left hand matrices

$$\left(\mathbf{V}^*\mathbf{M}^T_{\tilde{G}^\pm}\mathbf{U}^\dagger\right)^T = \mathbf{U}^*\mathbf{M}_{\tilde{G}^\pm}\mathbf{V}^\dagger \tag{3.41}$$

$$\therefore \quad = \mathbf{V}^*\mathbf{M}^T_{\tilde{G}^\pm}\mathbf{U}^\dagger \tag{3.42}$$

as $\mathbf{U}\mathbf{M}_{\tilde{G}^\pm}\mathbf{V}^\dagger$ is a diagonal matrix. Thus Equation 3.39 can be re-written as

$$-\frac{1}{2}\left(\tilde{\chi}^{+T}\mathbf{U}^*\mathbf{M}_{\tilde{G}^\pm}\mathbf{V}^\dagger\tilde{\chi}^- + \tilde{\chi}^{-T}\mathbf{U}^*\mathbf{M}_{\tilde{G}^\pm}\mathbf{V}^\dagger\tilde{\chi}^+\right). \tag{3.43}$$

The Hermitian conjugate of 3.40 is

$$\mathbf{V}\mathbf{M}^\dagger_{\tilde{G}^\pm}\mathbf{U}^T = \begin{pmatrix} m^*_{\tilde{\chi}_1^\pm} & 0 \\ 0 & m^*_{\tilde{\chi}_2^\pm} \end{pmatrix}. \tag{3.44}$$

Taking Equations 3.40 and 3.44 we can make the following combinations:

$$\mathbf{V}\mathbf{M}^\dagger_{\tilde{G}^\pm}\mathbf{U}^T\mathbf{U}^*\mathbf{M}_{\tilde{G}^\pm}\mathbf{V}^\dagger = \mathbf{V}\mathbf{M}^\dagger_{\tilde{G}^\pm}\mathbf{M}_{\tilde{G}^\pm}\mathbf{V}^\dagger = \begin{pmatrix} \left|m_{\tilde{\chi}_1^\pm}\right|^2 & 0 \\ 0 & \left|m_{\tilde{\chi}_2^\pm}\right|^2 \end{pmatrix} \tag{3.45}$$

$$\mathbf{U}^*\mathbf{M}_{\tilde{G}^\pm}\mathbf{V}^\dagger\mathbf{V}\mathbf{M}^\dagger_{\tilde{G}^\pm}\mathbf{U}^T = \mathbf{U}^*\mathbf{M}_{\tilde{G}^\pm}\mathbf{M}^\dagger_{\tilde{G}^\pm}\mathbf{U}^T = \begin{pmatrix} \left|m_{\tilde{\chi}_1^\pm}\right|^2 & 0 \\ 0 & \left|m_{\tilde{\chi}_2^\pm}\right|^2 \end{pmatrix}. \tag{3.46}$$

Thus we can see that positively charged states $\tilde{\chi}^+$ diagonalize $\mathbf{M}^\dagger_{\tilde{G}^\pm}\mathbf{M}_{\tilde{G}^\pm}$ and negatively charged states $\tilde{\chi}^-$ diagonalize $\mathbf{M}_{\tilde{G}^\pm}\mathbf{M}^\dagger_{\tilde{G}^\pm}$. As these matrices are equal to each other the mass of the chargino will not depend on whether it is positive or negative. We can extract the masses of the charginos by finding the eigenvalues of $\mathbf{M}^\dagger_{\tilde{G}^\pm}\mathbf{M}_{\tilde{G}^\pm}$ (or $\mathbf{M}_{\tilde{G}^\pm}\mathbf{M}^\dagger_{\tilde{G}^\pm}$). This gives us [3]

$$\left|m_{\tilde{\chi}_1^\pm}\right|^2 = \frac{1}{2}\left[\left(M_2^2 + |\mu|^2 + 2m_W^2\right) - \sqrt{\left(M_2^2 + |\mu|^2 + 2m_W^2\right)^2 - 4|\mu M_2 - m_W^2\sin 2\beta|^2}\right] \tag{3.47}$$

$$\left|m_{\tilde{\chi}_2^\pm}\right|^2 = \frac{1}{2}\left[\left(M_2^2 + |\mu|^2 + 2m_W^2\right) + \sqrt{\left(M_2^2 + |\mu|^2 + 2m_W^2\right)^2 - 4|\mu M_2 - m_W^2\sin 2\beta|^2}\right] \tag{3.48}$$

**Sfermion Masses**

For the squarks and sleptons we have the three $6 \times 6$ mass matrices:

$$\mathbf{M}^2_{\tilde{u}} = \begin{pmatrix} \mathbf{m}^2_{\tilde{Q}} + \mathbf{m}^\dagger_u \mathbf{m}_u + D^u_{LL}\mathbb{1}_3 & \mathbf{m}^\dagger_u \left(\mathbf{a}^\dagger_{\mathrm{u}} - \mu^* \cot\beta\right) \\ \left(\mathbf{a}_{\mathrm{u}} - \mu \cot\beta\right) \mathbf{m}_u & \mathbf{m}^2_{\tilde{\bar{u}}} + \mathbf{m}_u \mathbf{m}^\dagger_u + D^u_{RR}\mathbb{1}_3 \end{pmatrix}, \tag{3.49}$$

$$\mathbf{M}^2_{\tilde{d}} = \begin{pmatrix} \mathbf{K}^\dagger \mathbf{m}^2_{\tilde{Q}} \mathbf{K} + \mathbf{m}_d \mathbf{m}^\dagger_d + D^d_{LL}\mathbb{1}_3 & \mathbf{m}^\dagger_d \left(\mathbf{a}^\dagger_{\mathrm{d}} - \mu^* \tan\beta\right) \\ \left(\mathbf{a}_{\mathrm{d}} - \mu \tan\beta\right) \mathbf{m}_d & \mathbf{m}^2_{\tilde{\bar{d}}} + \mathbf{m}^\dagger_d \mathbf{m}_d + D^d_{RR}\mathbb{1}_3 \end{pmatrix}, \tag{3.50}$$

$$\mathbf{M}^2_{\tilde{e}} = \begin{pmatrix} \mathbf{m}^2_{\tilde{L}} + \mathbf{m}_e \mathbf{m}^\dagger_e + D^e_{LL}\mathbb{1}_3 & \mathbf{m}^\dagger_e \left(\mathbf{a}^\dagger_{\mathrm{e}} - \mu^* \tan\beta\right) \\ \left(\mathbf{a}_{\mathrm{e}} - \mu \tan\beta\right) \mathbf{m}_e & \mathbf{m}^2_{\tilde{\bar{e}}} + \mathbf{m}^\dagger_e \mathbf{m}_e + D^e_{RR}\mathbb{1}_3 \end{pmatrix}, \tag{3.51}$$

$$\tag{3.52}$$

and one $3 \times 3$ mass matrix:

$$\mathbf{M}^2_{\tilde{\nu}} = \mathbf{m}^2_{\tilde{L}} + D^\nu_{LL}\mathbb{1}_3, \tag{3.53}$$

where $K$ is the Cabibbo-Kobayashi-Maskawa (CKM) matrix, $\mathbf{m}_u = \mathrm{diag}(m_u, m_c, m_t)$, $\mathbf{m}_d = \mathrm{diag}(m_d, m_s, m_b)$, $\mathbf{m}_e = \mathrm{diag}(m_e, m_\mu, m_\tau)$ and

$$D^f_{LL} = m^2_Z \cos 2\beta \left(T_{3f} - e_f \sin\theta_w{}^2\right) \qquad \text{and} \qquad D^f_{RR} = -m^2_Z \cos 2\beta e_f \sin\theta_w{}^2. \tag{3.54}$$

$T_{3f}$ is the weak isospin and $e_f$ is the charge of the fermion $f$. Just as with the chargino case the slepton and squark mass eigenstates diagonalize the above mass matrices [37]. The sneutrino mass eigenstates are $\tilde{\nu}_k$ with $k = 1, 2, 3$, corresponding to $\tilde{\nu}_e$, $\tilde{\nu}_\mu$ and $\tilde{\nu}_\tau$. Separate partners of each fermion chirality state are required [3], so we have two mass eigenstates for each generation of charged slepton, up-type and down-type squark. These eigenstates are $\tilde{e}_k$, $\tilde{u}_k$ and $\tilde{d}_k$ with $k = 1, ..., 6$.

The sfermion mass eigenstates are linked to the left-right eigenstates $\tilde{f}_L$ and $\tilde{f}_R$ by [37]

$$\tilde{f}_{La} = \sum_{k=1}^{6} \tilde{f}_k \mathbf{\Gamma}^{*ka}_{FL}, \tag{3.55}$$

$$\tilde{f}_{Ra} = \sum_{k=1}^{6} \tilde{f}_k \mathbf{\Gamma}^{*ka}_{FR}, \tag{3.56}$$

where $F = U, D, E, \nu$. $\mathbf{\Gamma}^{*ka}_{UL,R}$ and $\mathbf{\Gamma}^{*ka}_{DL,R}$ are $6 \times 3$ squark mixing matrices, $\mathbf{\Gamma}^{*ka}_{EL,R}$ is the $6 \times 3$ charged slepton mixing matrix, and $\mathbf{\Gamma}^{*ka}_{\nu L}$ is the $3 \times 3$ sneutrino mixing matrix.

Simplification of the mass matrices can occur if we assume the absence of flavour changing neutral currents (FCNCs), which is strongly supported by experimental evidence [14], [59]. In models without FCNCs the matrices $\mathbf{A}_U$, $\mathbf{A}_D$, $\mathbf{A}_E$, $\mathbf{M}_Q$, $\mathbf{M}_U$, $\mathbf{M}_D$, $\mathbf{M}_E$, and $\mathbf{M}_L$, become diagonal, and the sfermion mass matrices can be diagonalized analytically [37].

### 3.3.4 The MSSM-25 Parameterisation

Throughout the preceding sections we have introduced a great many free parameters. In order to make a search of the MSSM parameter space feasible we must apply informed assumptions to reduce the number of free parameters to a more manageable number. This simplification can be performed either by setting certain parameters to zero or by making two or more parameters equal to each other. There are many different ways of simplifying the 105-dimensional MSSM parameter space to obtain a reduced parameter space of arbitrary size. Here we describe the method used in this research to reduce 105 parameters down to 25: the MSSM-25 parameter space.

The gaugino and Higgs sectors remain unchanged, giving six parameters:

$$M_1, M_2, M_3 \qquad \text{and} \qquad \mu, \tan\beta, m_A. \tag{3.57}$$

The sfermion mass parameter matrices are simplified by assuming the absence of FCNCs which forces all non-diagonal entries to be zero. Each mass parameter matrix now only has three free parameters, and so the sfermion sector now has a total of 15 parameters. They are denoted:

$$\mathbf{m}^2_{\tilde{Q}} = \begin{pmatrix} m^2_{\tilde{Q}_1} & 0 & 0 \\ 0 & m^2_{\tilde{Q}_2} & 0 \\ 0 & 0 & m^2_{\tilde{Q}_3} \end{pmatrix} \qquad \text{Left-type Squarks} \tag{3.58}$$

$$\mathbf{m}^2_{\tilde{\bar{u}}} = \begin{pmatrix} m^2_{\tilde{\bar{u}}_1} & 0 & 0 \\ 0 & m^2_{\tilde{\bar{u}}_2} & 0 \\ 0 & 0 & m^2_{\tilde{\bar{u}}_3} \end{pmatrix} \qquad \text{Right-type Sup Squarks} \tag{3.59}$$

$$\mathbf{m}^2_{\tilde{\bar{d}}} = \begin{pmatrix} m^2_{\tilde{\bar{d}}_1} & 0 & 0 \\ 0 & m^2_{\tilde{\bar{d}}_2} & 0 \\ 0 & 0 & m^2_{\tilde{\bar{d}}_3} \end{pmatrix} \qquad \text{Right-type Sdown Squarks} \tag{3.60}$$

$$\mathbf{m}^2_{\tilde{L}} = \begin{pmatrix} m^2_{\tilde{L}_1} & 0 & 0 \\ 0 & m^2_{\tilde{L}_2} & 0 \\ 0 & 0 & m^2_{\tilde{L}_3} \end{pmatrix} \qquad \text{Left-type Sleptons} \tag{3.61}$$

$$\mathbf{m}^2_{\tilde{\bar{e}}} = \begin{pmatrix} m^2_{\tilde{\bar{e}}_1} & 0 & 0 \\ 0 & m^2_{\tilde{\bar{e}}_2} & 0 \\ 0 & 0 & m^2_{\tilde{\bar{e}}_3} \end{pmatrix} \qquad \text{Right-type Selectrons} \tag{3.62}$$

For the triple scalar couplings $\mathbf{a}_\mathrm{u}$, $\mathbf{a}_\mathrm{d}$, and $\mathbf{a}_\mathrm{e}$ we again apply the prohibition on FCNCs to eliminate the off diagonal entries. We also restrict the matrices to be Hermitian (and so the diagonal elements to be real) so as to eliminate any CP-violating phases [15]. We also make the assumption that the triple scalar couplings are proportional to the Yukawa matrices $\mathbf{y}_\mathrm{u}$, $\mathbf{y}_\mathrm{d}$, and $\mathbf{y}_\mathrm{e}$. We can set the first and second entries of $\mathbf{a}_\mathrm{u}$ and $\mathbf{a}_\mathrm{d}$ to zero as the corresponding Yukawa couplings are negligibly small, but we retain one parameter for the first and second entries of $\mathbf{a}_\mathrm{e}$ as it is relevant to the calculation of the anomalous magnetic moment of the muon [2]. We

finally arrive at the following triple scalar coupling matrices:

$$\mathbf{a}_{\mathrm{u}} = \begin{pmatrix} 0 & 0 & 0 \\ 0 & 0 & 0 \\ 0 & 0 & a_{\mathrm{u}3} Y_{u33} \end{pmatrix} \tag{3.63}$$

$$\mathbf{a}_{\mathrm{d}} = \begin{pmatrix} 0 & 0 & 0 \\ 0 & 0 & 0 \\ 0 & 0 & a_{\mathrm{d}3} Y_{d33} \end{pmatrix} \tag{3.64}$$

$$\mathbf{a}_{\mathrm{e}} = \begin{pmatrix} a_{\mathrm{e}1} Y_{e11} & 0 & 0 \\ 0 & a_{\mathrm{e}1} Y_{e22} & 0 \\ 0 & 0 & A_{\mathrm{e}3} Y_{e33} \end{pmatrix} \tag{3.65}$$

Thus we have 25 parameters; three each from gaugino and Higgs sectors, 15 from the sfermion sector, and four from the trilinear scalar couplings. This is the parameter space we will be scanning across using the methods soon to be described in Chapter 6.

### 3.3.5 Alternative Parameterisations

Just as we were able to simplify the 105 parameters of the MSSM down to 25 we can make alternative reductions to other numbers of parameters. We shall outline one such example, the MSSM-7 parameterisation, as we will later be comparing results derived from it against those from our MSSM-25 parameter scans.

As the name suggests the MSSM-7 has seven free parameters. The Higgs sector remains unchanged from the full MSSM and the MSSM-25, giving us three parameters, $\mu$, $\tan\beta$ and $m_A$. The three free gaugino sector parameters in the MSSM-25, $M_1$, $M_2$, and $M_3$, are reduced to one, $M_2$, with the values of $M_1$ and $M_3$ defined by functions of $M_2$ derived from renormalization group evolution:

$$M_1 = \frac{5}{3} \tan^2 \theta_W(m_Z) M_2 \tag{3.66}$$

$$M_3 = \frac{\sin^2 \theta_W(m_Z)}{\alpha_{\mathrm{em}}(m_Z)} \alpha_3(m_Z) M_2 \tag{3.67}$$

where $\theta_W(m_Z)$, $\alpha_{\mathrm{em}}(m_Z)$ and $\alpha_3(m_Z)$ are the weak mixing angle, the electromagnetic coupling constant and the strong coupling constant respectively, all of which are running constants and taken at the $m_Z$ ($Z^0$ boson mass) scale.

The slepton matrices are greatly simplified. As with the MSSM-25 the off diagonal elements are set to zero, but additionally, the diagonal elements of all five matrices are set equal to a common parameter. The 15 parameters of the MSSM-25 are thus reduced to one.

In the triple scalar couplings sector $\mathbf{a}_{\mathrm{u}}$ and $\mathbf{a}_{\mathrm{d}}$ are the same as those in MSSM-25, but all elements of the $\mathbf{a}_{\mathrm{e}}$ matrix are set to zero. This sector thus gives two parameters.

Hence this reduction has three parameters from the Higgs sector, one each from the gaugino and slepton sectors and two from the triple scalar couplings, yielding a total of seven parameters.

## 3.4 Supersymmetric Dark Matter

### 3.4.1 $R$-parity

There are additional terms that could have been included in the MSSM superpotential (Equation 3.22) [3]:

$$W_{\Delta L=1} = \lambda_e^{ijk} L_i \cdot L_j \bar{e}_k + \lambda_e^{ijk} L_i \cdot Q_j \bar{d}_k + \mu_L^i L_i \cdot H_{\mathrm{u}} \tag{3.68}$$

$$W_{\Delta B=1} = \lambda_B^{ijk} \bar{u}_i \bar{d}_j \bar{d}_k \tag{3.69}$$

The superfields $L_i$ carry a lepton number of $L = 1$, $\bar{e}$ has $L = -1$, and the rest have no lepton number, so the terms of Equation 3.68 violate lepton number conservation by one unit. The superfields $Q_i$ have a baryon number of $B = 1/3$ and $\bar{u}$ and $\bar{d}$ carry $B = -1/3$, meaning the couplings in Equation 3.69 violate baryon number conservation by one unit. If the couplings $\lambda_L$ and $\lambda_B$ were present in our model protons would decay into lepton-meson pairs, a process that has not been observed in nature. One option would be to impose baryon and lepton number conservation as a fundamental principle and thus rule out Equations 3.68 and 3.69. However it is known that both are violated by non-perturbative electroweak effect which while negligible at low energies could be important at higher energies [3]. So we require a symmetry that is capable of supressing the interactions of 3.68 and 3.69 while still allowing potential lepton and baryon number violation at high energies [3].

The solution is $R$-parity, defined as

$$R = (-1)^{3B+L+2s} \tag{3.70}$$

where $s$ is the spin of the particle. Demanding multiplicative conservation of $R$-parity for all interactions gives the desired effect of prohibiting the terms in Equations 3.68 and 3.69. If we take any vertex and impose conservation of angular momentum then the sum of the spins is always integer valued. Thus for any such vertex $(-)^{2s}$ is always equal to $+1$. Then from inspection of the couplings in Equations 3.68 and 3.69 it is clear they do not conserve $R$-parity and are thus forbidden [3].

Another feature of $R$-parity is that all particles have $R$-parity of $+1$ while sparticles have $R$-parity of -1. This means that the lightest supersymmetric particle (LSP) is stable; it has $R$-parity of -1, and could only decay into lighter, SM particles, all of which have $R-$parity of $+1$, violating $R$-parity conservation. Depending on the choice of parameters the LSP can be any of the sparticles described above, but if it happens to be electrically neutral and uncoloured then it is a natural candidate for WIMP dark matter.

Out of the sparticles described above there are two possibilities for electrically neutral and uncoloured LSPs: neutralinos and sneutrinos. The sneutrino relic density has been shown to pass through the cosmologically interesting range of $0.1 \lesssim \Omega_{\tilde{\nu}} h^2 \lesssim 1.0$ for a mass range of 550 GeV $\lesssim m_{\tilde{\nu}} \lesssim$ 2300 GeV, but this range is ruled out by limits placed on the sneutrino scattering cross section by direct detection experiments [27]. Thus the lightest neutralino is the most promising LSP candidate for WIMP dark matter, and it is this particle we focus our attention on.

One final facet of neutralinos is that they are Majorana particles, which means that they are their own anti-particle [47]. Thus two neutralino LSPs can annihilate with each other and produce SM particles. This does not violate $R$-parity as two sparticles have a combined $R$-parity of $(-1) \times (-1) = 1$, the same as two particles. This self annihilation will become crucial in subsequent chapters.

### 3.4.2 The Neutralino Relic Density

Assuming the scenario of supersymmetry and $R$-parity conservation outlined above, the neutralino WIMPs put forward as a dark matter candidate are relics from the Big Bang and the time immediately after. They were produced at a time when the universe was much denser than it is today, and the baryonic particles were colliding with energy sufficient to create supersymmetric particles. However as the universe expanded and cooled the production of sparticles ceased - the neutralinos we have now are the same ones that existed billions of years ago. As stated in Subsection 2.1.2 results from the WMAP satellite show the cold dark matter relic density to be $\Omega_{\rm DM}h^2 = 0.1120 \pm 0.0056$. This is the figure we aim to obtain with our SUSY dark matter models when we explore the MSSM-25 parameter space, as described in Chapter 6.

Here we describe the process for calculating the relic density for a given supersymmetric model. We first look at a basic scenario that only has annihilations amongst a population of the lightest neutralinos, and then we outline the improvements necessary to include co-annihilations between a set of sparticles with masses close to that of the lightest neutralino. This section draws heavily from Chapter 7 of [11].

In very early, radiation dominated, universe supersymmetric WIMPs were produced by the high energy collisions between particles of the hot, thermal plasma. WIMPs would also annihilate with each other to produce standard model particles. When temperatures were much higher than the WIMP mass, e.g. $T \gg m_\chi$, then the rate of production and annihilation were in equilibrium, with a common rate of

$$\Gamma_{\rm ann} = \langle \sigma_{\rm ann} v \rangle \, n_{\rm eq} \tag{3.71}$$

where $\sigma_{\rm ann}$ is the WIMP annihilation cross section, $v$ is the relative velocity of the two annihilating WIMPs, $n_{\rm eq}$ is the equilibrium number density of the WIMPs, and the angled brackets denote an average over the WIMP thermal distribution.

The temperature of the plasma dropped as the universe expanded, and eventually dropped below the WIMP mass. The production and annihilation reaction rates remained in equilibrium but the number of WIMPs produced decreased by the Boltzmann factor $e^{-m_\chi/T}$ as the only particles with sufficient kinetic energy to create WIMP pairs were in the tail of the Boltzmann distribution. The expansion of the universe also reduced the particle number density $n$ and thus also the production and annihilation rates.

WIMP production finally ceased when the production and annihilation rate $\Gamma_{\rm ann}$ dropped below the expansion rate of the universe. This point in time is known as *freeze out*. Since this time the total number of WIMPs has remained approximately constant and the number density has decreased as the universe has expanded.

Calculation of the relic density begins with the rate equation for the WIMP number density $n$ and the entropy conservation law:

$$\frac{dn}{dt} = -3Hn - \langle \sigma_{\rm ann} v \rangle \left( n^2 - n_{\rm eq}^2 \right) \tag{3.72}$$

$$\frac{ds}{dt} = -3Hs, \tag{3.73}$$

where $t$ is time, $H$ is the Hubble parameter, and $s$ is the entropy density. The first term on the right of Equation 3.72 describes changes in number density due to the expansion of the universe,

while the second term covers changes from production and annihilation of WIMPs.

We then combine Equations 3.72 and 3.73 and change variables to give

$$\frac{dY}{dx} = \frac{1}{3H}\frac{ds}{dx}\left\langle \sigma_{\text{ann}} v \right\rangle \left(Y^2 - Y_{\text{eq}}^2\right) \tag{3.74}$$

where

$$Y = \frac{n}{s}, \qquad\qquad x = \frac{m}{T}, \tag{3.75}$$

$m$ is the LSP WIMP mass and $T$ is the photon temperature.

From the Friedman equation we can describe the Hubble parameter in terms of the mass-energy density $\rho$ as

$$H^2 = \frac{8\pi}{3M_{\text{P}}^2}\rho \tag{3.76}$$

where $M_{\text{P}} = 1.22 \times 10^{19} GeV$ is the Planck mass. Energy density $\rho$ and entropy density $s$ are given as functions of the photon temperature:

$$\rho = \frac{\pi^2}{30} g_{\text{eff}}(T) T^4 \tag{3.77}$$

$$s = \frac{2\pi^2}{45} h_{\text{eff}}(T) T^3 \tag{3.78}$$

where $g_{\text{eff}}$ and $h_{\text{eff}}$ are effective degrees of freedom for the energy and entropy densities respectively, calculations of which can be found in [44].

By defining the degrees of freedom parameter $\sqrt{g_*}$ as

$$\sqrt{g_*} = \frac{h_{\text{eff}}}{\sqrt{g_{\text{eff}}}}\left(1 + \frac{T}{3h_{\text{eff}}}\frac{dh_{\text{eff}}}{dT}\right) \tag{3.79}$$

we can rewrite Equation 3.74 as

$$\frac{dY}{dx} = -\sqrt{\frac{\pi M_{\text{P}}^2}{45}}\frac{\sqrt{g_*}m}{x^2}\left\langle \sigma_{\text{ann}} v \right\rangle \left(Y^2 - Y_{\text{eq}}^2\right). \tag{3.80}$$

This equation can then be solved numerically to find $Y$ at the present time, denoted $Y_0$. As an initial condition we take $Y = Y_{\text{eq}}$ at $x \simeq 1$, e.g. at $m \simeq T$, the point at which WIMP production begins to decrease exponentially. From $Y_0$ we compute the LSP WIMP relic density as

$$\Omega_\chi h^2 = \frac{m_\chi s_0 Y_0 h^2}{\rho_c^0} = 2.755 \times 10^8 Y_0 m_\chi \text{GeV}^{-1} \tag{3.81}$$

where $\rho_c^0$ and $s_0$ are the critical density and entropy density at the present time respectively.

For a more accurate calculation of the relic density we must include the effects of co-annihilations on the WIMP population. Co-annihilations take place when there are one or more sparticles with masses close to that of the LSP [11]. They open up a range of new channels that can deplete

the neutralino population. For instance, coannihilation between neutralinos and charginos could produce the following reactions:

$$\tilde{\chi}_1^0\ \tilde{\chi}_2^0\ \rightarrow\ W^+\ W^- \qquad \text{and} \qquad \tilde{\chi}_1^0\ e^-\ \rightarrow\ \tilde{\chi}_2^-\ \nu_e \tag{3.82}$$

The left hand reaction has a neutralino LSP coannihilating with a slightly heavier neutralino to produce SM particles. This type of reaction is important as it provides significant additional channels for the depletion of the neutralino population.

In the right-hand reaction a neutralino LSP converts to a heavier chargino through a scattering off a particle in the thermal plasma. The energy barrier that normally impedes these types of conversions is overcome if the temperature is high enough to supply the requisite extra energy, e.g. if the mass difference $\Delta m \sim$ temperature $T$. The heavier sparticle can then undergo several types of interaction: decay back down to the LSP state, which will leave the neutralino LSP density unchanged; coannihilate with a neutralino LSP to produce SM particles, which, considering it took a neutralino LSP to create the heavier sparticle in the first place ultimately leaves the particle/sparticle ledger unchanged; or it could potentially find another heavy sparticle to coannihilate to SM particles with, which would produce a change in the neutralino density.

Thus including co-annihilations opens up new channels for the annihilation and production of LSPs and so alters the annihilation and production cross section used in our calculations. This means we must replace the simple $\sigma_{\text{ann}}$ with a significantly more complicated formula that takes into account all possible co-annihilation channels. A full description can be found in Chapter 23 of [37].

# Chapter 4

# Dark Matter Detection

There are two broad methods for detecting dark matter, direct and indirect. Direct detection methods aim to observe the interaction of a dark matter particle within the detector itself, while indirect methods endeavour to infer the presence of dark matter through any secondary particles it produces. The latter category includes dark matter detection with IceCube and so is discussed first and in greater depth, but later in this chapter direct detection methods are also covered.

## 4.1 Indirect Detection of Neutralino Dark Matter

### 4.1.1 Accumulation and Annihilation of Neutralinos in the Sun

#### WIMP Capture Rate

As astrophysical bodies such as the sun and the earth orbit the galaxy they move through the dark matter halo. If the dark matter halo consists of WIMPs then weak interactions can occur between the body's constituent nuclei and the WIMP. If the WIMP loses sufficient energy during such a scattering it can drop below the escape velocity of the body at the point of interaction and become gravitationally trapped. Once inside the body it can undergo further weak scatterings and lose yet more energy, dropping down into successively lower orbits after each scattering. In this way astrophysical bodies can accumulate a population of WIMPs within them.

The capture rate $C(t)$ is calculated under the assumption that the halo is infinitely far away from the body, or in other words, the initial velocity of a halo particle is unaffected by the gravitational field of the body. We now derive a formula for the capture rate based on [71] and the earlier work of [39]. The time dependent capture rate is

$$C(t) = 4\pi \int_0^{R_\star} r^2 \int_0^\infty \frac{f(u)}{u} w \Omega_v^-(w) \mathrm{d}u \mathrm{d}r \tag{4.1}$$

where $R_\star$ is the radius of the body, $r$ is the radius of a given point from the centre of the body, $u$ is the velocity of the WIMP before it is affected by the body's gravitational field and $f(u)$ is the WIMP velocity distribution in the halo. At a given point of radius $r$ the escape velocity is $v = v(r,t)$, and by the time an incoming WIMP reaches this point its velocity will be $w = w(u,r,t) = \sqrt{u^2 + v^2}$. $\Omega_v^-(w)$ is the rate at which WIMPs with velocity $w$ scatter to velocities less than the escape velocity $v$ and thus become trapped.

Several elements of Equation 4.1 are deserving of closer inspection. First, we look at the velocity distribution of WIMPs in the halo, $f(u)$. We make the assumption that the WIMP velocities in the halo have an isothermal distribution with a dispersion of $\bar{v}$. In the rest frame of the halo

the velocity distribution of WIMPs is

$$f_0(u) = \frac{4}{\sqrt{\pi}} \left(\frac{3}{2}\right)^{3/2} \frac{\rho_\chi}{m_\chi} \frac{u^2}{\bar{v}^3} \exp\left(-\frac{3u^2}{2\bar{v}^2}\right), \tag{4.2}$$

where $\rho_\chi$ is the WIMP density. Switching to the frame of an astrophysical body such as a star or a planet moving through the halo with velocity $v_\star$ the distribution becomes

$$f_\star(u) = f_0(u) \exp\left(-\frac{3v_\star^2}{2\bar{v}^2}\right) \frac{\sinh\left(\frac{3uv_\star}{\bar{v}^2}\right)}{\frac{3uv_\star}{\bar{v}^2}}. \tag{4.3}$$

We now turn our attention to $\Omega_v^-(w)$, the rate at which WIMPs scatter from velocity $w$ to below the escape velocity $v$. For a WIMP with mass $m_\chi$ and velocity $w$ colliding with a nucleus with zero initial velocity and mass $m_{\rm nuc}$ simple kinematics tells us that WIMPs final velocity $w'$ will be

$$w' = \frac{m_\chi - m_{\rm nuc}}{m_\chi + m_{\rm nuc}} w \tag{4.4}$$

The assumption of a fully elastic collision gives us an upper limit on the fraction of energy lost by the neutralino:

$$\frac{\Delta E}{E} = \frac{1/2\, m_\chi w^2 - 1/2\, m_\chi w'^2}{1/2\, m_\chi w^2} \tag{4.5}$$

$$= \frac{1/2\, m_\chi w^2 - 1/2\, m_\chi \left(\frac{m_\chi - m_{\rm nuc}}{m_\chi + m_{\rm nuc}}\right)^2 w^2}{1/2\, m_\chi w^2} \tag{4.6}$$

$$= \frac{4 m_\chi m_{\rm nuc}}{(m_\chi + m_{\rm nuc})^2} \tag{4.7}$$

We make the change of variables

$$\mu \equiv \frac{m_\chi}{m_{\rm nuc}} \qquad \text{and} \qquad \mu_\pm \equiv \frac{\mu \pm 1}{2} \tag{4.8}$$

and rewrite the fractional energy loss limits as

$$0 \leq \frac{\Delta E}{E} \leq \frac{\mu}{\mu_+^2}. \tag{4.9}$$

The requirement that a WIMP must lose enough energy during the scattering for its final velocity $w'$ to be below the local escape velocity, e.g. $w' \leq v$, gives us a lower limit on the fractional energy loss:

$$\frac{\Delta E}{E} = \frac{1/2\, m_\chi w^2 - 1/2\, m_\chi w'^2}{1/2\, m_\chi w^2} \tag{4.10}$$

$$\therefore \frac{\Delta E}{E} \geq \frac{w^2 - v^2}{w^2} \tag{4.11}$$

$$\geq \frac{u^2}{w^2} \tag{4.12}$$

The fractional energy loss of the WIMP is thus

$$\frac{u^2}{w^2} \leq \frac{\Delta E}{E} \leq \frac{\mu}{\mu_+^2} \tag{4.13}$$

From this we can derive a limit on $u$, the velocity of the WIMP before it was affected by the body's gravitational field:

$$\frac{u^2}{w^2} \leq \frac{\mu}{\mu_+^2}, \tag{4.14}$$

which upon rearrangement gives

$$u^2 \leq \frac{\mu v^2}{\mu_-^2}. \tag{4.15}$$

We can now give an expression for $\Omega_v^-(w)$:

$$\Omega_v^-(w) = \sum_i \Omega_{v,i}^-(w) \tag{4.16}$$

$$= \sum_i w\sigma_i n_i(r,t)\frac{\mu_i}{\mu_{+,i}^2}\theta\left(\frac{\mu_i v^2}{\mu_{-,i}^2} - u^2\right)\int_{\Delta_-}^{\Delta_+} |F_i(\Delta)|^2 \mathrm{d}\Delta \tag{4.17}$$

where $i$ is the $i^{\text{th}}$ nuclear species and $n_i(r,t)$ is its local number density in the body. $\theta$ is the Heaviside step function embodying the limit in Equation 4.15. For clarity the fractional energy loss and its limits from Equation 4.13 have been denoted as

$$\Delta_- = \frac{u^2}{w^2} \qquad \leq \qquad \Delta = \frac{\Delta E}{E} \qquad \leq \qquad \Delta_+ = \frac{\mu_i}{\mu_{+,i}^2}. \tag{4.18}$$

$F_i(\Delta)$ is the nuclear form factor for the $i^{\text{th}}$ nuclear species.

$\sigma_i$ is the total cross section for scattering between a WIMP and a nucleus of species $i$. The fundamental interactions that gives rise to $\sigma_i$ are neutralino-quark and neutralino-gluon, the strengths of which are determined by the parameters of the particular supersymmetric model. To build up to a neutralino-nuclei cross section we add layers describing the quark and gluon distribution within the nucleons and the nucleon distribution within the nucleus. In practice there are only two significant interactions to consider, spin-dependent and spin-independent [47]. We can approximate $\sigma_i$ for a nuclei of species $i$, atomic number $A_i$ and spin $J_i$ as

$$\sigma_i = \beta^2\left[\sigma_{\text{SI}}A_i^2 + \sigma_{\text{SD}}\frac{4(J_i+1)}{3J_i}\left|\langle S_{\text{p},i}\rangle + \langle S_{\text{n},i}\rangle\right|^2\right] \tag{4.19}$$

where $\sigma_{\text{SD}}$ and $\sigma_{\text{SD}}$ are the hydrogen-normalised spin-independent and spin-dependent nuclear scattering cross sections respectively, $\langle S_{\text{p},i}\rangle$ and $\langle S_{\text{n},i}\rangle$ are the expectation values of the spin of the nuclei's proton and neutron systems respectively, and

$$\beta = \frac{m_{\text{nuc}}(m_\chi + m_{\text{p}})}{m_{\text{p}}(m_\chi + m_{\text{nuc}})}. \tag{4.20}$$

where $m_{\text{p}}$ is the mass of the proton.

The spin-dependent portion of $\sigma_i$ on the other hand is increased by larger nuclear spins due to the $J_i$, $\langle S_{\text{p},i}\rangle$, and $\langle S_{\text{n},i}\rangle$ terms. The determination of nuclear spin is dependent on the internal structure of the nuclei and is not proportional to atomic number. Within nuclei in the ground state many nucleons are aligned into spin-singlet pairings, i.e. pairs where one nucleon is spin $+1/2$ and the other is $-1/2$. The contribution of these nuclei pairs to the overall spin of the

nuclei is zero. Thus the total spin of a nuclei is generally determined by the presence of unpaired nuclei. Nuclei with even $A_i$ will usually have zero total spin and so zero spin-dependent WIMP interactions, while nuclei with odd $A_i$ will have half integer total spins and thus undergo spin-dependent interactions with WIMPs [31].

The spin-independent portion of the cross section $\sigma_i$ is increased by larger nucleon masses due to the $A_i^2$ term. For heavy nuclei this enhancement can be large; for example xenon has $A_{\mathrm{Xe}}^2 \approx 16,900$, depending on the isotope. This fact has important consequences on direct detection experiments and will thus be discussed further in Section 4.2. So as we move from lighter to heavier nuclei the contribution of the spin-independent interaction to the total cross section will grow, while the spin-dependent contribution will fluctuate based on the exact composition of the nuclei.

The rate of capture is thus dependent on the mass, motion and composition of the body, the mass and distribution of the WIMPs, and the interaction cross section between the WIMP and the nuclei that make up the body.

### WIMP Annihilation Rate

As mentioned in Subsection 3.4.1 neutralinos are Majorana particles and thus undergo self-annihilation. Just as we have a formula for the capture rate of WIMPs in astrophysical bodies we also have a one to describe the annihilation rate. For a given point in the body the local annihilation rate per unit volume is [71]

$$a(r,t) = \frac{1}{2}\langle \sigma_{\mathrm{a}} v \rangle_0 n_\chi(r,t)^2 \tag{4.21}$$

where $\langle \sigma_{\mathrm{a}} v \rangle_0$ is the non-relativistic limit of the velocity-averaged annihilation cross section, and $n_\chi(r,t)$ is the local WIMP density. To find the total annihilation rate $A(t)$ we integrate over the total volume of the body, assumed to be a sphere of radius $R_\star$:

$$A(t) = 4\pi \int_0^{R_\star} r^2 a(r,t) \mathrm{d}r \tag{4.22}$$

We can combine the capture and annihilation rates into a differential equation describing the total population of WIMPs in an astrophysical body $N(t)$:

$$\frac{\mathrm{d}N(t)}{\mathrm{d}t} = C(t) - 2A(t) \tag{4.23}$$

Solving this equation is complicated by the fact that the annihilation rate is dependent on the local density of WIMPs which is in turn dependent on the total WIMP population $N(t)$. We numerically solve Equation 4.23 for the annihilation rate at the current time by iterating over the time $t$ [71].

### Annihilation products

Assuming that the neutralino WIMP is the lightest supersymmetric particle, as it must be to be a viable dark matter candidate, then the products of its self-annihilation will be SM particles such as quarks, charged leptons, gauge and Higgs bosons. The type of annihilation products will depend on the neutralino mass, its composition in terms of gauge-eigenstates, and other MSSM parameters such as coupling strengths. As we take the thermal average annihilation cross

section in the zero velocity limit there is no direct neutralino to neutrino annihilation channel available [47]. Most of the annihilation products will be immediately absorbed within the sun's core, but some will decay into neutrinos which can escape [47]. It is these neutrinos that we hope to detect with the IceCube Neutrino Observatory.

The neutralino self-annihilation almost always results in a two-body final state, meaning the annihilation products will each have energies equal to the neutralino mass. These products then undergo two- or three-body decay, and so any neutrinos produced will have a wide distribution of energies, with typically energies being approximately $1/3$ to $1/2$ of the neutralino mass [47]. There are a wide range of decay products which can be organized according to the neutrino spectrum they produce. The limiting cases are generally taken to be $b\bar{b}$, which gives a soft neutrino spectrum, and $W^+W^-$, which gives a very hard neutrino spectrum [1]. For neutralino masses below 80GeV $\tau\bar{\tau}$ performs the role of a hard spectrum limiting case [25].

Distinguishing the neutrinos produced by solar neutralino annihilations from those produced by other means is done using energy and direction measurements. The position of the sun can be used to select suitable neutrino events and reduce background signals [1]. Typical masses for neutralino WIMPs range from 10 GeV to several TeV, and so the neutrinos derived from these particles will produce a signal distinct from the MeV range solar neutrinos produced by the sun's fusion reactions [47]. The IceCube Neutrino Observatory, which we will now describe, has a low energy threshold of approximately 10 GeV, above the range of solar neutrino energies.

### 4.1.2 The IceCube Neutrino Observatory

The interaction cross section of neutrinos is very small, making them very hard to detect. The recently completed IceCube Neutrino Observatory consists of a cubic kilometer of extremely transparent natural ice deep below the South Pole. When a neutrino interacts with a nucleus in the ice via the charged weak boson $W^{\pm}$ (charged-current interaction) a charged lepton is produced with the same flavour as the incident neutrino. This charged lepton receives between 50% and 80% of the neutrino's energy, with the remainder being transferred to the target nucleus which then fragments to form a hadronic shower. If the neutrino instead interacts via the neutral weak boson $Z^0$ (neutral-current interaction) then the target nucleus receives a fraction of the neutrino's energy and only a hadronic shower is produced. Depending on their energy the charged lepton and any charged particles in the hadronic shower may be traveling faster than the local speed of light in ice and if so will produce Cherenkov radiation. Through observation of this Cherenkov radiation we can determine the energy of the neutrino and reconstruct its path. Muons produced by charged current interactions are of particular interest because their mean free paths can be up to 10km for the most energetic neutrinos. Thus we can detect neutrinos that interact outside the volume of instrumented ice that makes up IceCube, and so the effective volume for muon neutrinos exceeds $1\text{km}^3$ [41].

The Cherenkov radiation is detected by Detector Optical Modules (DOMs), 5160 of which are imbedded deep in the ice. At the heart of each DOM is a photomultiplier tube (PMT) which transforms the Cherenkov radiation into electrical signals via the photoelectric effect. These signals are digitized and time-stamped by electronics within the DOM then sent to the central counting house on the surface. The PMT and its associated electronics are sealed within a borosilicate glass pressure vessel [41]. Included in the DOM are a series of LEDs that can be 'flashed' as a means of calibrating IceCube.

The DOMs are arranged along strings which are lowered down vertical wells melted down into

the ice using a hot water drill. The main array consists of 80 such strings, each with 60 DOMs attached, arranged in a triangular pattern, with a horizontal spacing of 125m [77]. The DOMs on these strings are attached every 17m along a kilometer of cable, and when embedded in the ice extend from 1450m to 2450m below the surface. In addition to these strings there are six more placed in the centre of the main array with a horizontal separation of only 72m. Again these strings have 60 DOMs but their vertical distribution is different; 50 DOMs are arranged with 7m spacing between 2107m and 2450m below the surface, and the remaining ten are arranged with 10m spacing between 1750m and 1860m below the surface. These six strings plus the seven main array strings around them constitute the DeepCore array, which will be discussed further.

The purpose of DeepCore is to increase sensitivity to low energy neutrinos, particularly those produced by dark matter annihilations [83]. The main array is capable of detecting muon neutrinos down to an energy of about 100 GeV, the exact minimum energy being analysis dependent [41]. However the DeepCore array can bring this threshold down an order of magnitude to below 10 GeV [83]. The outer strings of the main array and the 60 DOMs located further up the six DeepCore strings will act as a veto against the background of down going atmospheric muons [83].

The performance of IceCube is characterized by the effective area $A(E_\nu, \theta)$, a function of the incident neutrino energy $E_\nu$ and zenith angle $\theta$. Effective area is determined through simulations, and is on the order of $1\text{km}^2$ [41].

Cosmic ray interactions within the atmosphere create air showers of downward going muons and muon neutrinos. These are detected by IceCube and form a background for observations of neutrinos from solar neutralino annihilations. This background is minimised by taking data during the austral winter, when the sun is below the horizon, and then only selecting events with upward going reconstructed paths [1].

### 4.1.3 Other Indirect Detection Methods

Indirect detection of dark matter with IceCube as described above relies on searching for the neutrinos produced by neutralino annihilations in the Sun. However indirect detection methods can utilise other messenger particles besides neutrinos and look for these messenger particles in places other than the sun.

There are several examples of alternative regions in which to look for the products of neutralino annihilations. Annihilations will occur within the dark matter halo of our own galaxy and can potentially be detected through the $\gamma$-rays they emit [75]. The dark matter halos of dwarf galaxies could also produce gamma ray signals, though our ability to detect them is uncertain [55; 64]. These $\gamma$-ray signals could be detected by the Large Area Telescope (LAT) aboard the Fermi Gamma-ray Space Telescope [6].

## 4.2 Direct Detection of Neutralino Dark Matter

If the dark matter halo around the Milky Way does indeed consist of neutralino WIMPs then there is a constant flux of them flowing through the earth as we orbit around the galaxy. The aim of direct detection experiments is to observe the recoil of nuclei in a detector material when struck by neutralinos from this flux [47]. This nuclear recoil can be observed in three different ways. The energy from the recoiling nucleus can cause the atom to ionize and eject detectable electrons. This same energy can also cause electrons to jump up a higher energy level. When

this excited electron decays back down to a lower energy level it will emit a photon which can be detected. This process is known as scintillation. Finally, if the target nucleus is embedded in a crystal the nuclear recoil can produce phonon excitations, which can be measured through minute changes in temperature [69].

The neutralino-nucleus cross sections are very small, with current limits from direct detection experiments showing them to be less than $\sim 10^{-38}$ cm$^2$ or $\sim 10^{-44}$ cm$^2$ for spin-dependent [29] and spin-independent [5] interactions respectively. Hence direct detection experiments must be very sensitive. Understanding and eliminating the effects of background signals is very important. Background for direct detection comes from cosmic rays and the gammas and muons they induce, and also radioactive isotopes within the equipment and immediate surrounds of the experiments. To reduce the background from cosmic rays the detectors are placed deep underground and sophisticated shielding is installed. Special attention is paid to the materials used in the construction of the experimental apparatus to reduce contamination by radioisotopes. The motion of the earth around the sun can also be used to distinguish signal from background. If we assume the sun has a reasonably constant velocity relative to the dark matter halo as it orbits the centre of the galaxy, there will be a yearly modulation of the earth's velocity relative to the halo as we orbit the sun. For half of our orbit we will be moving in the same direction as then sun relative to the halo, and for the other half we will be moving in the opposite direction. Thus there should be a yearly modulation in the flux of neutralinos through the earth and through our detectors, and so also a yearly modulation in the detection rate [47].

### 4.2.1 XENON100 Direct Detection Experiment

The XENON100 experiment is a scintillation detector installed underground at the Laboratori Nazionali del Gran Sasso laboratory near Rome, Italy [5]. It consists of 161 kg of ultrapure liquid xenon (LXe) separated into a 99 kg veto volume surrounding an optically separated 62 kg target volume. Following a WIMP nucleon scatter XENON100 can detect not only the prompt scintillation light produced (known as S1 signal) but also the ionization electrons - as these electrons pass through the gaseous xenon at the top of the detector they will excite atoms and so produced further scintillation light. Detection of both forms of scintillation light is done with PMTs [5].

As described above in Subsection 4.1.1 the atomic mass of xenon gives an enhancement of $A^2_{\mathrm{Xe}} \approx 16,900$ to the spin-independent WIMP interaction, giving the XENON100 experiment good sensitivity to this interaction. Based on 100.9 days worth of data taken between 13 January and 8 June 2010 limits have been placed on the spin independent elastic WIMP-nucleon cross section as a function of WIMP mass [5]. In Chapter 7 these limits are utilized in the analysis of our MSSM-25 parameter space scans and simulations.

### 4.2.2 ZEPLIN-III Direct Detection Experiment

The ZEPLIN-III experiment is located 1100m below the surface at the Boulby Underground Laboratory in the United Kingdom [52]. It has a similar setup to the XENON-100 experiment, using a 12 kg LXe target with a layer of gaseous xenon above and recording S1 and S2 scintillation signals. Their first science run lasted from 27 February to 20 May 2008 and from this data the ZEPLIN-III collaboration derived limits for spin-dependent WIMP-nucleon cross sections [52]. Two different limits were calculated based on two nuclear spin distributions that each used different nucleon-nucleon potentials, designated Bonn-A and Bonn-CD. The Bonn-A limit is utilised in our analyses found in Chapter 7.

### 4.2.3 SIMPLE Direct Detections Experiment

The SIMPLE (Superheated Instrument for Massive ParticLe Experiments) detector, located at the Laboratoire Souterrain á Bas-Bruit (LSBB, Low Noise Underground Laboratory) in southern France, takes a different approach to direct detection. It consists of 15 Superheated Droplet Detectors (SDDs) that contain a gel matrix throughout which droplets of superheated liquid chlorofluorocarbon $C_2ClF_5$ are homogeneously distributed [29]. Deposition of energy by a WIMP scattering can cause the superheated liquid droplets to transition to a gaseous phase and form bubbles. The nucleation of these bubbles is accompanied by an acoustic shock wave which is detected by a piezoelectric transducer placed at the top of the SDD [35].

One advantage of this approach is the ability to tune the energy sensitivity to reduce background. By adjusting the thermodynamic properties of the superheated liquid it is possible to set a required energy deposition threshold for bubble nucleation and so make the detector effectively insensitive to many background sources. The SDDs of the SIMPLE experiment are built using this principle and are thus insensitive to electrons, $\gamma$-rays and cosmic muons [29]. Also the use of a chlorofluorocarbon liquid is advantageous due to the increased sensitivity to WIMP-proton spin-dependent interactions of fluorine-19 [29], the stable isotope of fluorine that makes up 100% of fluorine on earth [60].

Limits from this experiment on the spin-dependent WIMP-proton scattering cross section are used as part of our analyses in Chapter 7.

# Chapter 5

# Statistical Framework and the Calculation of Exclusion Confidence Levels

In this chapter we describe the statistics used in this research, starting with basic concepts then moving on to the calculations specific to our analyses and simulations.

## 5.1 The Frequentist and Bayesian Formulations of Statistics

### 5.1.1 The Poisson Distribution

The Poisson distribution models the number of rare but unlimited events occurring in a given time frame [32]. For example the number of deaths from bizarre gardening accidents would be described by a Poisson distribution - they are rare events but there is the potential for a limitless number of them to occur.

Consider observing a process that emits particles for a set length of time $T$. Let the average number of particle 'hits' we see in our detector caused by this process be $\theta$, and occurrence of each hit be independent. Suppose we then divide up the time interval $T$ into $N$ subintervals, each of length $t = \frac{T}{N}$, with $N$ large enough to ensure that the probability of two hits occurring in the same interval is negligible. The probability that a hit occurs in one of these subintervals is now $p = \frac{\theta}{N}$. As the occurrence of each hit is independent, then the probability of a subinterval containing a hit is independent of the other subintervals. Thus we can model the probability of observing a certain number of hits $n$ in the entire interval $T$ using the binomial distribution [57]:

$$P(n) = \binom{N}{n} p^n \left(1-p\right)^{N-n} \tag{5.1}$$

where $\binom{N}{n}$ is the binomial coefficient

$$\binom{N}{n} = \frac{N!}{n!(N-n)!}. \tag{5.2}$$

Substituting for the probability $p = \frac{\theta}{N}$ we get

$$P(n) = \binom{N}{n} \left(\frac{\theta}{N}\right)^n \left(1-\frac{\theta}{N}\right)^{N-n}. \tag{5.3}$$

Now we take $N$ and let it tend towards infinity, which gives us the following limits:

$$\lim_{N\to\infty} \binom{N}{n} \left(\frac{1}{N}\right)^n = \frac{1}{n!} \tag{5.4}$$

$$\lim_{N\to\infty} \left(1 - \frac{\theta}{N}\right)^{-n} = 1 \tag{5.5}$$

$$\lim_{N\to\infty} \left(1 - \frac{\theta}{N}\right)^{N} = e^{-\theta} \tag{5.6}$$

Applying these limits to Equation 5.3 yields the formula for the Poisson Distribution, the probability, for a given time frame, of $n$ events occurring when the average number of events is $\theta$:

$$P(n) = \frac{\theta^n e^{-\theta}}{n!}. \tag{5.7}$$

We can recast Equation 5.7 as a *likelihood*:

$$\mathcal{L}(n|\theta) = \frac{\theta^n e^{-\theta}}{n!}. \tag{5.8}$$

This is the probability of observing $n$ hits given an average number $\theta$ hits. This conditionality was assumed in the derivation of Equation 5.7; now it is explicit.

### 5.1.2 Frequentist and Bayesian Viewpoints

There are several different ways to interpret what probability is. The frequentist school of thought holds that there exists a true, objective probability which will give predictions as to the outcome of future experiements. It is based on relative frequencies; the probability is the number of times an event occurs in a test series divided by the total number of trials in the series [20]. In the context of the particle counting example used to motivate the derivation of the Poisson distribution then there is a true value of $\theta$ and the probability distribution tells us how many times we will see a certain particle count $n$ in a given time frame.

The Bayesian view point is that probability is a description of our degree of belief. The likelihood of Equation 5.8 is used to measure how certain we are that $\theta$ is indeed the correct average number of hits. Bayesians see probability as a subjective quantity as opposed to the objective quantities they regard frequentist probabilities to be. Bruno de Finetti states that "Probability... if regarded as something endowed with some kind of objective existence is... an illusory attempt to exteriorize or materialize our true probabilistic beliefs" [21].

This interpretation of probability as quantifying our degree of belief in a certain model is embodied by Bayes's Theorem. In its most general form Bayes's Theorem links conditional probabilities. Given an outcome $y$, such as the number of hits recorded by a detector, and a set of parameters $\boldsymbol{\theta} = (\theta_1, ..., \theta_d)$, we can construct the conditional probabilities $P(y|\boldsymbol{\theta})$, the probability that outcome $y$ will occur given a specific set of parameters $\boldsymbol{\theta}$, and $P(\boldsymbol{\theta}|y)$, the probability that the set of parameters $\boldsymbol{\theta}$ is correct given that outcome $y$ has been observed. These are linked by Bayes's Theorem:

$$P(\boldsymbol{\theta}|y) = \frac{P(y|\boldsymbol{\theta})P(\boldsymbol{\theta})}{P(y)}. \tag{5.9}$$

$P(\boldsymbol{\theta})$ is the *prior probability*, and summarises all the previous beliefs and knowledge one has regarding the parameters $\boldsymbol{\theta}$. $P(y|\boldsymbol{\theta})$ is the *likelihood*, and just as above, it is the probability of observing outcome $y$ assuming the model described by parameters $\boldsymbol{\theta}$ is correct. $P(y)$ can be regarded as a normalization constant and is calculated using the integral [18]

$$P(y) = \int P(y|\boldsymbol{\theta})P(\boldsymbol{\theta})\mathrm{d}\boldsymbol{\theta}. \tag{5.10}$$

This is the total probability of observing outcome $y$ assuming the parameter space spanned by $\theta$ is a description of the correct model.

$P(\boldsymbol{\theta}|y)$ is, in the context of Bayes's theorem, called the *posterior probability*, and embodies our updated knowledge following the observation of $y$ [18].

Consider the posterior probability $P(\boldsymbol{\theta}|y)$, where, as before, $\boldsymbol{\theta} = (\theta_1, ..., \theta_d)$ is a set of $d$ parameters. Under some circumstances only a subset of $\boldsymbol{\theta}$ will of interest to us. The remaining parameters that do not interest us are called *nuisance parameters*. To focus the posterior probability in on the parameters of interest and remove the effects of the nuisance parameters we can perform a process known as Bayesian marginalisation. Denoting the interesting parameters $\boldsymbol{\psi}$ and the nuisance parameters $\boldsymbol{\lambda}$ (e.g. $\boldsymbol{\theta} = (\boldsymbol{\psi}, \boldsymbol{\lambda})$), the posterior probability as it stands is $P(\boldsymbol{\theta}|y) = P(\boldsymbol{\psi}, \boldsymbol{\lambda}|y)$. The marginalisation is performed by integrating over the nuisance parameter like so [10]:

$$P(\boldsymbol{\psi}|y) = \int P(\boldsymbol{\psi}, \boldsymbol{\lambda}|y)\mathrm{d}\boldsymbol{\lambda} \tag{5.11}$$

## 5.2 Application to Dark Matter Searches

We now apply the statistical ideas and machinery described above to the focus of this thesis, supersymmetric dark matter searches.

### 5.2.1 Construction of the Likelihood Function

Our likelihood is based on the Poissonian distribution. If, in a given span of time, the total predicted number of events is $\theta_{tot}$, then the likelihood of $n_{tot}$ events occurring is

$$\mathcal{L}\left(n_{tot}|\theta_{tot}\right) = \frac{\theta_{tot}^{n_{tot}} e^{-\theta_{tot}}}{n!}. \tag{5.12}$$

Both signal and background contribute to the total number of predicted events $\theta_{tot}$ and the number of events $n_{tot}$. Hence we split $\theta_{tot}$ up as $\theta_{tot} = \theta_{sig} + \theta_{BG}$. We can link $\theta_{sig}$ to the differential neutrino flux $\frac{\mathrm{d}\Phi(E)}{\mathrm{d}E}$ by

$$\theta_{sig} = \int_0^\infty A(E)\frac{\mathrm{d}\Phi(E)}{\mathrm{d}E}\mathrm{d}E, \tag{5.13}$$

where $A(E)$ is the effective area of the detector at a given energy $E$.

We then introduce an error into the signal rate $\theta_{sig}$:

$$\theta_{sig} \to \varepsilon\theta_{sig} \tag{5.14}$$

to account for systematic observational errors stemming from sources such as estimates of the effective area, event reconstructions, ice properties etc. We model this error $\varepsilon$ as a Gaussian distribution centred around 1 with a variance of $\sigma_\varepsilon^2$. So our likelihood $\mathcal{L}$ is now

$$\mathcal{L}\left(n_{tot}|\theta_{BG},\theta_{sig},\varepsilon\right)=\frac{\left(\theta_{BG}+\varepsilon\theta_{sig}\right)^{n_{tot}}e^{-(\theta_{BG}+\varepsilon\theta_{sig})}}{n_{tot}!}. \tag{5.15}$$

With an assumed Gaussian distribution for $\varepsilon$ we can removed it from the likelihood function by performing a semi-Bayesian marginalization over it [70]. The method is considered semi-Bayesian because we are applying Bayesian marginalization not to a posterior probability as we did in Equation 5.11, but directly to a likelihood, which is a frequentist quantity. The marginalisation gives us

$$\mathcal{L}\left(n_{tot}|\theta_{BG},\theta_{sig}\right)=\frac{1}{\sqrt{2\pi}\sigma_\varepsilon}\int_0^\infty\frac{\left(\theta_{BG}+\varepsilon\theta_{sig}\right)^{n_{tot}}e^{-(\theta_{BG}+\varepsilon\theta_{sig})}}{n_{tot}!}e^{-\frac{1}{2}\left(\frac{1-\varepsilon}{\sigma_\varepsilon}\right)^2}\mathrm{d}\varepsilon. \tag{5.16}$$

### 5.2.2 The p-value

Using the likelihood function constructed above we can create a new quantity: the *p-value*. In general the p-value is the probability of obtaining a predicted or hypothesized result at least as extreme as the observed result, assuming the null hypothesis is true [12]. To apply this general definition to our situation we must define what me mean by three key terms: *null hypothesis*, *predicted result*, and *observed result*.

The *null hypothesis* is the hypothesis which we want to reject [81]. This is paired with the alternative hypothesis which we aim to support by showing that the null hypothesis is false. As we are working towards model rejection we take the null hypothesis to be the case where we have events originating from background and solar neutralino annihilation as described by a particular MSSM-25 parameter point.

The *results* are what we measure, which in this context are the number of events in IceCube. The predicted result is the number of events we should see in IceCube from background ($\theta_{BG}$) and solar neutralino annihilations ($\theta_{sig}$) as predicted by a specific set MSSM-25 parameters. For all p-value calculations $\theta_{BG}$ is equal to 1478.6702 events, a figure generated from simulations performed by Matthias Danninger (Stockholm University) of background signal within a 20° cone around the sun. These simulations take into account the detection sensitivities of IceCube by way effective area.

The observed result, $n_{tot}$, is the number of events actually observed in the experiment during a given period, and the absence of real data from IceCube we use simulations. Given that we do not know if SUSY is valid and if it is, what IceCube signal it would generate, the only real option for creating a simulated data set is to assume that we get no signal from solar neutralino annihilation and base any conclusions on this assumption. To generate such a signal a Poissonion model was constructed with the expected value $\theta$ set to $\theta_{BG}$= 1478.6702. This gives a probability distribution for obtaining $n$ events from background described by Equation 5.7. A value for $n_tot$ was then extracted from this model. For this research the particular value extracted is $n_{tot}$=1452 events. This simulated value of $n_{tot}$ was generated by Matthias Danninger (Stockholm University).

So in our specific case the p-value $p\left(n_{tot}|\theta_{BG},\theta_{sig}\right)$ is the probability of observing $n_{tot}$ events assuming a neutrino flux from both background ($\theta_{BG}$) and solar neutralino annihilation ($\theta_{sig}$).

The formula for the p-value is [12]

$$p\left(n_{tot}|\theta_{BG},\theta_{sig}\right)=\sum_{n\leq n_{tot}}\mathcal{L}\left(n|\theta_{BG},\theta_{sig}\right). \tag{5.17}$$

We can also calculate the p-value of the background alone by setting $\theta_{sig}=0$.

$$p\left(n_{tot}|\theta_{BG}\right)=\sum_{n\leq n_{tot}}\mathcal{L}\left(n|\theta_{BG}\right)=\sum_{n\leq n_{tot}}\frac{\left(\theta_{BG}\right)^{n}e^{-(\theta_{BG})}}{n!}. \tag{5.18}$$

Using this p-value we can exclude models with confidence levels of $(1-p\left(n_{tot}|\theta_{BG},\theta_{sig}\right))$ [48]. However this confidence level is susceptible to statistical fluctuations in the background rate; if the number of observed events is too low to account for the estimated background then there is the potential to exclude the signal and perhaps even the background at a high confidence interval [48]. To solve this problem we normalise the signal and background p-vale $p\left(n_{tot}|\theta_{BG},\theta_{sig}\right)$ by the background only p-value $p\left(n_{tot}|\theta_{BG}\right)$ to create the *modified p-value*:

$$p_{mod}\left(n_{tot}\right)=\frac{p\left(n_{tot}|\theta_{BG},\theta_{sig}\right)}{p\left(n_{tot}|\theta_{BG}\right)}. \tag{5.19}$$

This modified p-value is then used to calculate exclusion confidence levels:

$$\left(1-p_{mod}(n_{tot})\right)=\left(1-\frac{p\left(n_{tot}|\theta_{BG},\theta_{sig}\right)}{p\left(n_{tot}|\theta_{BG}\right)}\right). \tag{5.20}$$

The utility of the modified p-value becomes clear if we consider a situation where we wish to keep the confidence level derived from the modified p-value constant; perhaps we are selecting points excluded with a certain confidence level. If statistical fluctuations cause the background to have a low p-value (and so excluding the background with a high confidence level) then to maintain the $p_{mod}$ derived confidence level the signal and background p-value $p\left(n_{tot}|\theta_{BG},\theta_{sig}\right)$ must be correspondingly reduced, increasing the necessary exclusion confidence level for the signal and background hypothesis.

The modified p-value is what is calculated by the `DarkSUSY` IceCube likelihood routines. Taking this p-value we can state that, given a set of observational data with $n_{tot}$ events, a MSSM-25 model described by a point in the 25-dimensional parameter space is excluded at a confidence level of $(1-p_{mod}(n_{tot}))$. Given that for this analysis we are using simulated data with background events only, any exclusion limits we calculate apply only to the case where IceCube observes no signal from solar neutralino annihilations.

# Chapter 6

# Searches and Simulations of the MSSM-25 Parameter Space

We have now described the tools necessary to take a point in the MSSM-25 parameter space, derive the particle mass spectrum, their couplings, the neutralino capture and annihilation rate in the sun, the flux of neutrinos through IceCube and the confidence level with which we can rule out the point assuming we see no signal in IceCube. We now look at how these tools are applied to the exploration of the MSSM-25 parameter space. Firstly we look at the `DarkSUSY` software package which automates the calculation of the observables for a given point. Then we describe the VEGAS algorithm, which decides which points in the parameter space to test. We then look at the higher level programme control and sorting used for this research, followed by the specific details of the exploration.

## 6.1 The `DarkSUSY` Software Package

The pathways between the specific parameter values and the observables we calculate are complex and intertwined. To allow the investigation of many points in a short time the necessary calculations are implemented as computer software. The package we use for this research is `DarkSUSY` [38]. It was first publicly released in 2000 and is written in `FORTRAN77`.

The current public release takes a set of given parameters and then calculates the mass spectrum, the coupling constants, the neutralino relic density, the solar capture and annihilation rate and the flux of neutrinos though the earth. Higgs masses and their vertices are calculated using the `FeynHiggs` package [33; 22; 42; 43]. A more advanced version of this software, named `iclike`, was used for this research, but has yet to be publicly released. (This version was released after submission of this thesis as `DarkSUSY 5.0.6` [72].) It has the additional capability of calculating the predicted signal and background in IceCube and calculating p-values for each point as described in Subsection 5.2.2.

### 6.1.1 MSSM-25 modifications to `DarkSUSY`

One of the first tasks of this project was to modify `iclike` to accept 25 parameter models. Previously it had only been capable of working with seven, 13, or 15 parameter models. The 25 parameters as described by Subsection 3.3.4 were denoted as:

$$M_1 = \texttt{m1}, \qquad M_2 = \texttt{m2}, \qquad M_3 = \texttt{m3} \tag{6.1}$$

$$\mu = \texttt{mu} \qquad \tan\beta = \texttt{tanbe} \qquad m_A = \texttt{ma} \tag{6.2}$$

$$\mathbf{m}^2_{\tilde{Q}} = \begin{pmatrix} m^2_{\tilde{Q}_1} & 0 & 0 \\ 0 & m^2_{\tilde{Q}_2} & 0 \\ 0 & 0 & m^2_{\tilde{Q}_3} \end{pmatrix} = \begin{pmatrix} \texttt{msqL1}^2 & 0 & 0 \\ 0 & \texttt{msqL2}^2 & 0 \\ 0 & 0 & \texttt{msqL3}^2 \end{pmatrix} \tag{6.3}$$

$$\mathbf{m}^2_{\tilde{\bar{u}}} = \begin{pmatrix} m^2_{\tilde{\bar{u}}_1} & 0 & 0 \\ 0 & m^2_{\tilde{\bar{u}}_2} & 0 \\ 0 & 0 & m^2_{\tilde{\bar{u}}_3} \end{pmatrix} = \begin{pmatrix} \texttt{msqRu}^2 & 0 & 0 \\ 0 & \texttt{msqRc}^2 & 0 \\ 0 & 0 & \texttt{msqRt}^2 \end{pmatrix} \tag{6.4}$$

$$\mathbf{m}^2_{\tilde{\bar{d}}} = \begin{pmatrix} m^2_{\tilde{\bar{d}}_1} & 0 & 0 \\ 0 & m^2_{\tilde{\bar{d}}_2} & 0 \\ 0 & 0 & m^2_{\tilde{\bar{d}}_3} \end{pmatrix} = \begin{pmatrix} \texttt{msqRd}^2 & 0 & 0 \\ 0 & \texttt{msqRs}^2 & 0 \\ 0 & 0 & \texttt{msqRb}^2 \end{pmatrix} \tag{6.5}$$

$$\mathbf{m}^2_{\tilde{L}} = \begin{pmatrix} m^2_{\tilde{L}_1} & 0 & 0 \\ 0 & m^2_{\tilde{L}_2} & 0 \\ 0 & 0 & m^2_{\tilde{L}_3} \end{pmatrix} = \begin{pmatrix} \texttt{mslL1}^2 & 0 & 0 \\ 0 & \texttt{mslL2}^2 & 0 \\ 0 & 0 & \texttt{mslL3}^2 \end{pmatrix} \tag{6.6}$$

$$\mathbf{m}^2_{\tilde{\bar{e}}} = \begin{pmatrix} m^2_{\tilde{\bar{e}}_1} & 0 & 0 \\ 0 & m^2_{\tilde{\bar{e}}_2} & 0 \\ 0 & 0 & m^2_{\tilde{\bar{e}}_3} \end{pmatrix} = \begin{pmatrix} \texttt{mslRe}^2 & 0 & 0 \\ 0 & \texttt{mslRmu}^2 & 0 \\ 0 & 0 & \texttt{mslRtau}^2 \end{pmatrix} \tag{6.7}$$

$$\mathbf{a}_{\mathrm{u}} = \begin{pmatrix} 0 & 0 & 0 \\ 0 & 0 & 0 \\ 0 & 0 & a_{\mathrm{u}3} Y_{u33} \end{pmatrix} = \begin{pmatrix} 0 & 0 & 0 \\ 0 & 0 & 0 \\ 0 & 0 & \texttt{atm} Y_{u33} \end{pmatrix} \tag{6.8}$$

$$\mathbf{a}_{\mathrm{d}} = \begin{pmatrix} 0 & 0 & 0 \\ 0 & 0 & 0 \\ 0 & 0 & a_{\mathrm{d}3} Y_{d33} \end{pmatrix} = \begin{pmatrix} 0 & 0 & 0 \\ 0 & 0 & 0 \\ 0 & 0 & \texttt{abm} Y_{d33} \end{pmatrix} \tag{6.9}$$

$$\mathbf{a}_{\mathrm{e}} = \begin{pmatrix} a_{\mathrm{e}1} Y_{e11} & 0 & 0 \\ 0 & a_{\mathrm{e}1} Y_{e22} & 0 \\ 0 & 0 & A_{\mathrm{e}3} Y_{e33} \end{pmatrix} = \begin{pmatrix} \texttt{aemum} Y_{e11} & 0 & 0 \\ 0 & \texttt{aemum} Y_{e22} & 0 \\ 0 & 0 & \texttt{ataum} Y_{e33} \end{pmatrix} \tag{6.10}$$

$$\tag{6.11}$$

The primary changes were implemented in the file `dsgive_model25.f`. For each parameterisation there is a corresponding `dsgive_model` file, which takes the given set of input parameters and translates them into the 105 internal MSSM parameter. For example `dsgive_model25.f` sets the internal parameters $M_1$, $M_2$, and $M_3$ equal to the input parameters `m1`, `m2`, and `m3` respectively. In contrast `dsgive_model.f`, which corresponds to the MSSM-7 parameterisation, takes the input parameter `m2` and sets the internal parameter $M_2$ equal to it, then sets $M_1$ and $M_3$ using Equations 3.66 and 3.67.

Further changes throughout the `DarkSUSY` code were necessary to implement support for 25-

dimensional models, primarily related to internal parameter sets. A bug fix in FeynHiggs was also performed; we suspect that its cause is related to the increased number of parameters creating new parameter combinations that in turn drive downstream variables to previously untested areas.

## 6.2 The VEGAS Algorithm and adscan_mssm25

With the tools to analyse a given point now described we look at the method by which points are selected. The most basic option would be a simple grid scan: thinking of the parameter space as a 25-dimensional hyperspace, pick $N$ equidistant points along each parameter coordinate and thus build up a grid of $N^{25}$ points, which are then analysed one by one. However the computational cost of such a scan would be cosmological in scale; if we took $N = 10$ and took the generous assumption of testing one model every clock cycle on a 2.5GHz machine the processing time would be on the order of the age of the universe. Thus we must turn to more advanced techniques based on random sampling, collectively known as Monte-Carlo methods. For this research we use the VEGAS algorithm, described below, implemented in the adscan_mssm25 programme.

The VEGAS algorithm is a Monte Carlo method for computing multidimensional integrals based on importance sampling [65]. Monte Carlo integration techniques calculate the integral of a function based on the value of the function at a number of random points in its input parameter space. Basic methods will select points using a uniform probability density $\rho$, but greater efficiency can be gained by weighting $\rho$ and focusing the selection of points into certain regions. For a given function $f$ integrated over a volume $V$ the probability density suggested by importance sampling is [65]

$$\rho = \frac{|f|}{\int |f| dV}. \tag{6.12}$$

So the probability density $\rho$ is proportional to the function $f$, known as the importance function. However on the face of it there is an internal inconsistency: we are calculating $\rho$ in order to more accurately determine the integral of $f$, but the formula for $\rho$ already involves the integral of $f$. We solve this by iterating the formula. Starting with a uniform probability density, we calculate an initial approximation of the integral and then feed it into Equation 6.12. Using the freshly calculated probability distribution we calculate a better approximation of the integral and insert it back into Equation 6.12 to get an even better distribution $\rho$. Continued iteration of this process will generate successively better approximations of the integral. The benefit of an extra iteration eventually drops off, with more than 10 iterations rarely being useful [65].

In exploring the MSSM-25 parameter space we hijack the VEGAS algorithm. Instead of using a distribution of points to find the integral of a function we set a function and use the algorithm to focus in on 'good' points. We choose our metric of what points are good to be the proximity of that point's neutralino relic density to the value derived from WMAP measurements (see Subsection 2.1.2). To this end the importance function we insert into the VEGAS algorithm is

$$f(\Omega_\chi h^2) = \exp\left[-\frac{1}{2}\left(\frac{\Omega_\chi h^2 - \Omega_{\text{WMAP-7}} h^2}{\sigma_{\Omega h^2}}\right)^2\right] \tag{6.13}$$

where $\Omega_{\text{WMAP-7}} h^2 = 0.1120$, the cold dark matter relic density derived from 7-year WMAP measurements [51]. The denominator $\sigma_{\Omega h^2} = 0.01$ is the error, and is set to this value to allow for both theoretical and experimental error. A point with neutralino relic density $\Omega_\chi h^2$ close to the WMAP measurement will have a larger $f$ value and so larger $\rho$ value also. Thus on the

next iteration the algorithm will focus its point selection on areas around this successful point.

A `FORTRAN77` implementation of the VEGAS algorithm has been built into a larger programme called `adscan_mssm7`, a `DarkSUSY` version of the `adscan` programme written by Oliver Brein [13]. Its name is short for *adaptive scan*, as it adapts its probability density function during the course of calculation run. As part of this research `adscan_mssm7` was modified to search the MSSM-25 parameter space, giving rise to `adscan_mssm25`. This programme starts by reading in simulation parameters from two files:

- `ds25scanTagsOutputRandom.txt` contains a six character scantag used to keep track of points, the names the call the output files, and a random integer to seed the initial uniform pseudo-random selection of points; and
- `ds25scanVegasMSSMParams.txt` contains the parameters for the VEGAS algorithm and the limits on the 25 model parameters.

The VEGAS algorithm parameters include `ITMX`, the number of times Equation 6.12 is iterated, NCALL, the maximum number of function evaluations per iteration, and `ext_ifunc`, which specifies the exact version of the importance function $f$ [65].

Each point selected VEGAS algorithm is first fed into the `dssusy` routine of `DarkSUSY`. This calculates the mass spectrum of the Higgs bosons and sparticles, their mixings, their interaction vertices, and their decay widths. It also identifies which species of sparticle the LSP is. If the particular set of parameters given by the point results in an unphysical system (e.g. a particle with negative mass), or it the neutralino is not the LSP, the point is discarded and VEGAS moves on.

`adscan_mssm25` then calls `dsacbnd`, which checks various observables derived from the model parameters against limits from accelerator experiments. Accelerator limit values are taken from the Particle Data Group's Review of Particle Physics 2002 [40]. The observables checked are the sparticle mass spectrum, the Higgs mass, the invisible $Z^0$ boson decay width, the $b \to s\gamma$ width, the $\rho$ parameter (calculated from the Weinberg weak mixing angle $\theta_W$ and the masses of the $W^{\pm}$ and $Z^0$ bosons), and the anomalous magnetic moment of the muon. If the point produces observables that are ruled out by this experimental evidence, the point is discarded VEGAS, again, moves on.

If it passes all the checks listed above the point is now considered valid and `calc_omega` is called to calculate the relic density. This is fed into the importance function which deems how good the point is and whether or not this region should be focused on during the next iteration. At this point `adscan_mssm25` also outputs the details of this point to several files organized by suffix:

- ____`out`: 25 parameters that define the point,
- ____`spec`: mass spectrum for sparticles and Higgs bosons,
- ____`ac`: MSSM contribution to anomalous magnetic dipole-moment of the muon $(g-2)$ and branching ratios for $\tau \to \mu + \gamma$ and $b \to s + \gamma$,
- ____`omega`: neutralino relic density $\Omega_\chi h^2$ and $x_f = \frac{m_\chi}{T_f}$ where $T_f$ is the freeze out temperature, and
- ____`ddxsec`: spin-independent and spin-dependent neutralino-nucleon cross sections

## 6.3 ds25scancontrol and Higher Level Coordination

The benefit of increasing the number of iterations performed by adscan_mssm25 beyond 10 is low [65]. The more effective way to explore the MSSM-25 parameter space and build up a list of viable points is to run adscan_mssm25 multiple times each with a different random number seed. To implement this a Python controller script, ds25scancontrol, was written. This controller script takes as input a three letter code and the number of adscan_mssm25 runs to perform. The controller writes to the ds25scanTagsOutputRandom.txt file:

- the six character scantag, consisting of the three letter code followed by the number of the adscan_mssm25 run,
- the names of the output files, consisting of the three letter code, the suffixes listed above, and the number of the adscan_mssm25 run, and
- a random integer seed for the initial pseudo-random point selection.

The parameters listed in ds25scanVegasMSSMParams.txt remain constant for each run of adscan_mssm25, and so are changed manually when required. The controller then executes adscan_mssm25, which reads in the parameters listed in the two input files and begins its scan of the parameter space.

One instance of adscan_mssm25 runs on a single core, and so for multiple-core machines the controller will run multiple instances of adscan_mssm25. Once the first adscan_mssm25 process is started, the contoller script waits 20 second to let this process read in the data from the input files. It then generates a new scantag, a new random integer and new file output names, writes them to file, and sets another adscan_mssm25 instance running. Once the desired number of cores are each running one instance of adscan_mssm25, the controller enters a sleep mode. Every three minutes it awakes to poll the processes. If any adscan_mssm25 programmes have completed their scan and the maximum number of runs has not been reached the controller will write a new input file and start another adscan_mssm25 run.

## 6.4 Distillation and Post-Processing

The calculation of signal rates and p-values for IceCube can be computationally intensive and so are only performed on a small subset of the total number of points found. The data from a single run of ds25scancontrol, which is made up from multiple adscan_mssm25 runs, is fed into a Python script called OmegaDistilleryMSSM25. This selects the points with a neutralino relic density within two uncertainties of the 7 year WMAP measurement (Equation 2.4), i.e. in the range $0.1120 - 0.0112 \leq \Omega_\chi h^2 \leq 0.1120 + 0.0112$. The out, spec, ac, omega and ddxsec data for points which satisfy this criterion are output to the distilled files, with names consisting of Distilled, the three character ds25scancontrol code, followed by the corresponding suffix.

The Distilled____Out file is then fed into the Python script ICRatesPostProcessorController. The script parcels the data into a number of blocks equal to the number of cores one has available, and each of these blocks is then fed into a different instance of a FORTRAN programme called ICRatesPostProcessor. This programme runs through the parameters for each point and calculates the IceCube signal, log-likelihood, and p-value, and the neutrino emission rate from the sun and the earth. It also calculates the total annihilation cross section for the neutralino and the branching ratios for various channels. The calculation and output of this data was not included in early versions of adscan_mssm25 and so was instead included in the post processor to

| Parameter | Units | W Set | | V Set | |
|---|---|---|---|---|---|
| m1 | GeV | -4000 | 4000 | -16000 | 16000 |
| m2 | GeV | -4000 | 4000 | -16000 | 16000 |
| m3 | GeV | -4000 | 4000 | -16000 | 16000 |
| mu | GeV | -1000 | 1000 | -4000 | 4000 |
| ma | GeV | -1000 | 1000 | -4000 | 4000 |
| tanbe | | 2 | 65 | 2 | 65 |
| msqL1 | GeV | 100 | 4000 | 100 | 16000 |
| msqL2 | GeV | 100 | 4000 | 100 | 16000 |
| msqL3 | GeV | 100 | 4000 | 100 | 16000 |
| msqRu | GeV | 100 | 4000 | 100 | 16000 |
| msqRc | GeV | 100 | 4000 | 100 | 16000 |
| msqRt | GeV | 100 | 4000 | 100 | 16000 |
| msqRd | GeV | 100 | 4000 | 100 | 16000 |
| msqRd | GeV | 100 | 4000 | 100 | 16000 |
| msqRb | GeV | 100 | 4000 | 100 | 16000 |
| mslL1 | GeV | 100 | 4000 | 100 | 16000 |
| mslL2 | GeV | 100 | 4000 | 100 | 16000 |
| mslL3 | GeV | 100 | 4000 | 100 | 16000 |
| mslRe | GeV | 100 | 4000 | 100 | 16000 |
| mslRmu | GeV | 100 | 4000 | 100 | 16000 |
| mslRtau | GeV | 100 | 4000 | 100 | 16000 |
| atm | GeV | -8000 | 8000 | -32000 | 32000 |
| abm | GeV | -8000 | 8000 | -32000 | 32000 |
| aemum | GeV | -8000 | 8000 | -32000 | 32000 |
| ataum | GeV | -8000 | 8000 | -32000 | 32000 |

Table 6.1: MSSM-25 Simulation Parameter Limits, W and V Sets

keep the `adscan_mssm25` output files consistent. The results from each `ICRatesPostProcessor` instance are then recombined once all processing is complete. The annihilation rates and branching ratios are placed in `Distilled____AchRates` files, and the IceCube and neutrino rates data are placed in `Distilled____NtelicRates` files, with the middle space filled with the particular three-character `ds25scancontrol` code.

Finally the distilled results from each `ds25scancontrol` run are collated together into global distilled files, from which plotting and data analysis are performed.

## 6.5 Specific Simulation Details

### 6.5.1 Parameter Limits

Two different sets of parameter limits were used for the simulations, denoted the W and V sets. The smaller W set was used first followed by the larger V set; backwards letter order is a relic from the earlier use of X and Y for initial runs of development versions of the simulations. The W and V limit sets are listed in Table 6.1.
An upper limit on $\tan\beta$ of 80 was attempted for the V limit set, however a previously unknown internal restriction in DarkSUSY prevented this parameter from moving beyond 65. This limit has been implemented as larger values of $\tan\beta$ cause difficulties with electroweak symmetry

| | W Set | V Set | Total |
|---|---|---|---|
| Raw Points | 4,980,801 | 3,269,477 | 8,250,278 |
| Distilled Points | 927,037 | 1,667,511 | 2,594,548 |
| % with suitable $\Omega_\chi h^2$ | 18.6 | 51.0 | 31.4 |
| | | | |
| `adscan_mssm25` Runs | 106 | 60 | 166 |
| Raw Points per Run | 46,988 | 54,491 | 49,700 |
| Distilled Points per Run | 8,746 | 27,792 | 15,630 |

Table 6.2: Summary of Simulation Data

breaking [4].

### 6.5.2 Run Details

Each of the three letters in the `ds25scancontrol` codes served a function. The first denoted which computer it was run on. The DarkSUSY software was installed on five computers labelled A through E, ranging in power from a four core Intel i7 (eight effective cores due to HyperThreading) to a two-core Intel Core 2 Duo. The second letter denoted which parameter limit set was used for the run, W or V. The third letter ran from A onwards and distinguished subsequent runs of the same data set on the same computer. So for example AwA, AwB and AwC denoted subsequent runs using the W data set on Computer A.

All data files were transferred back to the A computer for distillation and post processing. Information regarding the number of points found for each data set is summarised in Table 6.2. Raw points are those that have only passed the physicality and accelerator bounds tests described in Subsection 6.2 and so were outputted by `adscan_mssm25`. Distilled points are those that have passed the additional test of having suitable relic density values.

Already we can see how much easier it is to find suitable points within the enlarged data set. On each run the V set produced slightly more raw points, but over three times more distilled points. 51.0% of raw V set points turned out to have suitable $\Omega_\chi h^2$ values compared with only 18.6% of W data set points.

### 6.5.3 Random Raw Data Set

A random selection of 250,000 data points was extracted from the raw files and fed into `ICRatesPostProcessorController` . This set is used during analysis to see the areas `adscan_mssm25` explored but did not necessarily find points with suitable relic density. A percentage of these points will have suitable relic density but not all.

### 6.5.4 MSSM-7 Data Set

For comparison purposes a data set based on the MSSM-7 Parameterisation was acquired. This set was produced by Joakim Edsjö, Christopher Savage (Stockholm University) and Pat Scott (McGill University), and consisted of `out`, `spec`, `ac`, `omega` and `ddxsec` files covering 271,765 points across the parameter space. These files were fed into the `OmegaDistilleryMSSM25` programme and yielded 236,910 points within our relic density selection bracket. The distilled

points were then fed into `ICRatesPostProcessorController`, which for this task was running a version of `ICRatesPostProcessor` modified to work with MSSM-7 models.

# Chapter 7

# Results and Analysis

## 7.1 Analytical Methods and Approach

Three key questions will drive our analysis of the data generated by the MSSM-25 parameter space scans described in previous chapters:

1. Are there areas of the MSSM-25 parameter space which can be excluded by results from IceCube, and if so, what are they?

2. What is the advantage of using IceCube for indirect dark matter detection?

3. What is the utility of using the MSSM-25 parameterization instead of smaller parameterizations, such as the MSSM-7?

As stated in Subsection 5.2.2 the experimental signal used in our analysis is replaced with a simulated signal that is consistent with background and contains no signal from simulated solar neutralino annihilations. Thus we must preface any conclusion we make with *assuming a signal consistent with background is detected by IceCube...*

Our primary analytical tool is the modified p-value derived in Chapter 5. We recast this as a confidence exclusion level equal to $(1 - p_{mod})$. Using this tool we can take given set of parameters and specify the confidence level with which we could exclude this point if no signal above background is detected. We define brackets of confidence level using $\sigma$ values. A common colour coding of points is described in Table 7.1 along with the details of the brackets used. The gray background in the plots is composed of the points from the random raw sample described in Subsection 6.5.3. Also given in Table 7.1 is a rough indication of the correlation between the confidence levels and the corresponding IceCube signal and ease of exclusion. A point which predicts a high amount of signal in IceCube would be easy to exclude if no signal is observed. Conversely it would be very difficult to exclude models which predict very little IceCube signal.

| $\sigma$ | Confidence Level | Colour | Predicted IC Signal | Ease of Exclusion |
|---|---|---|---|---|
| $0 \leq \sigma < 1$ | $0 \leq CL < 0.6826895$ | Red | Low | Hard |
| $1 \leq \sigma < 3$ | $0.6826895 \leq CL < 0.9973002$ | Green | Medium | Medium |
| $3 \leq \sigma < 5$ | $0.9973002 \leq CL < 0.9999994$ | Cyan | High | Easy |
| $5 \leq \sigma$ | $0.9999994 \leq CL < 1$ | Blue | Very High | Very Easy |

Table 7.1: Confidence Level Brackets and Colour Coding

An exclusion confidence level of $5\sigma$ is generally thought of as the 'gold standard', while anything below $1\sigma$ is considered not to be excludable at all. Many direct detection experiments publish exclusion limits at 90% confidence levels, so cyan coloured points, which represent $> 99\%$ confidence levels, can be considered very good.

The display of over 2.5 million points is not a straight forward task and so deserves some comment. Each set of points is plotted in its own layer, with successive layers being displayed on top those before it. First the random raw sample points are plotted with large grey dots, followed by the red points as smaller dots. The green and then cyan points are plotted with dots the same size as those used for the red points.Finally the points with exclusion confidence levels above $5\sigma$ are plotted at large navy blue points.

Given these plotting methods one must interpret the plots in a certain way. A large, concentrated region of cyan does not necessarily mean that we can exclude all points with parameter values within that region with confidence level between $3\sigma$ and $5\sigma$. There is the potential for many red points to be hidden underneath the cluster of cyan points. All we can conclude from such a concentration is that there are a great many models with these parameters that can be excluded with confidence level between $3\sigma$ and $5\sigma$.

The search method also dictates how we must view these plots. The VEGAS algorithm focuses the point selection of `adscan_mssm25` in areas which produce points with neutralino relic density close to that measured by the WMAP satellite. As we shall see in Subsection 7.2.4 this can sometimes cause excessive focus around certain parameter values and the neglect of others. Thus an absence of points in an area of a plot does not necessarily mean a true void in the MSSM-25 parameter space.

The first question can be answered by plotting the distribution of each of the 25 parameters and looking for areas with high concentrations of cyan and blue points. This analysis is performed in Section 7.2. The second question will be answered by making comparisons to limits placed on observables by other experiments, particularly direct detection experiments such as those described in Section 4.2. We answer this question in Section 7.3. Answering the third question will require comparison between the observables derived from the MSSM-25 and MSSM-7 parameter sets. These comparisons can be found in Section 7.4.

## 7.2 Parameter Space Exclusion

When we plot parameter value against parameter value we find that very similar structures and forms are repeated amongst the gaugino, squark, slepton and triliple scalar coupling parameter classes. Hence for brevity we display here a representative sample of these plots (Figures 7.2 - 7.9).

Before we analyse the specific structure of each parameter class some general comments can be made regarding features present in all the plots. In Figures 7.1, 7.2, 7.3, 7.4, 7.5, 7.7, 7.8, and 7.9, distinct boundaries can be seen between certain areas of the plots. This is the result of combining data produced by simulations that used two different sets of parameter limits, the W and V limit sets as described in Subsection 6.5.1. For example in Figure 7.2 the limit of the W set can be clearly seen as a line at $M_2 = 4000$ GeV. For squark, slepton and triple scalar coupling classes the V set covers the majority of the plot area and the W set is a small, dense block of points in the lower left-hand corner.

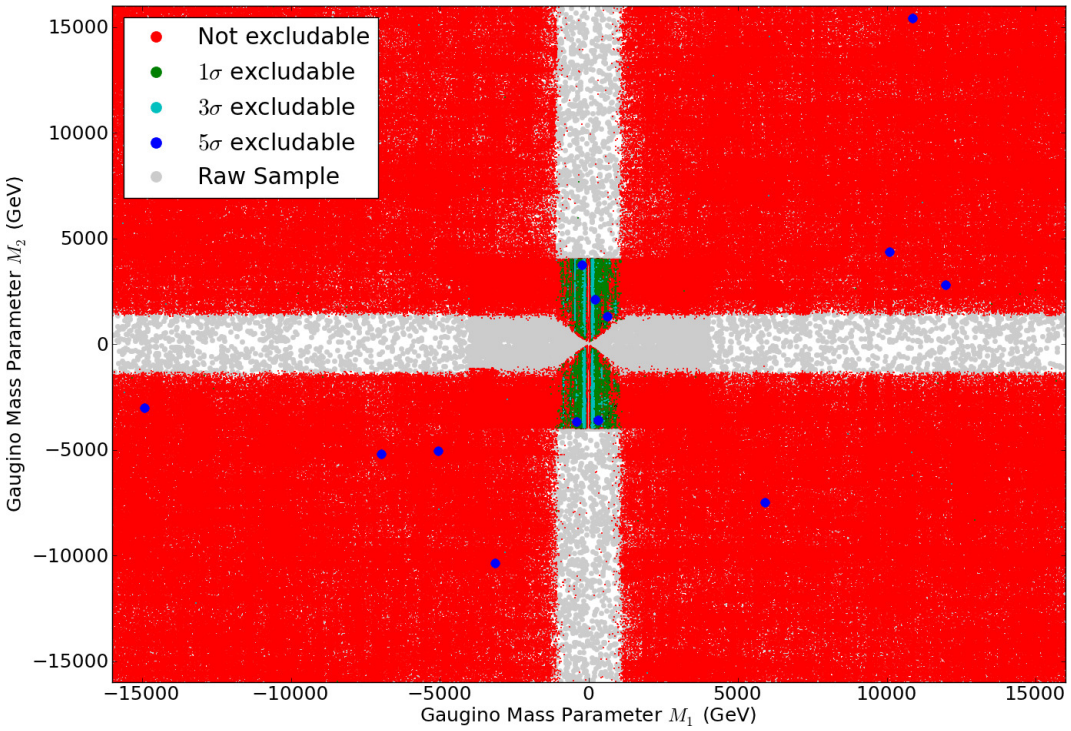


Figure 7.1: Gaugino parameters $M_1$ vs $M_2$.

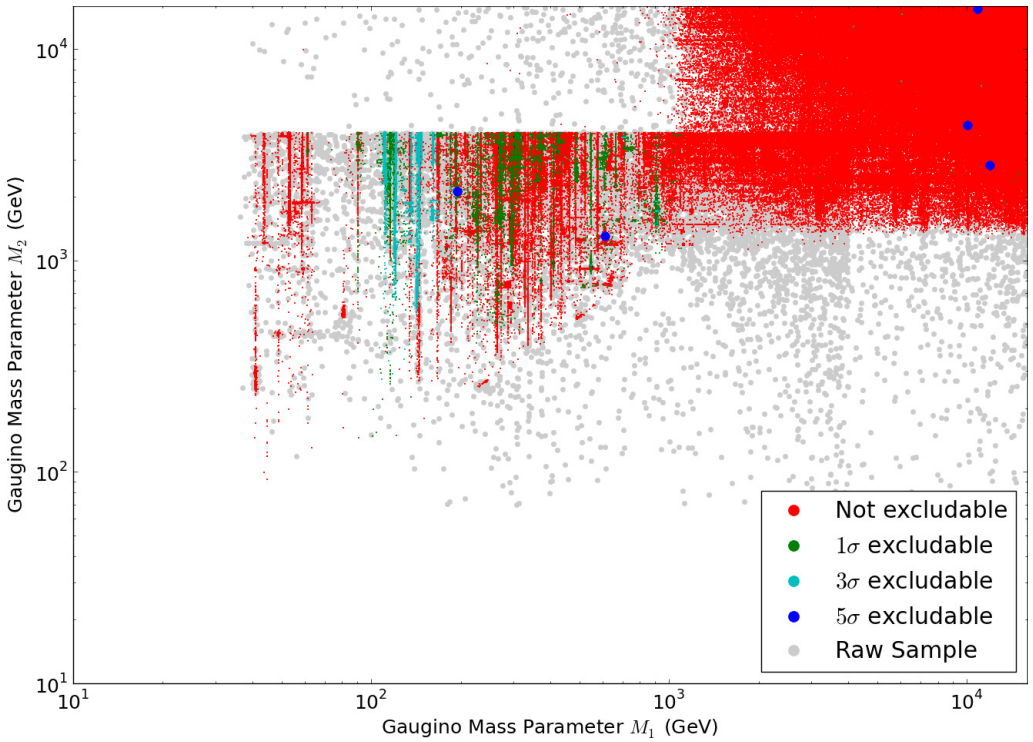


Figure 7.2: Gaugino parameters $M_1$ vs $M_2$, upper right quadrant of Fig. 7.1, with logarithmic axes to enhance view of inner region.

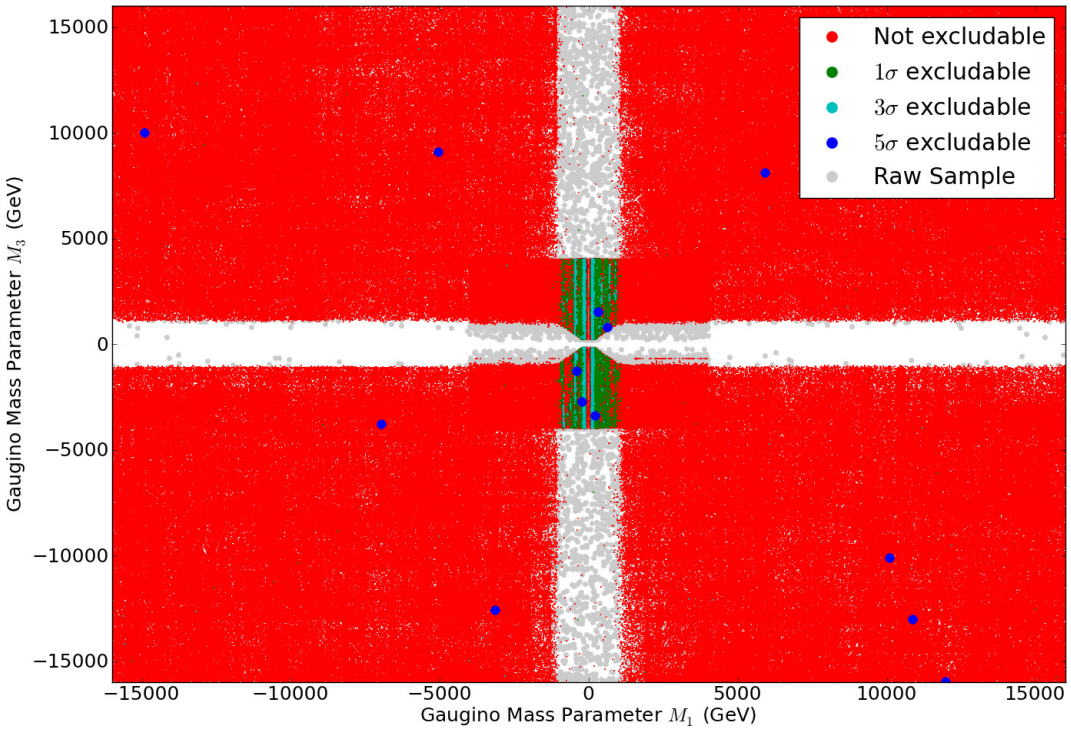


Figure 7.3: Gaugino parameters $M_1$ vs $M_3$.

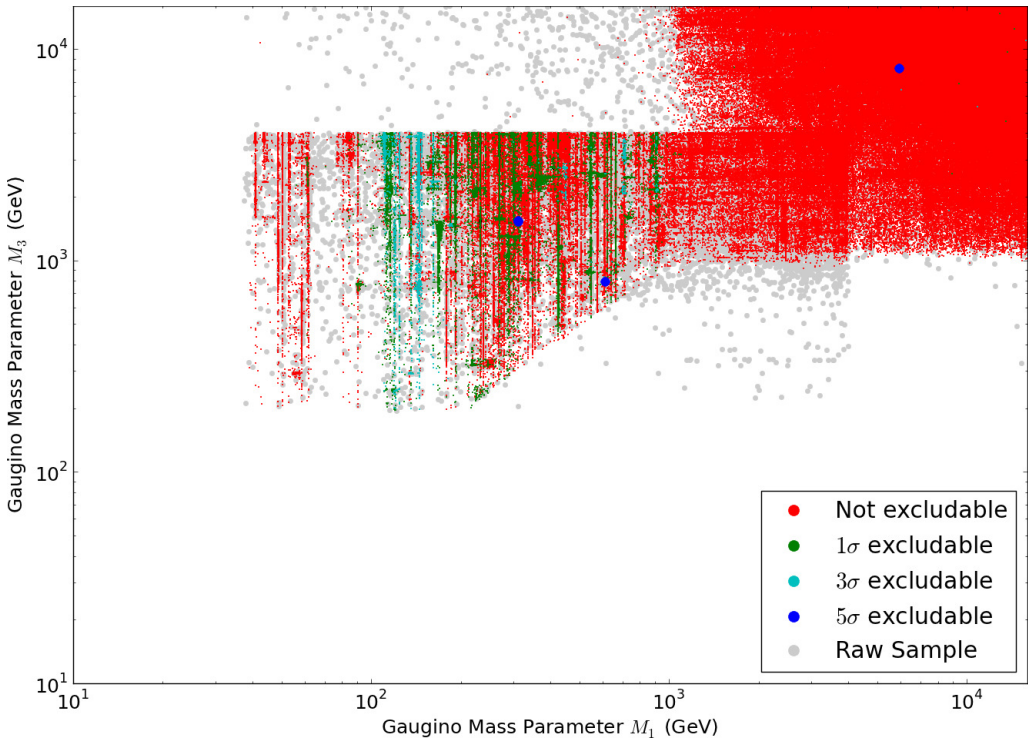


Figure 7.4: Gaugino parameters $M_1$ vs $M_3$, upper right quadrant of Fig. 7.3, with logarithmic axes to enhance view of inner region.

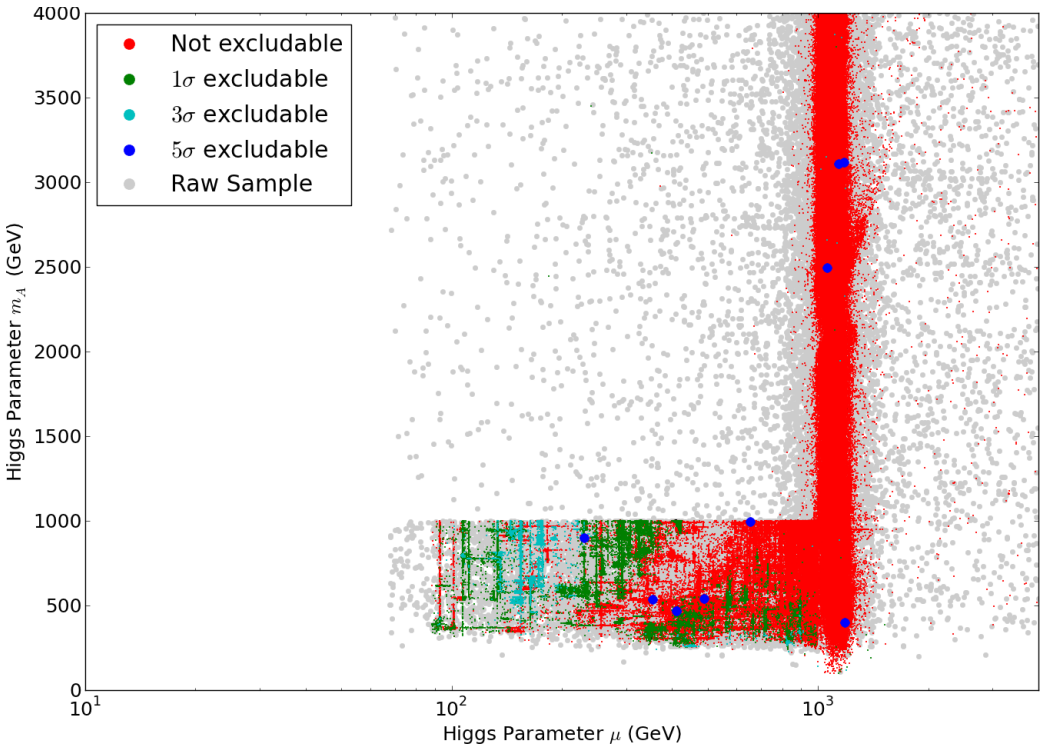


Figure 7.5: Higgs parameters $\mu$ vs $m_A$

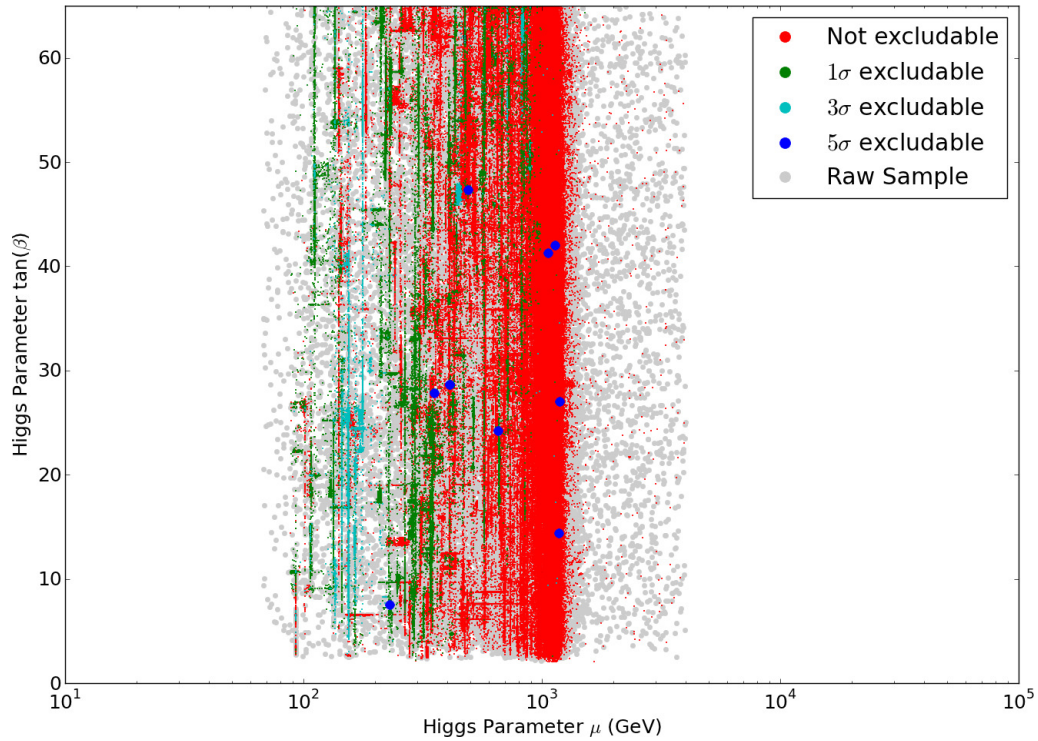


Figure 7.6: Higgs Parameters $\mu$ vs $\tan\beta$

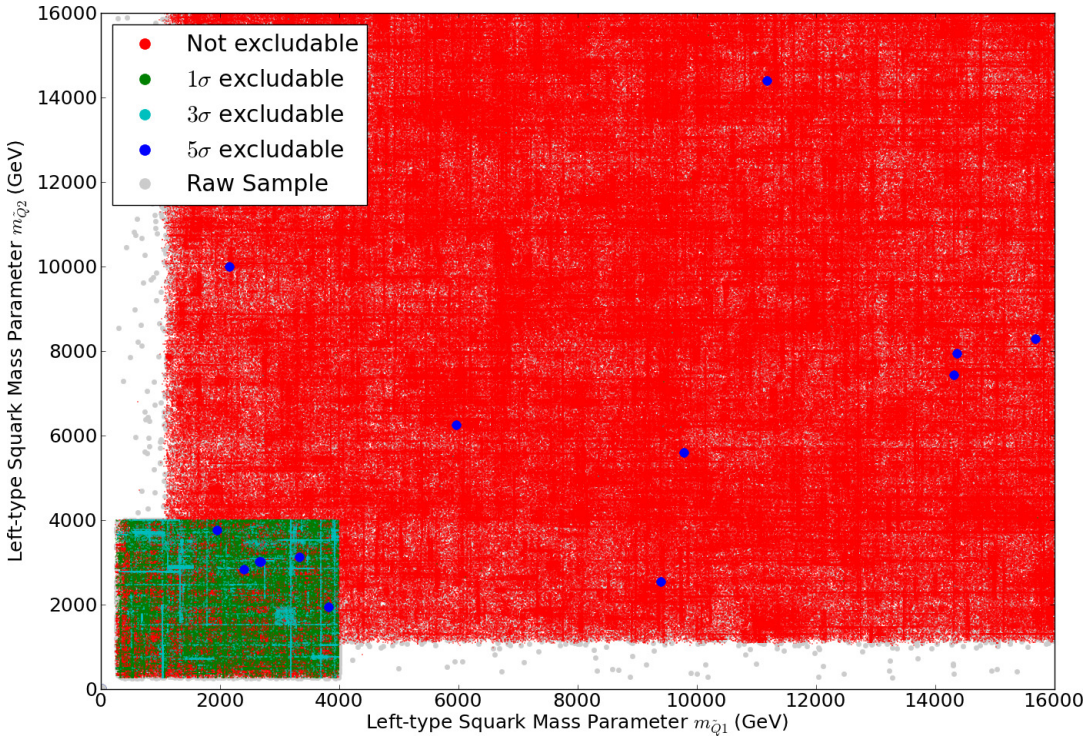


Figure 7.7: Squark Mass Parameters $M_{\tilde{Q}_1}$ vs $M_{\tilde{Q}_2}$. Colour coding as per Table 7.1 and previous figures

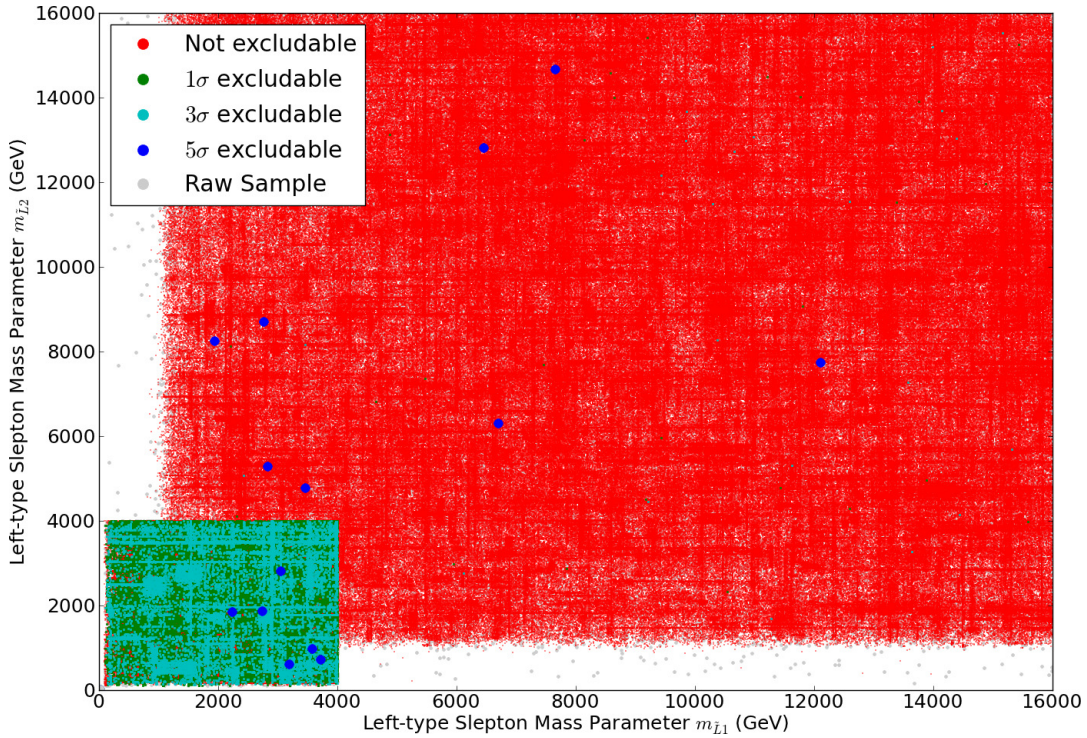


Figure 7.8: Slepton Mass Parameter $M_{\tilde{L}_1}$ vs $M_{\tilde{L}_2}$. Colour coding as per Table 7.1 and previous figures.

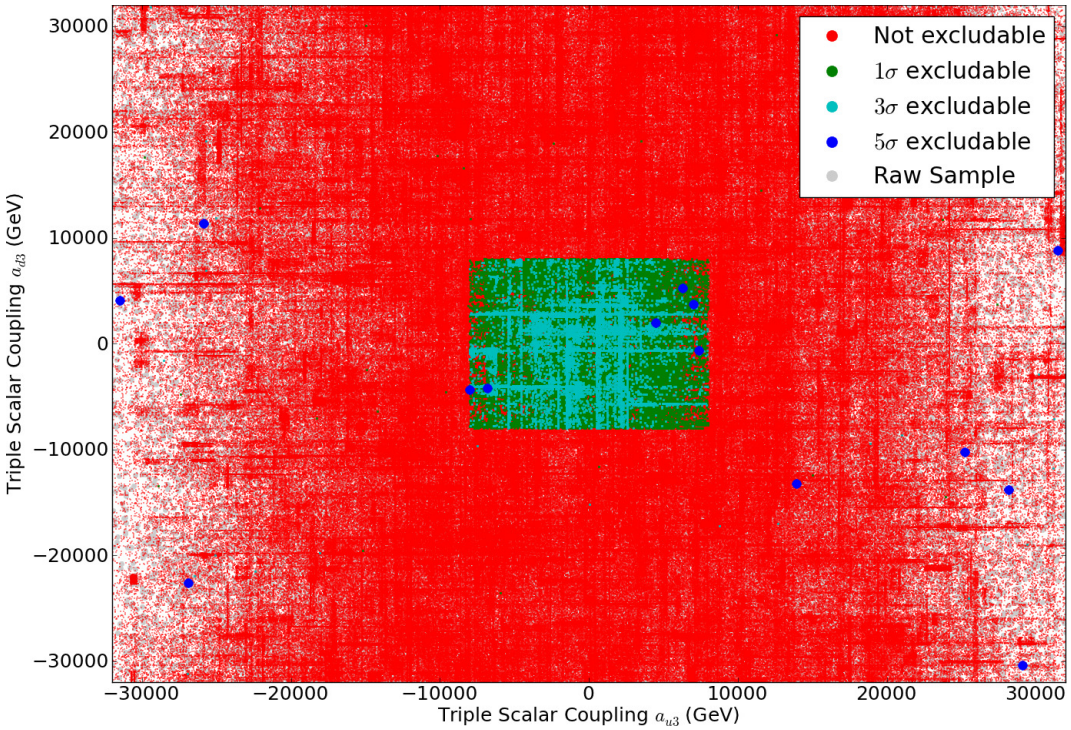


Figure 7.9: Triple Scalar Couplings $a_{u3}$ vs $a_{d3}$. Colour coding as per Table 7.1 and previous figures.

One question that arises from Figures 7.2, 7.4, 7.5, 7.7, 7.8 and 7.9 is why the area covered by the V data set is so predominantly red and devoid of green or cyan points. A related question is why there is such a sharp cut off between the two limit sets in Figure 7.7, 7.8 and 7.9; one might expect that there should be a smooth transition in the distribution of colours. These questions will be addressed in Subsection 7.2.4.

### 7.2.1 Gaugino Parameters

In Figures 7.1 and 7.3 the gaugino parameters $M_1$, $M_2$, and $M_3$ are plotted on regular axes. Given the high degree of symmetry in both axes the top right quadrant of both plots is then plotted on logarithmic axes in Figures 7.2 and 7.4 in order to enhance the view of the inner region.

A strong concentration of cyan points, which represent exclusion at a confidence level between $3\sigma$ and $5\sigma$, is present at $M_1 \approx 100 - 200$ GeV in Figure 7.2. A similar feature is apparent in Figure 7.4, the plot of $M_1$ against $M_3$. The $M_2$ and $M_3$ values that correspond to this cluster range from 200 GeV to 4000 GeV, the limit for these parameters in the W set. The band may well continue, but the simulations performed using the V set did not explore this region.

In both Figures 7.2 and 7.4 the effect of the relic density cut can be seen in the areas at the bottom of the plots which have grey points but no coloured points.

### 7.2.2 Higgs Parameters

In Figure 7.5 there is a large concentration of cyan points between $\mu \approx 100$ GeV and $\mu \approx 250$ GeV, with $m_A$ running from approximately 300 GeV to its W set maximum of 1000 GeV. As

with the cyan concentration in Figure 7.2 this feature may continue for higher $m_A$ value but the V data set did not explore this region. In fact the points arising from the expanded V limit set are highly concentrated around a line just above $\mu = 1000$ GeV. The distribution of grey points shows that the simulations did not sample the region of $m_A > 1000$GeV and $\mu < 1000$ GeV as extensively as it did the region around $\mu = 1000$ GeV.

The cause of this clustering becomes apparent when we look at Figure 7.10, where the relic density $\Omega_\chi h^2$ is plotted against the Higgs parameter $\mu$ for points from the random raw sample. The middle magenta line is the 7-year WMAP relic density measurement, with the two adjacent magenta lines demarcating the range of relic density values selected during later distillation.

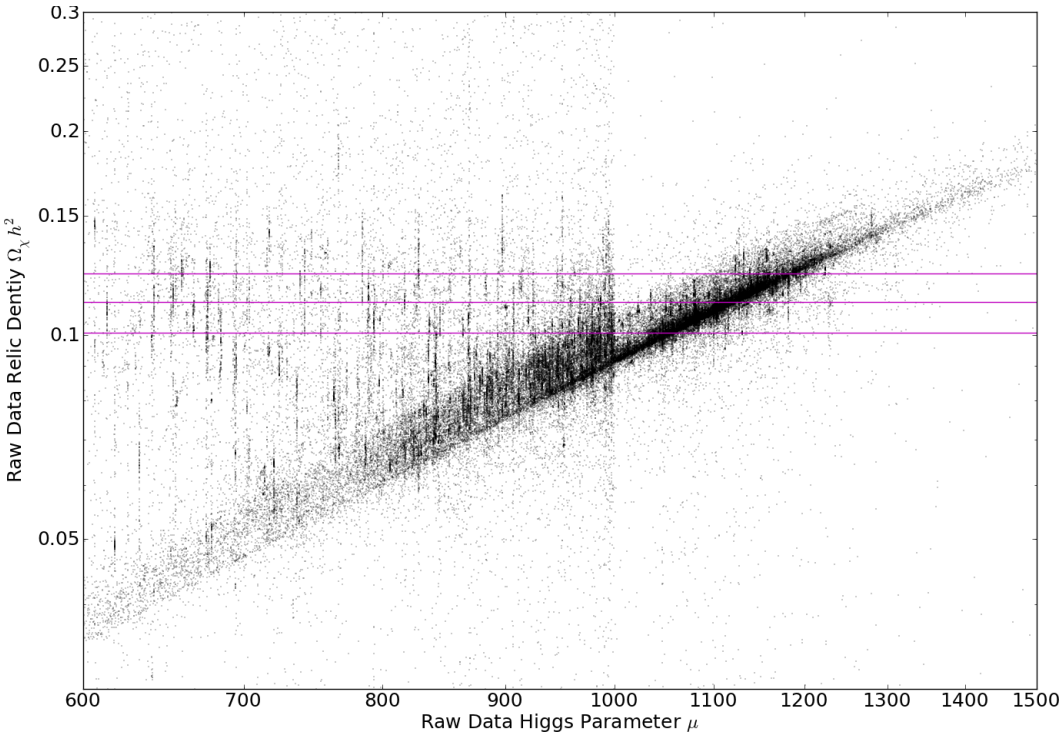


Figure 7.10: Raw data relic density $\Omega_\chi h^2$ as a function of raw data Higgs parameter $\mu$, from MSSM-25 simulations. The 7 year WMAP relic density measurement is plotted in magenta. The middle line is the stated value and the adjacent lines are plus and minus two uncertainties from this value.

A strong clustering of points has its centre intersecting with the WMAP relic density value. As laid out in Section 6.2 the VEGAS algorithm focuses its point selection around points which it has previously found to give relic densities close to the WMAP value. From Figure 7.10 we can see that there is an approximate relationship between the relic density and $\mu$; this not at all unsurprising as $\mu$ features in the calculation of neutralino mass (Equation 3.32), which goes on to play a key role in the relic density calculation (Subsection 3.4.2). So relic densities at and very close to the WMAP result occur for $\mu$ values just above 1100 GeV, and hence the VEGAS algorithm directs `adscan_mssm25` to focus point selection around this area. With the programme focusing so much of its attention on this area other regions of the $\mu$ parameter are neglected. The limits we set on future parameter space scans will have to be determined with this in mind; this region will have to be fenced off, as was unintentionally done with the W parameter limit set, so as to force `adscan_mssm25` to search other areas.

This cluster of red points circa $\mu = 1000$ GeV is repeated in Figure 7.6, however is not as distinct

due to both V and W sets having the same $\tan\beta$ range. The concentrations of cyan points in the range $\mu$=100 GeV to $\mu$=250 GeV seen in Figure 7.5 are present here also. They are spread out over the range of $\tan\beta$, though the concentration appears higher at lower $\tan\beta$.

### 7.2.3 Squark, Slepton Mass and Triple Scalar Coupling Parameters

Figures 7.7, 7.8 and 7.9 reveal no areas of particularly high exclusion confidence levels. The primary feature of note is the large swathes of red evident in the areas covered by the V limit set, the potential reasons for which will be outlined in Subsection 7.2.4. The value of $a_{u3}$ appears to affect the concentration of points with suitable relic density in Figure 7.9; the density of points decreases as $a_{u3}$ approaches its positive and negative bounds.

### 7.2.4 The Preponderance of Low Confidence Level Points in the V Data Limit Set

In Figure 7.5 we saw that almost all the points generated by simulations using the V parameter limit set had $\mu$ clustered around 1100 GeV and were coloured red, signifying a low exclusion confidence level. In other plots we also see that the vast majority of points derived from the V limit set are red; looking at Figures 7.1, 7.3, 7.7, 7.8, and 7.9, there is a multicoloured inner region bounded by the W set of parameter limits surrounded by a near uniform swathe of red points bounded by the V set of parameter limits.

The mechanism that caused the high concentration of V set points around $\mu$ around 1100 GeV was discussed in Subsection 7.2.2. The question now becomes how this value of $\mu$ leads to almost the entirety of these points having exclusion confidence levels of less than $1\sigma$.

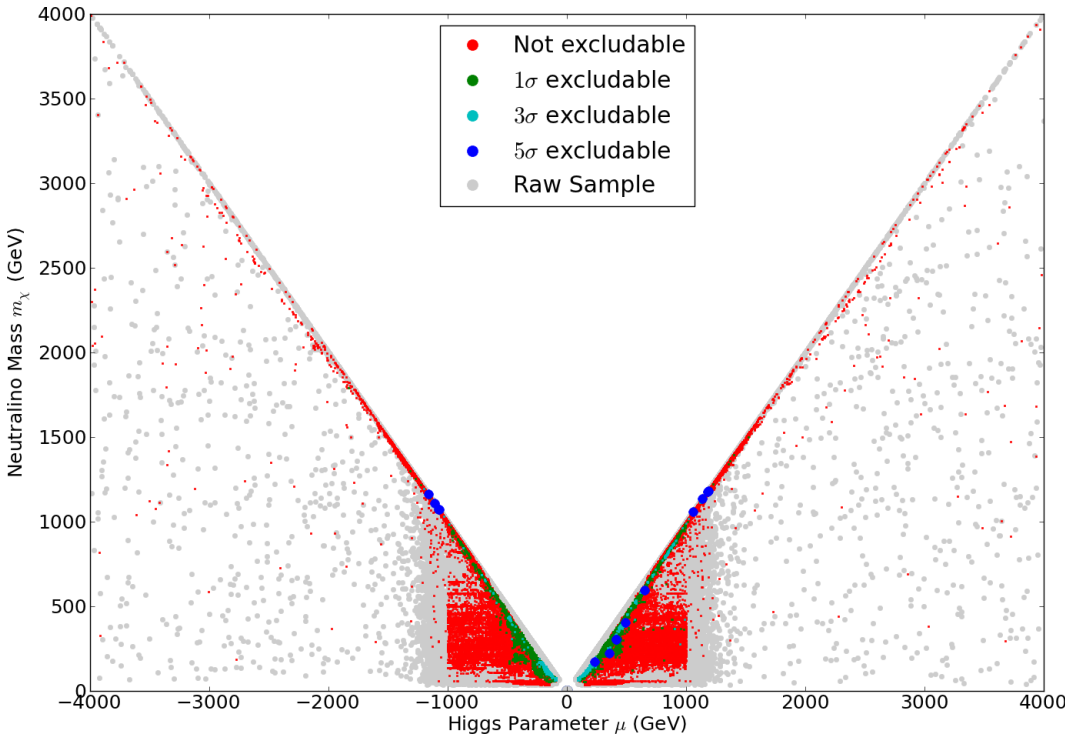


Figure 7.11: Neutralino mass $m_\chi$ against Higgs parameter $\mu$, from MSSM-25 simulations.

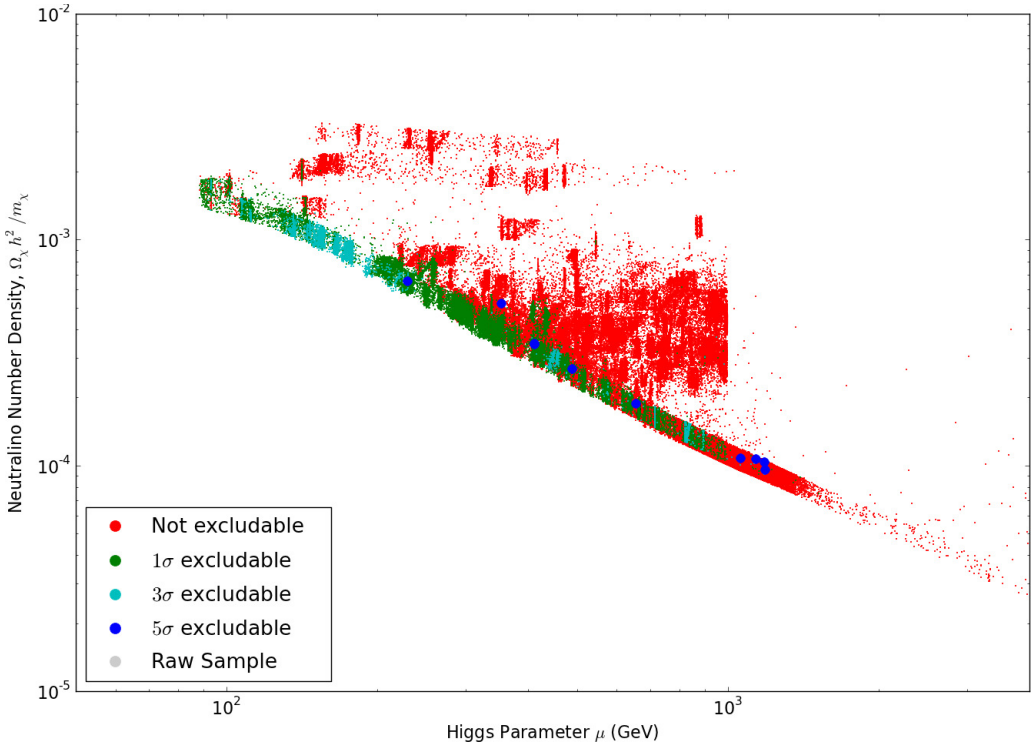


Figure 7.12: Neutralino relic number density $\frac{\Omega_\chi h^2}{m_\chi}$ as a function of Higgs parameter $\mu$, from MSSM-25 simulations.

Figure 7.11 illustrates a dependence between the neutralino mass $m_\chi$ and the absolute value of $\mu$. This in turn affects the number density of WIMPs in the halo - a higher WIMP mass effectively means that the same total halo mass can be achieved with few WIMPs. This relationship is born out in Figure 7.12, where a higher value of $|\mu|$ translates to a lower WIMP number density for a large majority of points.

Looking back at the calculation of the solar WIMP capture rate in Subsection 4.1.1 we can see in Equation 4.1.1 the dependence of the halo velocity distribution upon the number density through the term $\frac{\rho_\chi}{m_\chi}$. By tracing this term through Equation 4.3 and back into the capture rate formula 4.1 we can see that reducing the WIMP number density will in turn reduce the capture rate. Unfortunately the capture rate was not outputted for each MSSM-25 parameter point during the simulations, but we can get an indication of its value for each point via intermediary quantities. Decreasing the capture rate will in general reduce the number density of WIMPs inside the sun, which in turn will decrease the WIMP annihilation rate (Equation 4.21). A decrease in the solar annihilation rate decreases the solar neutrino flux in IceCube and the corresponding muon flux generated by these neutrinos. In Figure 7.13 we see this muon flux plotted against the $\mu$ parameter.

Around our point of interest at $\mu = 1100$ GeV we se a large clustering of points with very low muon flux. As the number of events in IceCube is derived from the observation of muon tracks a lower muon flux naturally corresponds with lower exclusion confidence levels. The muon flux in IceCube plotted in Figure 7.13 is calculated by taking the neutrino flux through IceCube and multiplying it by an energy-constant muon yield parameter. The signal used in the confidence level calculations however takes the neutrino spectrum and from this calculates the amount of signal based on muon production rates and the energy dependent effective area of IceCube. Thus

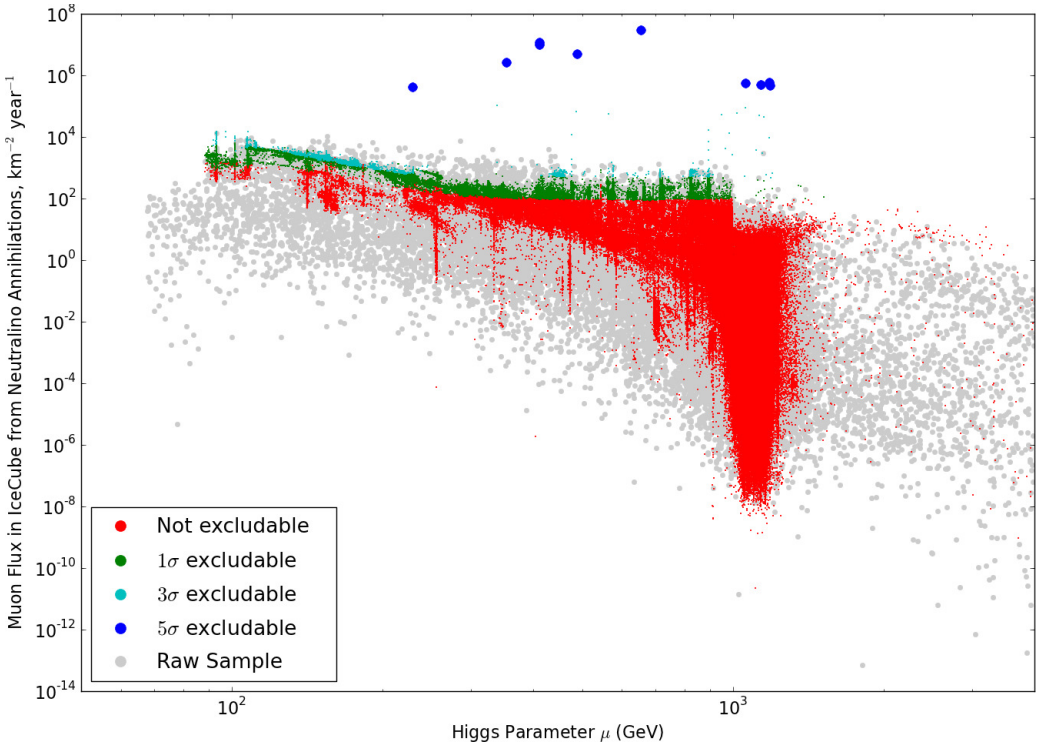


Figure 7.13: Muon flux in IceCube from solar neutrinos generated by neutralino annihilations, as a function of Higgs parameter $\mu$, from MSSM-25 simulations.

the muon flux plotted in Figure 7.13 does not have a one to one correspondence with IceCube signal, and hence the confidence level bands are not perfectly horizontal.

This final plot is the last piece in our chain of logic and gives credence to our theory. The root cause of the preponderance of red points found using the V limit set is due to the effects of the $\mu$ parameter. As shown in Figure 7.10 there is a relationship between $\mu$ and the relic density, and at $\mu \approx 1100$ GeV the model's relic density is at or very close to the WMAP result. This drives the VEGAS algorithm to focus point selection around $\mu \approx 1100$ GeV and neglect other possible $\mu$ values. This means that the vast majority of points in the V data set have $\mu$ around this value, and via the chain of reasoning given above, also have low exclusion confidence levels.

Figure 7.13 also tells us more about the large blue points that are scattered through the parameter space plots. We can see from this plot that they have extremely high muon fluxes, all above $10^6$ per km$^2$ per year. However, looking through the parameter space plots they do not appear to correspond with any particular parameter value. In Section 7.3 we shall see that these points have high spin-independent neutrino-nucleon cross sections as a common feature. Given the lack of any concentration in the parameter space the cause of these high spin-independent cross sections appears to be a precipitous combination of many parameters that happen to harmoniously combine in just the right way. Given their rarity - on the order of ten points out of a set of over 2.5 million - no solid conclusions can be drawn. If one wished to delve deeper into the parameter combinations that create these points a potential avenue would be to redefine the VEGAS importance sampling function $f$ to focus on high muon event rates.

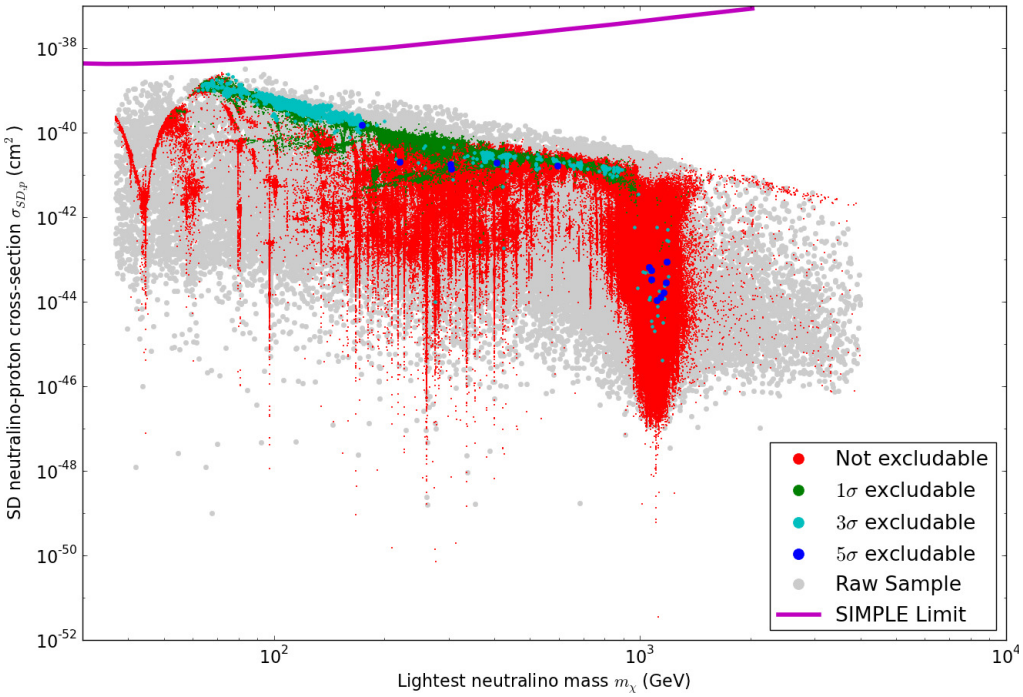


Figure 7.14: Spin-dependent neutralino-proton cross section $\sigma_{\mathrm{SD},p}$ as a function of neutralino mass $m_\chi$, from MSSM-25 simulations. Spin-dependent WIMP-proton cross section limit from SIMPLE direct detection experiment displayed as magenta line [28].

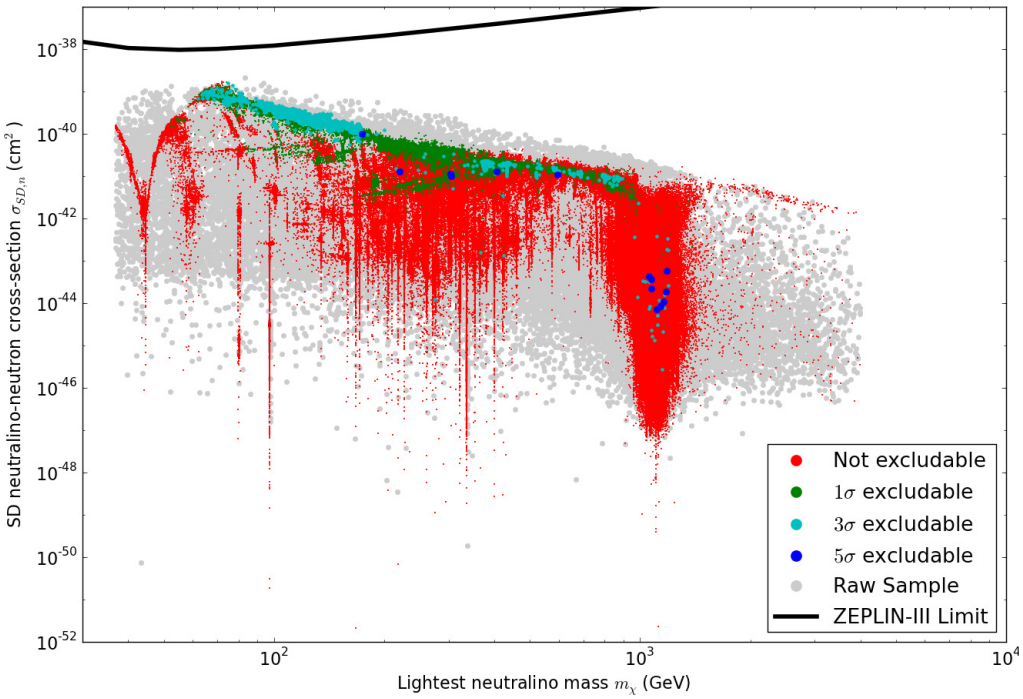


Figure 7.15: Spin-dependent neutralino-neutron cross section $\sigma_{\mathrm{SD},n}$ as a function of neutralino mass $m_\chi$, from MSSM-25 simulations. Spin-dependent WIMP-neutron cross section limit from ZEPLIN-III direct detection experiment displayed as black line [52].

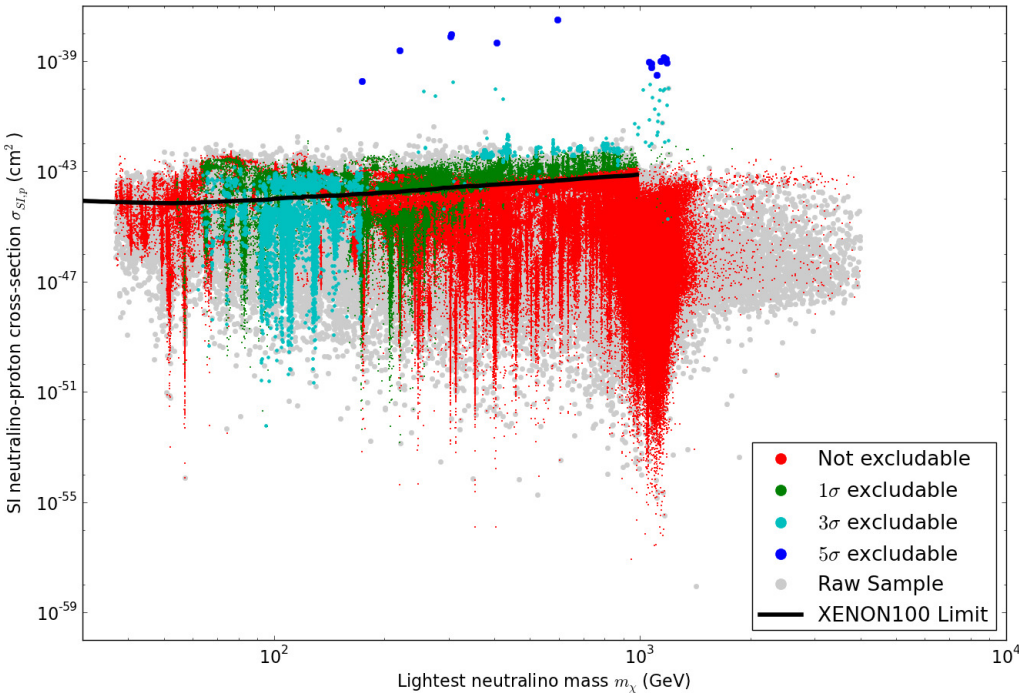


Figure 7.16: Spin-independent neutralino-proton cross section $\sigma_{\mathrm{SI},p}$ as a function of neutralino mass $m_\chi$, from MSSM-25 simulations. Spin-independent WIMP-nucleon cross section limit from XENON100 direct detection experiment displayed as black line [5].

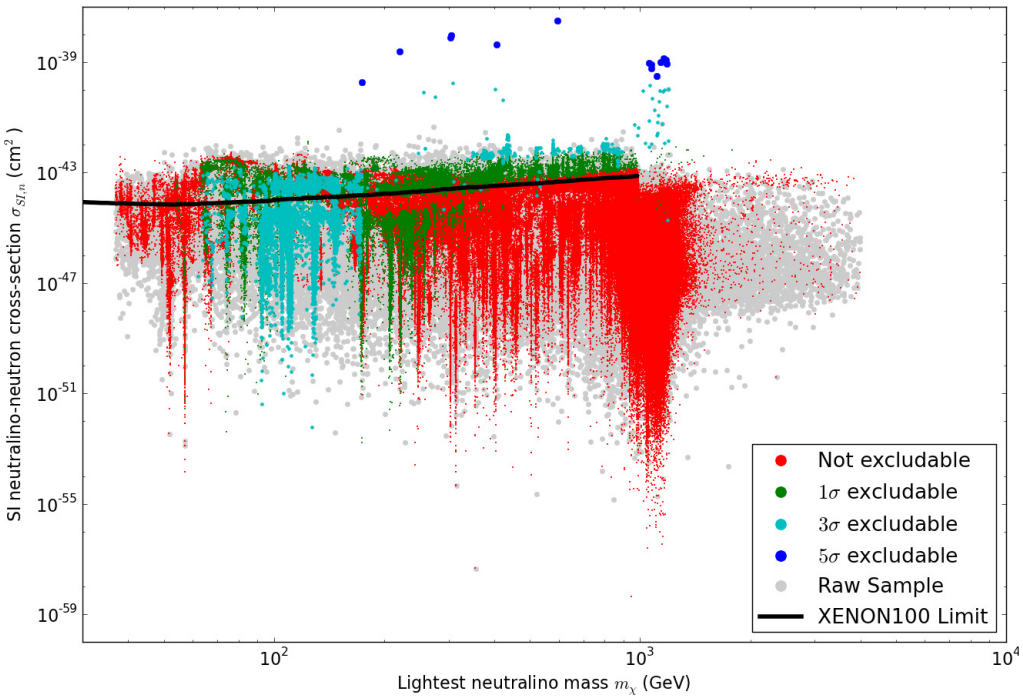


Figure 7.17: Spin-independent neutralino-neutron cross section $\sigma_{\mathrm{SI},n}$ as a function of neutralino mass $m_\chi$, from MSSM-25 simulations. Spin-independent WIMP-nucleon cross section limit from XENON100 direct detection experiment displayed as black line [5].

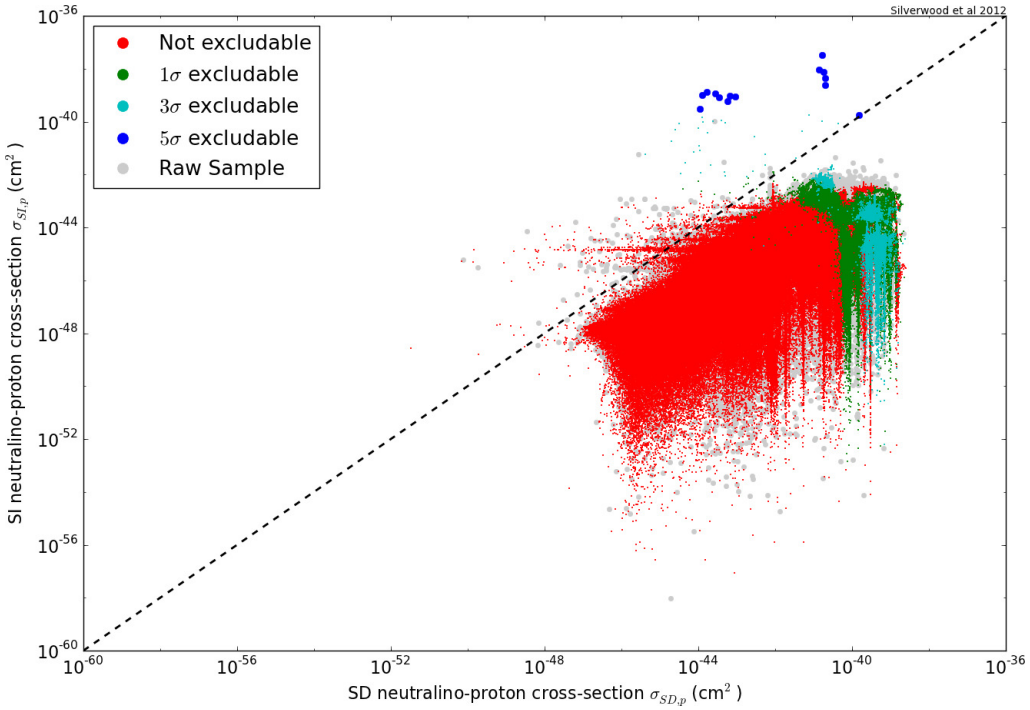


Figure 7.18: Spin-independent neutralino-proton cross section $\sigma_{\mathrm{SI},p}$ against spin dependent neutralino-proton cross section $\sigma_{\mathrm{SD},p}$, from MSSM-25 simulations.

## 7.3 Analysis of IceCube as an Indirect Dark Matter Detector

The IceCube Neutrino Telescope is a unique detector and offers us a new avenue for indirect dark matter detection. We now assess IceCube's efficacy in this role in light of information from scans of the MSSM-25 parameter space. This is performed by comparing interaction cross sections derived from our simulations to limits placed on these quantities by direct detector experiments.

Several points regarding the following plots and their interpretation should be noted. The direct detection limit data was obtained via the DMTools Beta website [34], and represents the best data available for a given interaction. WIMPs whose mass and cross section coordinates place them above the direct detection limit line are considered to be excluded with a confidence level as published by the experimental group; for the limits used here from SIMPLE, ZEPLIN-III and XENON100 this is 90%. The results we have obtained in this research do not give a solid line but instead assign exclusion confidence levels to individual points within the MSSM-25 parameter space. It is also important to recall that points with higher exclusion confidence levels are plotted over and so can exclude points with lower exclusion confidence levels. This means we have to be careful in interpreting these plots. An area of cyan on one of Figures 7.14 to 7.17 means that IceCube has exclusion capability for a certain range of interaction cross sections, a certain range of neutralino masses, *and* a certain set of other MSSM-25 parameters. In all of these plots areas of green and red can be seen in close proximity to areas of cyan. This means that beside a point that can be ruled out with a confidence level between $3\sigma$ and $5\sigma$ is a point that cannot be reliable ruled out at all.

Figure 7.14 displays the spin-dependent neutralino-proton interaction cross section against the neutralino mass for points generated by scans of the MSSM-25 parameter space. The magenta

line is the limit placed on WIMP-proton interaction cross section by the SIMPLE experiment [28], described in Subsection 4.2.3. Similarly Figure 7.15 shows the spin-dependent neutralino-neutron interaction cross sections, with limits from the ZEPLIN-III (Bonn-A) direct detection experiment, described in Subsection 4.2.2, displayed as the black line [52].

From these two plots we can see that none of the MSSM-25 parameter points found are above the exclusion limits set on spin-dependent interaction limits by the SIMPLE and ZEPLIN-III direct detection experiments. For these interactions the exclusion capability of IceCube thus exceeds that of SIMPLE and ZEPLIN-III, which give the lowest spin-dependent direct detection cross section limits currently available. This is understandable; increasing the sensitivity to spin-dependent interactions of one's detector relies for the most part on increasing the detector's mass and thus the number of nuclei a WIMP can potentially scatter on. While IceCube observes any such interactions indirectly through several intermediary processes, our 'target', the sun, is 30 orders or magnitude more massive than the targets used by SIMPLE or ZEPLIN.

Direct detection experiments can place much lower limits on spin-independent cross sections due to the enhancing effects of heavy nuclei, as described in Subsection 4.1.1. Figures 7.16 and 7.17 show the spin-independent interaction cross sections derived from MSSM-25 parameter points for protons and neutrons respectively. In both Figures the black line is the exclusion limit at 90% confidence level on spin-independent WIMP-nucleon interaction cross section from the XENON100 experiment [5].

As we can see from these two plots the XENON100 exclusion limit cuts into our data points and rules out a sizable fraction of them, including many cyan points and also the handful of extremely high signal points plotted as dark blue points. However there still remains a large number of cyan points below the line and hence not already excluded by XENON100. Thus, for certain regions of the MSSM-25 parameter space, IceCube has exclusion capability beyond that of the XENON100 direct detection experiment.

In light of the XENON100 exclusion limits we now revisit the spin-dependent neutralino-nucleon cross section analysis. The distilled MSSM-25 data set was reprocessed to extract a set of points with spin-independent neutralino-nucleon cross sections outside the exclusion limits set by XENON-100. In Figures 7.19 and 7.20 we take these points and plot the spin-dependent neutralino-proton cross section $\sigma_{\mathrm{SD},p}$ and neutralino-nucleon cross section $\sigma_{\mathrm{SD},n}$ respectively as a function of neutralino mass $m_\chi$. This reaffirms the exclusion capability of IceCube in regards to spin-dependent interactions - after the XENON100 cuts there are still strong clusters of cyan points below the limits set by the SIMPLE and ZEPLIN-III direct detection experiments.

Finally, Figures 7.16, 7.17 and 7.18 show that high spin-independent neutralino-nucleon cross section is the common element that links the blue points that were found to have extremely high signal rates. This would increase the capture rate and so tend to increase the neutrino signal for these points. However this high spin-independent cross section is also their undoing, as they all fall well inside the exclusion limits given by the XENON100 experiment.

## 7.4 Comparison of the MSSM-25 and MSSM-7 Parameterisations

Enlarging the parameter space of any simulation imposes additional computation burdens. Thus it is important to analyse the effects of such an enlargement so one can decide whether the use

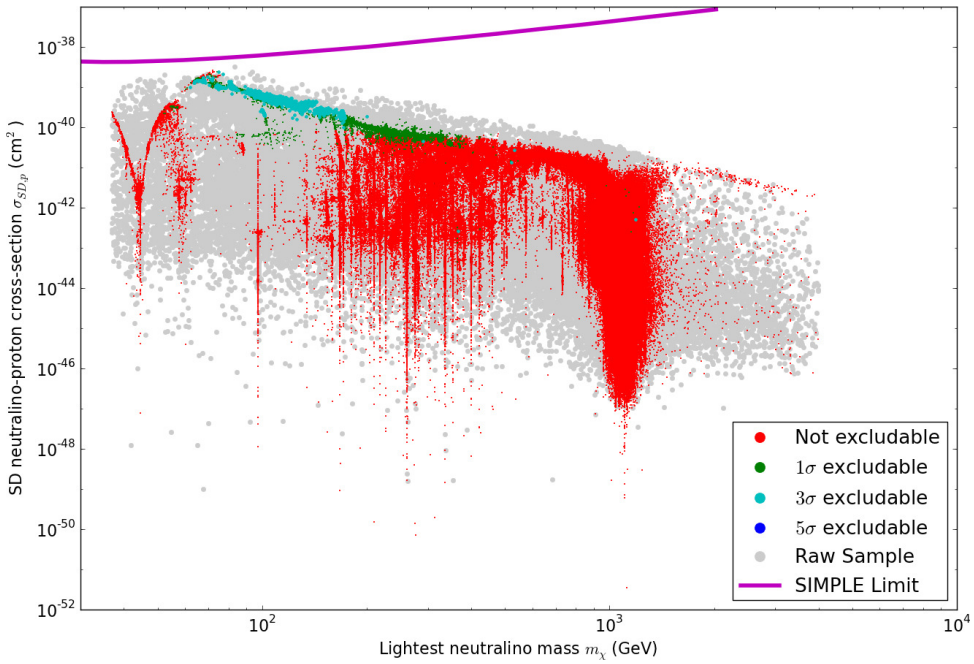


Figure 7.19: Spin-dependent neutralino-proton cross section $\sigma_{\mathrm{SD},p}$ as a function of neutralino mass $m_\chi$, from MSSM-25 simulations with points excluded by XENON100 limits [5] removed. Spin-dependent WIMP-proton cross section limit from SIMPLE direct detection experiment displayed as magenta line [28].

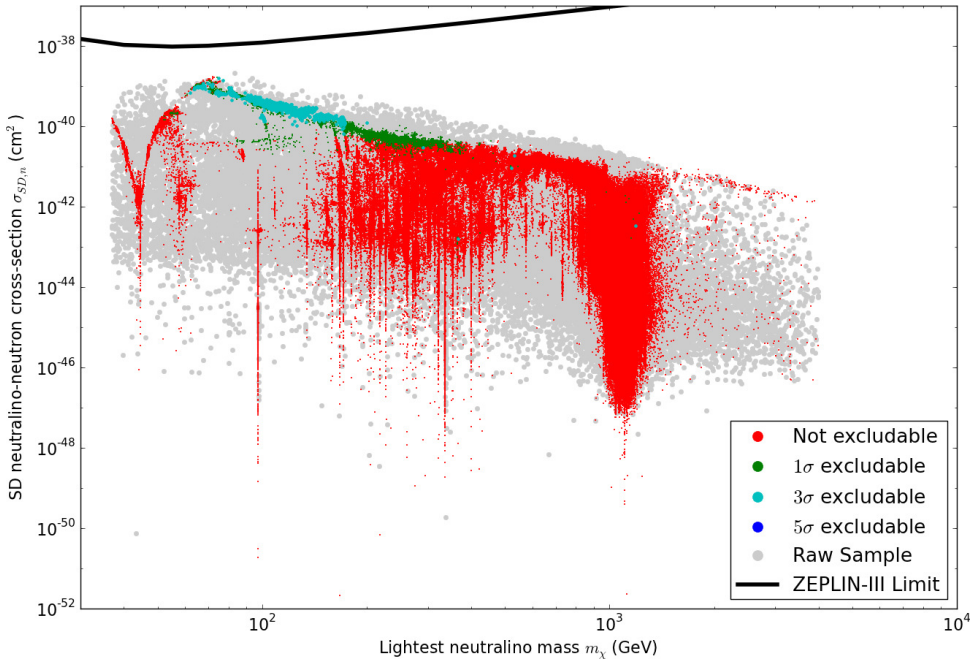


Figure 7.20: Spin-dependent neutralino-neutron cross section $\sigma_{\mathrm{SD},n}$ as a function of neutralino mass $m_\chi$, from MSSM-25 simulations with points excluded by XENON100 limits [5] removed. Spin-dependent WIMP-neutron cross section limit from ZEPLIN-III direct detection experiment displayed as black line [52].

of extra computational resources is justified. The data upon which the MSSM-7 plots are based upon is provided courtesy of Joakim Edsjö and Christopher Savage (Stockholm University) and Pat Scott (McGill University).

### 7.4.1 Direct Comparison of the Higgs Sector

For the most part comparisons can only be made between the observational quantities derived from the MSSM-7 and MSSM-25 parameter spaces as opposed to directly comparing parameters. The three parameters that describe the Higgs sector, $\mu$, $m_A$ and $\tan\beta$, are the exception as they are the same in both parameterisations. In Figures 7.21 and 7.22 the MSSM-7 Higgs parameter values are plotted, and can be compared to the MSSM-25 Higgs parameters plotted in Figures 7.5 and 7.6 respectively.

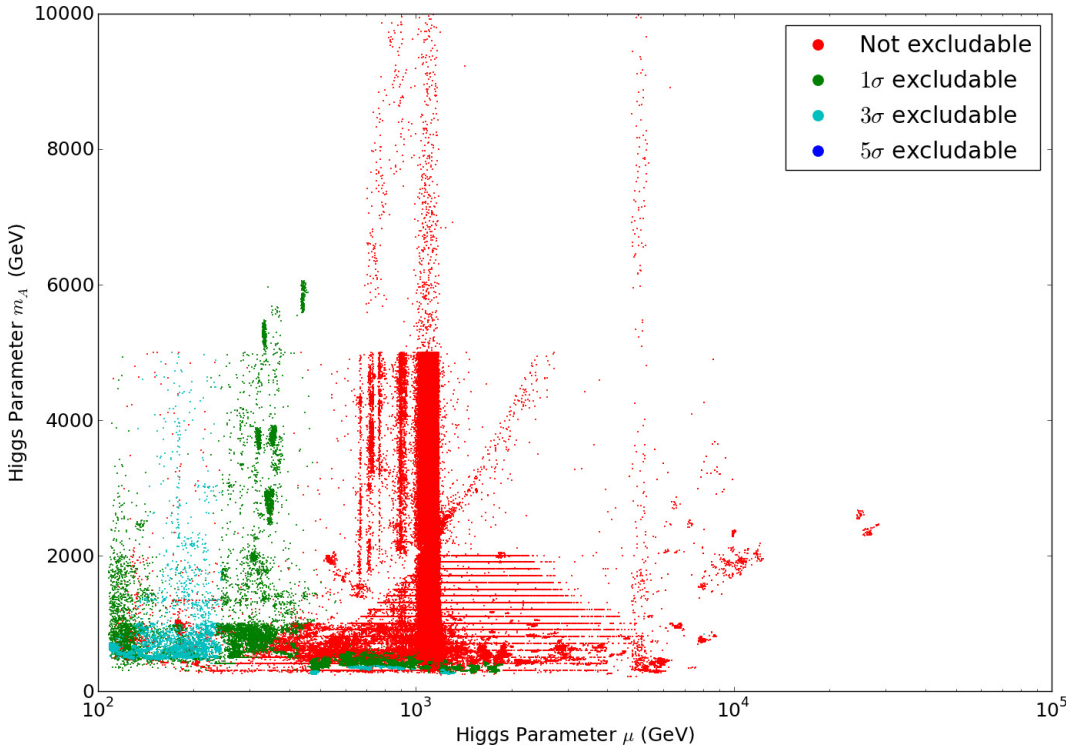


Figure 7.21: Higgs Sector $m_A$ against $\mu$, from MSSM-7 simulations. C.f. MSSM-25 data in Fig. 7.5

The first feature of note in Figures 7.21 and 7.22 is the high concentration of red points clustered around $\mu = 1100$ GeV. This is exactly the same feature we saw in the Higgs sector of the MSSM-25 parameterisation and investigated in depth in Subsection 7.2.4. The cluster of cyan points between $\mu \approx 100$ GeV and $\mu \approx 250$ GeV found in the MSSM-25 parameterisation is also present in the MSSM-7 parameterisation.

Through careful selection of simulation parameter limits by Joakim Edsjö the dominance of the $\mu \approx 1100$ GeV point has been minimised in the MSSM-7 data set. The area above $m_A = 1000$ GeV and below $\mu = 1000$ GeV has been searched fairly thoroughly, in stark contrast to the MSSM-25 simulations presented above. The dense region of cyan points between $\mu \approx 100$ GeV and $\mu \approx$250 GeV continues above $m_A = 1000$ GeV. This suggests that, if we set parameter limits to exclude the cluster at $\mu \approx$1100 GeV, we might see the cyan cluster extend further beyond

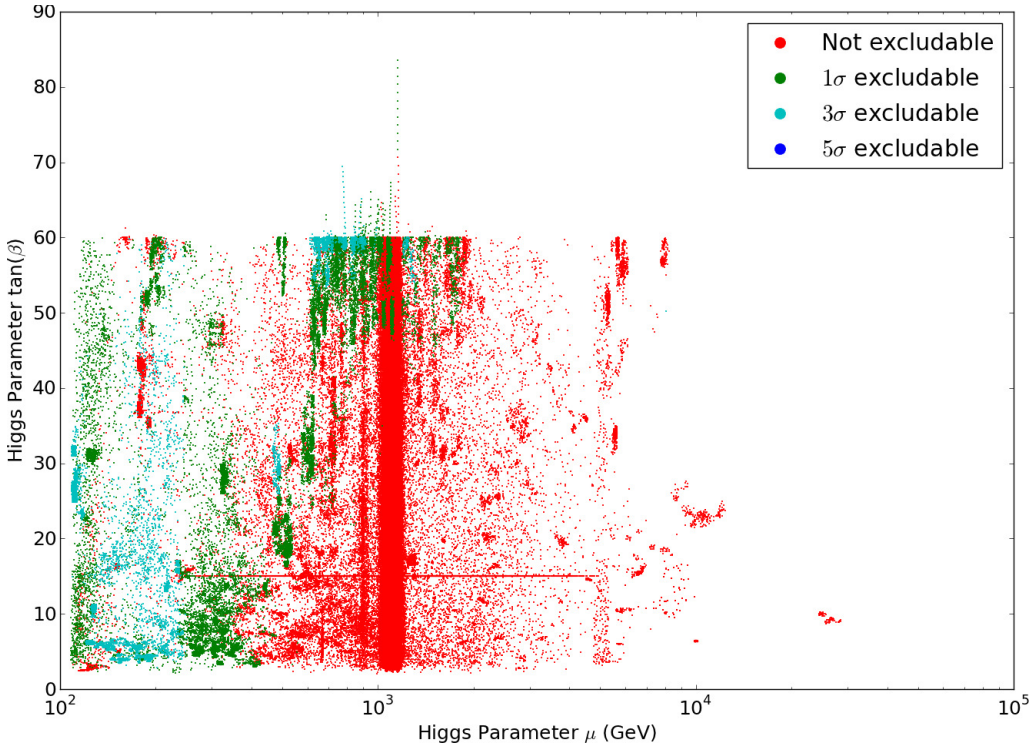


Figure 7.22: Higgs Sector $\tan\beta$ against $\mu$, from MSSM-7 simulations. C.f. MSSM-25 data in Fig. 7.6

$m_A = 1000$ GeV in the MSSM-25 simulations also.

### 7.4.2 Neutralino-Nucleon Cross Sections Revisited

In Section 7.3 plots of the neutrino-nucleon cross sections of the MSSM-25 parameter points and the corresponding direct detection limits provided insight into the capability of IceCube. For comparison we now present similar plots for the MSSM-7 data set in Figures 7.23, 7.24, 7.25, and 7.26.

The overall structure of the MSSM-7 neutralino-nucleon cross sections as shown in Figures 7.23 to 7.26 is similar to that of their MSSM-25 counterparts in Figures 7.14 to 7.17. The conclusions made regarding the exclusion capability of IceCube from the MSSM-25 data set remain the same for the MSSM-7 data set. The high concentration of cyan points around $m_\chi = 100$ GeV is present in the spin-independent cross section plots of both parameterisations (MSSM-7, Figures 7.25 and 7.26; MSSM-25, Figures 7.16 and 7.17) but its precise boundaries and distribution vary. The MSSM-25 parameterisation produced more cyan points with slightly higher neutralino mass and lower spin-independent cross section.

The patterns that appear in the red points of the plots of MSSM-7 neutralino-nucleon cross sections (Figures 7.23 to 7.26) are an artifact of the particular scanning method employed to generate the plots. As we can see from Figure 7.28 there are vertical lines of fixed $m_A$ value at regular 100 GeV intervals. This distribution is same as the patterns we see in Figures 7.23 to 7.26. These fixed $m_A$ values, when combined with other parameters, create the regular curved pattern seen in the neutralino mass. The regular, fixed $m_A$ values also appear in Figure 7.21, this time as horizontal lines. Such artifacts of search strategy appear unavoidable with `adscan` -

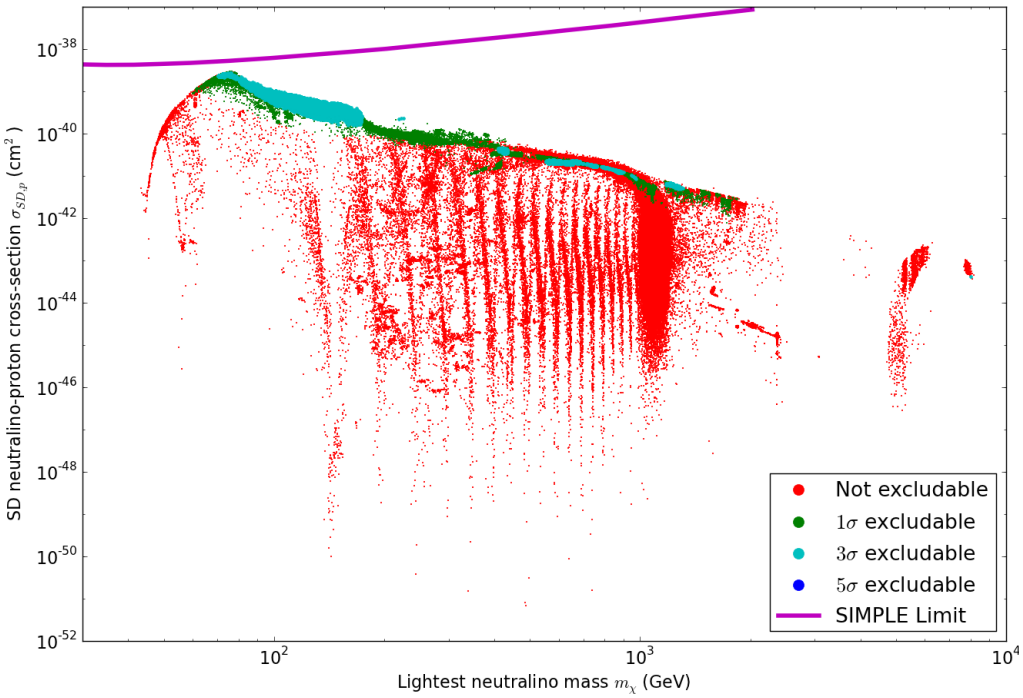


Figure 7.23: Neutralino mass $m_\chi$ against spin dependent neutralino-proton cross section $\sigma_{\mathrm{SD},p}$, from MSSM-7 simulations. C.f. MSSM-25 data in Fig. 7.14.

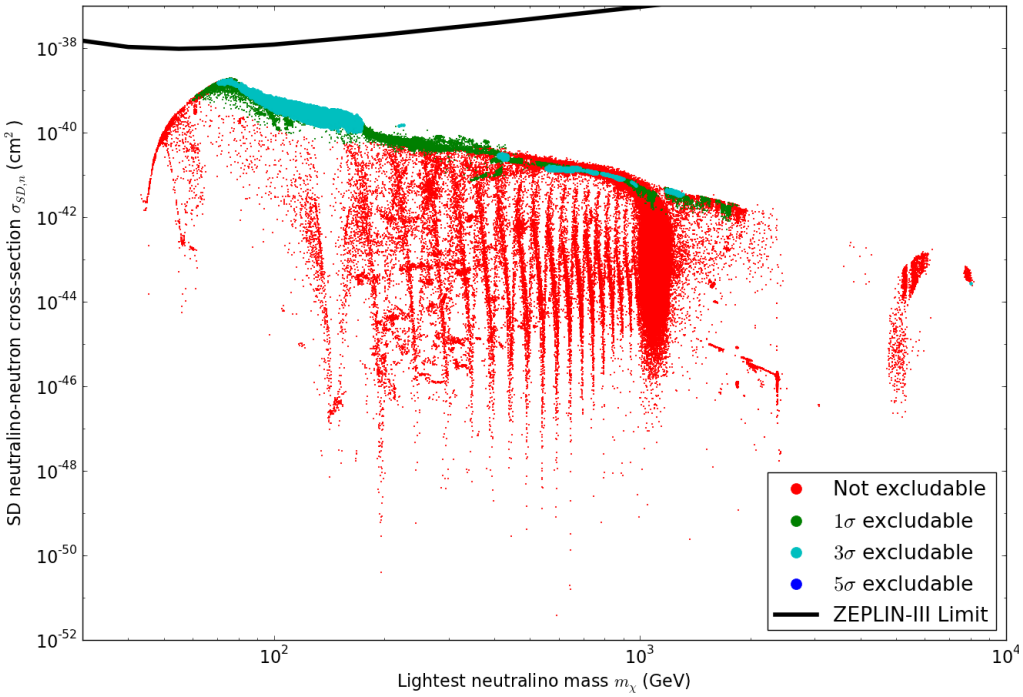


Figure 7.24: Neutralino Mass $m_\chi$ vs Spin Dependent Neutralino-Neutron Cross Section $\sigma_{\mathrm{SD},n}$, from MSSM-7 simulations. C.f. MSSM-25 data in Fig. 7.15.

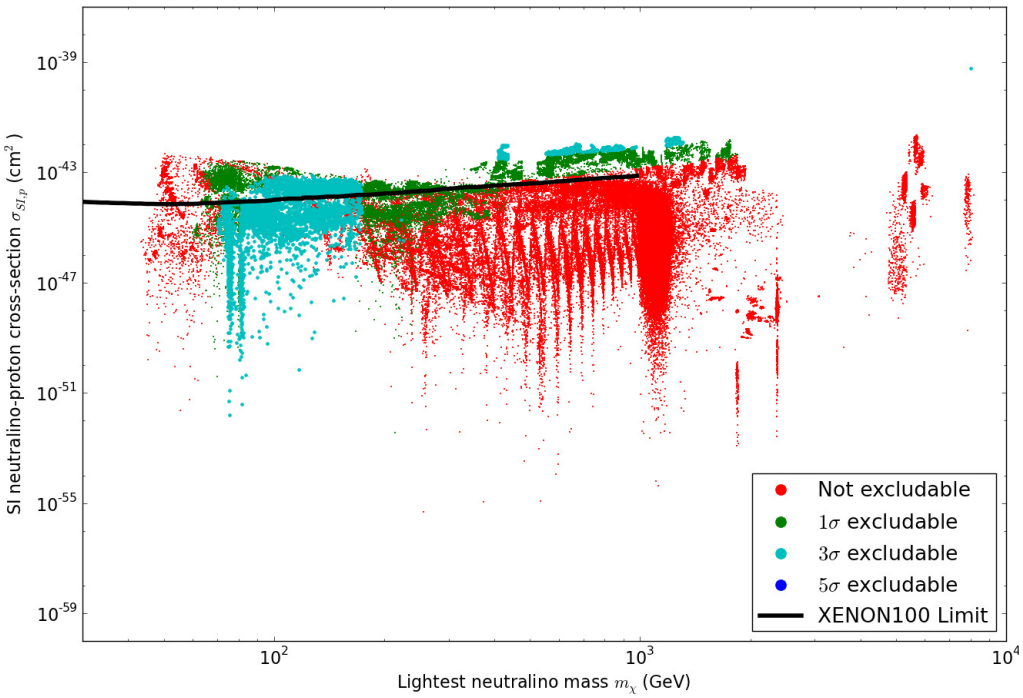


Figure 7.25: Neutralino Mass $m_\chi$ vs Spin Independent Neutralino-Proton Cross Section $\sigma_{\mathrm{SI},p}$, from MSSM-7 simulations. C.f. MSSM-25 data in Fig. 7.16.

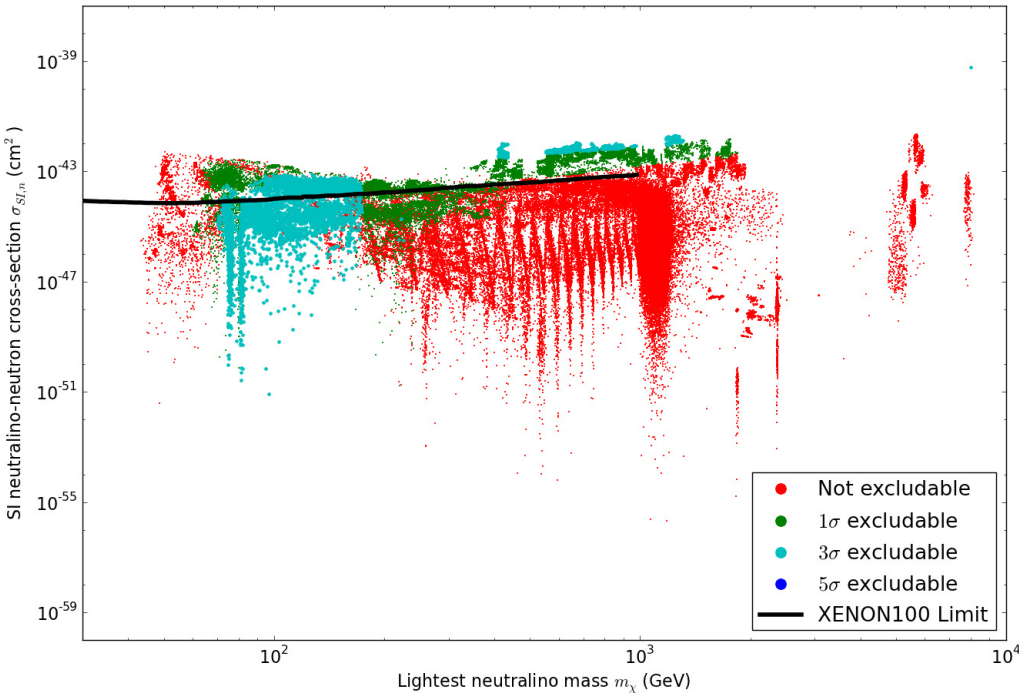


Figure 7.26: Neutralino Mass $m_\chi$ vs Spin Independent Neutralino-Neutron Cross Section $\sigma_{\mathrm{SI},n}$, from MSSM-7 simulations. C.f. MSSM-25 data in Fig. 7.17.

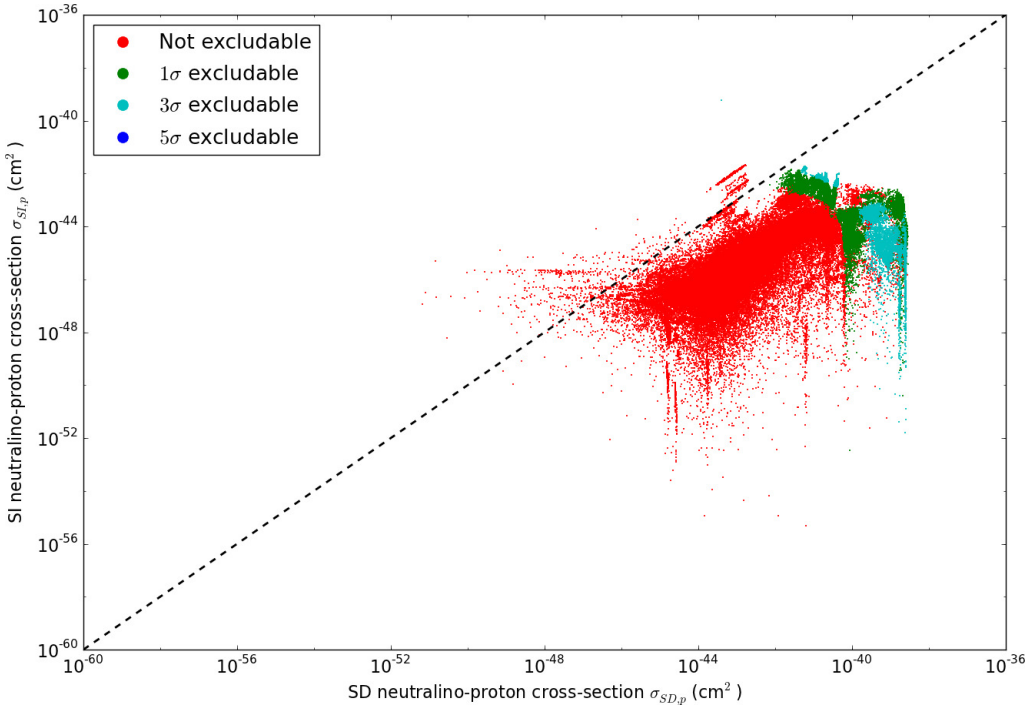


Figure 7.27: Spin-independent neutralino-proton cross section $\sigma_{\mathrm{SI},p}$ against spin dependent neutralino-proton cross section $\sigma_{\mathrm{SD},p}$, from MSSM-7 simulations. C.f. MSSM-25 data in Fig. 7.18.

the disjoints visible between the W and V limit sets and the high concentration around $\mu = 1100$ GeV in the V limit set can be considered artifacts of the search strategy used in this research.

Based on simulations using the MSSM-7 parameterisation Gustav Wikström and Joakim Edsjö derived estimates for the limits IceCube would be able to place on WIMP-nucleon scattering cross sections [84]. Given the similarity between the neutralino-nucleon cross section distributions for MSSM-25 and MSSM-7 parameterisations one can presume there will be no major changes in the limits derived in [84]. However a deeper analysis of this issue could be pursued in future work.

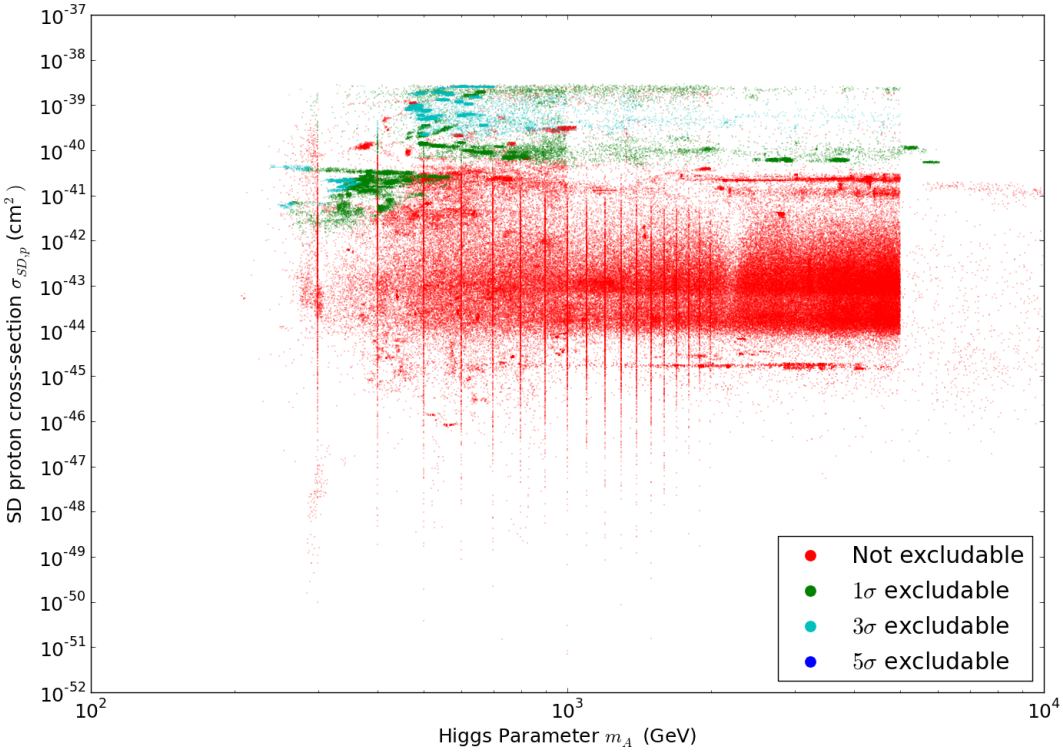


Figure 7.28: Spin-dependent neutralino-proton cross section $\sigma_{\mathrm{SD},p}$ as a function of Higgs parameter $m_A$, from MSSM-7 simulations.

# Chapter 8

# Conclusion

## 8.1 The Story So Far

The goal of the research presented in this thesis was the exploration of the 25 parameter Minimally Supersymmetric Standard Model from the perspective of indirect dark matter detection in the IceCube Neutrino Telescope.

Evidence for the existence of dark matter is abundant, as described in Chapter 2. The first clues came from the work of Fritz Zwicky in the 1930s on galaxy clusters [87; 88], and since then a wide body of evidence from multiple sources has been built up showing that the majority of mass in the universe consists of non-baryonic dark matter which interacts only via the weak force and gravity.

The observational signs of dark matter have also given us an idea of what it is and how it is distributed around the universe. Galactic rotation curves imply the existence of a spherical halo of dark matter surrounding galaxies [67; 68; 11]. The formation of large scale structures in the universe requires a certain amount of matter to be non-baryonic and non-dissipative. Surveys of large scale structure also indicate that the density of luminous and dark matter combined is $\Omega_{\mathrm{m}} \approx 0.29$ [62]. The abundances of certain elements is set through a process known as Big Bang Nucleosynthesis (BBN), and measurements of these abundances imply the density of luminous matter is $\Omega_{\mathrm{b}} \approx 0.04$ [46]. From the combination of these results we can conclude that the density of dark matter is $\Omega_{\mathrm{DM}} \approx 0.25$.

These figures for the densities of luminous and dark matter are confirmed and their precision improved by measurments of the Cosmic Microwave Background (CMB) by the WMAP satellite. The CMB is a relic of the very early universe, and anisotropies in its distribution are sensitive to the density of dark matter. From the 7-year WMAP measurements [51] we get a value for the dark matter relic density of

$$\Omega_{\mathrm{DM}} h^2 = 0.1120 \pm 0.0056. \tag{8.1}$$

Further evidence for dark matter is found through gravitational lensing, the process by which concentrations of mass bend light rays from distant sources and focus them towards an observer. This technique has been used to study the distribution of dark matter [56; 80], and also has been used to observe the collision of two galaxy clusters [16].

Despite the abundance of observational evidence there is still no definite answer as to what type of particle or particles dark matter consists of. The most promising candidates are a

class of particles known as WIMPs, or Weakly Interacting Massive Particles. One example of a WIMP is the neutralino, a hypothetical particle suggested by a theory known as Supersymmetry.

Supersymmetry (SUSY) is an extension of the Standard Model (SM), a theory which has been out guide to particle physics for more than 30 years. The SM described two distinct classes of particles, fermions and bosons. SUSY posits the existence of a symmetry linking the two groups of particles. However this cannot be achieved with the particles that normally make up the SM, so SUSY brings with it a new set of supersymmetric particles known as superparticles or sparticles. SUSY links the SM fermions to bosonic sparticles known as sfermions, and the SM bosons are linked to fermionic sparticles known as bosionos.

In generating masses for these particle the gauge-eigenstates of the neutral bosinos mix to create mass eigenstates known as neutralinos, which are neutral and weakly interacting. Conditions imposed to ensure the stability of the proton have the welcome side effect of making the lightest supersymmetric particle (LSP) stable. In certain regions of the SUSY parameter space the neutralino is the LSP, and thus it is a suitable WIMP dark matter candidate.

There are many different types of SUSY, but this research focuses on one type known as the Minimally Supersymmetric Standard Model. It consists of the SM combined with the minimum amount of extra machinery necessary to make it supersymmetric. Many aspects of the MSSM are as yet unknown and are quantified by 105 free parameters. Through the application of informed assumptions some of these 105 parameters can be set to zero or combined with other parameters. Thus the full 105 dimensional MSSM parameter space can be reduced to more manageable sizes. For this research a 25 dimensional parameter space was used, with comparisons being made to previous work performed with a seven dimensional parameter space.

Methods for detecting these neutralinos can be divided into two categories, direct and indirect. Direct detection methods are based on the idea that as the Earth moves through the galaxy it is also moving through the dark matter halo, so there is a constant flux of these particles through the Earth. WIMPs from the halo will occasionally interact with the luminous matter as they pass through the Earth, and by building a suitable target it could be possible to observe one of these interactions. The interactions between neutralino WIMPs and the nuclei of atoms can be divided into spin-independent and a spin-dependent pieces. The strength of the spin-independent piece is determined by the mass of the target nuclei and the spin-independent WIMP-nucleon scattering cross section, while the strength of the spin-dependent piece is determined by the total spin of the nuclei and the spin-dependent WIMP-nucleon scattering cross section [47].

The other method, indirect detection, aims to infer the presence of dark matter through any secondary particles it produces. Neutralino WIMPs can interact and annihilate with each other, thus producing a source of potentially detectable SM particles. $\gamma$-rays could be produced by neutralino WIMPs in the halos of the Milky Way and other galaxies [75], and these could be detected by the Fermi-LAT satellite [6].

Just as the neutralino WIMPs of the halo can interact with the nuclei of a direct detection experiment's target volume, they can also interact with nuclei of the sun. If they lose sufficient energy in these interactions the neutralinos can become permanently trapped in the sun. As they undergo further scatterings they will drop down into successively smaller orbits, eventually concentrating in the sun's core [39; 71]. The increased concentration of neutralinos will lead to an increased number of neutralino self-annihilations. The SM particles created by these self-

annihilations can themselves produce neutrinos which can escape the sun [47]. Thus there will be a signal of neutrinos emanating from the sun which we could detect, and so in turn infer the existence and properties of neutralino WIMP dark matter.

To detect these neutrinos we use the IceCube Neutrino Observatory, which consists of a cubic kilometer of extremely transparent natural ice deep below the South Pole. This has been instrumented with 5160 Detector Optical Modules (DOMs), which detect the faint flashes of light emitted when neutrinos interact with nuclei in the ice. Based on the amount and distribution of the light emitted we can determine the energy and direction of the incident neutrino.

The way we use IceCube to explore the MSSM-25 parameter space is through parameter exclusion. From a set of 25 parameters we can calculate the rate of neutralino capture and annihilation in the sun, and from this, calculate a figure for how many neutrinos IceCube would see if such a model were correct. From simulations of background sources we can also predict how many neutrinos IceCube would see if there were no neutralino annihilations in the sun. In the absence of real data from IceCube we assume that the only neutrinos we see are those from background sources, and given that assumption, we then calculate how confident we are in excluding a point in the parameter space. For example, if a certain set of parameters predicts that IceCube would see a very high number of neutrinos then we could be very confident in ruling out that model, because if were correct, it is very likely we would see it. In other words we could exclude this point in the parameter space with high confidence level. On the other hand, if another set of parameters predicts a that IceCube would see very few neutrinos originating from neutralino annihilation then we would be less confident in ruling out this set, as it would be very likely that this model could be true but we are simply unable to distinguish it from the background. In this case we could only exclude this point with low confidence level.

The process of taking a set of 25 parameters and calculating the observables it predicts, such as sparticle masses, coupling constants, and exclusion confidence levels, is automated by the `DarkSUSY` software package [38].This package was modified as part of this research to make it compatible with MSSM-25 models. To pick which points in the 25-dimensional parameter space to test we use the VEGAS algorithm, which uses Monte-Carlo methods to focus the search on areas which produce relic densities that closely match the figure given my WMAP. As discovered during this research this method has its limitations and foibles which must be taken into consideration.

The VEGAS algorithm was implemented in a FORTRAN programme called `adscan_mssm25`. Points selected by the VEGAS algorithm are checked against two criteria: first, they must produce physical results, and second, they must produce observables that do not conflict with current limits set by accelerator experiments. 8.25 million such points were found during this research. A random sample of 250,000 of these 8.25 million points was extracted for analytical purposes.

A further cut was placed on the neutralino relic density predicted by each of the 8.25 million points. Only points that passed this cut had their exclusion confidence levels calculated, as this process is computationally intensive. The cut extracted points with relic densities within two uncertainties of the 7-year WMAP measurement, i.e. in the range $0.1120 - 0.0112 \leq \Omega_\chi h^2 \leq 0.1120 + 0.0112$. 2.59 million points with suitable relic density were found and fed into the exclusion confidence level calculations, along with the random sample extracted earlier.

This data set was then analysed with the goal of answering three main questions: what, if any,

regions of the MSSM-25 parameter space could be excluded by IceCube; what is the utility of IceCube as a indirect dark matter detector; and what are the advantages of using the MSSM-25 parameterisation over the smaller, less computationally intensive MSSM-7 parameterization.

## 8.2 Research Conclusions

The first question posed in Chapter 7 was whether there were any areas of the MSSM-25 parameter space that could be excluded by results from IceCube, assuming no excess above expected background was observed. Answering this question involved plotting the distribution of points across the parameter space and looking for clusters of points colour coded in cyan or blue, which indicated exclusion confidence levels between $3\sigma$ and $5\sigma$ and above $5\sigma$ respectively. Only a handful of blue points were found, and their distribution appeared random. Clusters of cyan points were found for $M_1$ between approximately 100 GeV and 200 GeV (Figures 7.2 and 7.4), and for $\mu$ between approximately 100 GeV and 250 GeV (Figure 7.5). No other high concentrations of cyan points were found. Further regions of high excludability may exist within the boundaries set by our parameter limits, but issues related to search strategy, discussed further below, precluded a full search of all parameter values.

The advantage of IceCube for indirect dark matter detection is shown clearly in Figures 7.19 and 7.20. The cyan clusters represent regions that can be excluded by IceCube but are beyond the reach of current direct detection experiments.

The benefit of expanding the parameter space from seven to 25 parameters can be seen by comparing the MSSM-25 Figures 7.16 and 7.17 to their MSSM-7 counterparts, Figures 7.25 and 7.26. The MSSM-25 parameterisation produced cyan points with higher neutralino mass and lower spin-independent cross section. The MSSM-25 parameterisation shows that IceCube's exclusion capability extends further than the MSSM-7 parameterisation predicts.

## 8.3 Future Work

The set of parameter space points produced as part of this research represents a wealth of information about the 25 dimensional parameterisation of the MSSM. Further analysis of this data set is possible, investigating aspects such as the effect of the gauge eigenstate composition of the neutralino on various observables, the predicted gamma ray spectrum from dark matter in the halo, and as mentioned earlier, a reinvestigation of the limits IceCube can place on WIMP-nucleon scattering cross sections.

As described by Subsection 7.2.4 certain regions of the parameter space were neglected by the search algorithm. The data derived from the V limit set was dominated by points with $\mu$ values of approximately 1100 GeV, which in turn constrained certain observables into specific regions. As such future work will include performing further parameter scans with a region around this value of $\mu$ fenced off.

More advanced methods of searching the parameter space can also be implemented. One such example would be Monte Carlo Markov Chains as implemented in the `SuperBayeS` software package [30; 79], which utilizes Bayesian techniques to achieve improved computational efficiency. As with `DarkSUSY` modifications will be necessary to make `SuperBayeS` compatible with 25 parameter models.

## 8.4 Acknowledgements

15 months. One king-hell earthquake, three major aftershocks and countless minor shakes. 35,000 kilometers from here to Stockholm and back. And another 17,000 kilometers back to Europe soon to come.

A big thank you of course goes to my supervisors here at the University of Canterbury, Jenni Adams and Anthony Brown. Both have been a constant source of advice and support, kept me on track, and helped me see the bigger picture of my research. Their contribution would be exemplary even during normal years, and 2011 has been about as far from normal as you can get. Additionally it was through Jenni's connections within the IceCube collaboration that I was able to collaborate with researchers from across the globe, who included...

...Pat Scott of McGill University in Montreal. (To paraphrase Capt. Willard...) Everyone gets everything he wants. I wanted a mission, and for my sins, he gave me one. Pat has been my main contact point with the SUSY parameter scans project and has been a third, unofficial supervisor. I've learned a huge amount from Pat and I owe him a big debt of gratitude. And many beers in Amsterdam. Cheers Pat!

Thanks also to all the people at Stockholm University, not only for help with research but also for such an awesome time while I was there. Prof. Joakim Edsjö, who arranged for me to visit Stockholm for two weeks as part of this research. Christopher Savage who has helped with many technical issues over the last year. Joakim, Chris and Pat are the guys behind the MSSM-7 data set, the lack of which would doom a third of my conclusion. Matthias Danninger, whose IceCube background simulations this entire analysis depends on. Tack!

This thesis has relied heavily on computing, so a big thanks goes to Tim Delany and Orlon Petterson, the Physics Department IT technicians, for helping with software problems and hooking me up with computers for processing work.

A lot of people have contributed to this thesis simply by keeping me fed and sane, and to y'all some massive props are owed. My friends and flatmates Rachael Hemmingsen, Dimitri Schritt, Danelle Powell, Abbas Rahman and Tom Flikac, who have supplied me with cake, chocolate, stew, strawberries, aerial resupply of rocky road, muffins, and in general good humour and support through not just the last month of writing but also the utterly insane year we've had here in Christchurch. Colleagues and office mates in the University of Canterbury Physics Department, supplying books, advice and camaraderie as I've travelled up the Nung river of research. The Osbornes, my whanau, who put a roof over my head when I came back from Cambridge and who have always been there through the good times and the bad. My sister Monica, whose voice I hear every time I want to use the word 'aforementioned', and who has given support, advice, and perhaps most importantly, a bottle of gin to mark the conclusion of this thesis. And its good gin too. South Gin.

# Bibliography


[1] R. Abbasi et al., *Limits on a muon flux from neutralino annihilations in the sun with the icecube 22-string detector*, Physical Review Letters, 102 (2009), p. 201302.

[2] S. S. Abdussalam, B. C. Allanach, F. Quevedo, F. Feroz, and M. Hobson, *Fitting the phenomenological mssm*, Physical Review, 81 (2010), p. 095012.

[3] I. Aitchison, *Supersymmetry in Particle Physics*, Cambridge University Press, 2007.

[4] W. Altmannshofer and D. M. Straub, *Viability of mssm scenarios at very large* $\tan\beta$, Journal of High Energy Physics, 2010 (2010).

[5] E. Aprile, K. Arisaka, F. Arneodo, A. Askin, L. Baudis, A. Behrens, K. Bokeloh, E. Brown, T. Bruch, G. Bruno, J. Cardoso, W.-T. Chen, B. Choi, D. Cline, E. Duchovni, S. Fattori, A. Ferella, F. Gao, K.-L. Giboni, E. Gross, A. Kish, C. Lam, J. Lamblin, R. Lang, C. Levy, K. Lim, Q. Lin, S. Lindemann, M. Lindner, J. Lopes, K. Lung, T. Marrodán Undagoitia, Y. Mei, A. Melgarejo Fernandez, K. Ni, U. Oberlack, S. Orrigo, E. Pantic, R. Persiani, G. Plante, A. Ribeiro, R. Santorelli, J. Dos Santos, G. Sartorelli, M. Schumann, M. Selvi, P. Shagin, H. Simgen, A. Teymourian, D. Thers, O. Vitells, H. Wang, M. Weber, and C. Weinheimer, *Dark matter results from 100 live days of XENON100 data*, Physical Review Letters, 107 (2011).

[6] W. B. Atwood et al., *The Large Area telescope on the Fermi Gamma-Ray Space Telescope mission*, The Astrophysical Journal, 697 (2009), p. 1071.

[7] D. Balin and A. Love, *Supersymmetric Gauge Field Theory and String Theory*, Taylor & Francis, 1996.

[8] R. Barbieri, L. J. Hall, and V. S. Rychkov, *Improved naturalness with a heavy higgs boson: An alternative road to CERN LHC physics*, Physical Review D, 74 (2006), p. 015007.

[9] L. Bergström, *Non-baryonic dark matter: observartional evidence and detection methods*, Reports on Progress in Physics, 63 (2000), pp. 793–841.

[10] J. M. Bernardo and A. F. M. Smith, *Bayesian Theory*, John Wiley and Sons, 1994.

[11] G. Bertone, D. Hooper, and J. Silk, *Particle dark matter: evidence, candidates and constraints*, Physics Reports, 405 (2005), pp. 279–390.

[12] W. Bolstad, *Introduction to Bayesian Statistics*, John Wiley and Sons, 2007.

[13] O. Brein, *Adaptive scanning - a proposal how to scan theoretical predictions over a multi-dimensional parameter space efficiently*, Computer Physics Communications, 170 (2004), pp. 42–48.

[14] C. Burgess and G. Moore, *The Standard Model: A Primer*, Cambridge University Press, 2007.

[15] D. J. H. Chung, L. L. Everett, G. L. Kane, S. F. King, J. Lykken, and L.-T. Wang, *The soft supersymmetry-breaking lagrangian: theory and applications*, Physics Reports, 407 (2005), pp. 1–203.

[16] D. Clowe, M. Bradač, A. H. Gonzalez, M. Markevitch, S. W. Randall, C. Jones, and D. Zaritsky, *A direct empirical proof of the existence of dark matter*, The Astrophysical Journal Letters, 648 (2006), p. L109.

[17] M. Colless et al., *The 2df galaxy redshift survey: Spectra and redshifts*, Monthly Notices of the Royal Astronomical Society, 328 (2001), pp. 1039–1063. cited By (since 1996) 863.

[18] P. Congdon, *Bayesian Statistical Modelling*, John Wiley and Sons, 2006.

[19] R. C. Cotta, K. T. K. Howe, J. L. Hewett, and T. G. Rizzo, *Phenomenological minimal supersymmetric standard model dark matter searches on ice*, Physical Review D, 85 (2012).

[20] G. D'Agostini, *Probability and measurement uncertainty in physics - a Bayesian primer*, arXiv:hep-ph/9512295v2, (1995).

[21] B. de Finetti, *Theory of Probability*, John Wiley and Sons, 1974.

[22] G. Degrassi, S. Heinemeyer, W. Hollik, P. Slavich, and G. Weiglein, *Towards high-precision predictions for the mssm higgs sector*, European Physics Journal C, 28 (2003), pp. 133–143.

[23] M. Drees, M. M. Nojiri, D. P. Roy, and Y. Yamada, *Light higgsino dark matter*, Physical Review D, 56 (1997), pp. 276–290.

[24] J. Einasto, *Dark matter*, arXiv:astro-ph/09010632v2, (2010).

[25] J. Ellis, K. A. Olive, C. Savage, and V. C. Spanos, *Neutrino fluxes from constrained minimal supersymmetric standard model lightest supersymmetric particle annihilations in the Sun*, Physical Review D, 81 (2010), p. 085004.

[26] R. K. Ellis, W. J. Stirling, and B. R. Webber, *QCD and Collider Physics*, Cambridge University Press, 2003.

[27] T. Falk, K. A. Olive, and M. Srednicki, *Heavy sneutrinos as dark matter*, Physics Letters B, 339 (1994), pp. 248–251.

[28] M. Felizardo, T. Girard, T. Morlat, A. Fernandes, F. Giuliani, et al., *Final analysis and results of the Phase II SIMPLE dark matter search*, arXiv:astro-ph/11063014, (2011).

[29] M. Felizardo, T. Morlat, A. C. Fernandes, T. A. Girard, J. G. Marques, A. R. Ramos, M. Auguste, D. Boyer, A. Cavaillou, C. Sudre, J. Poupeney, R. F. Payne, H. S. Miley, and J. Puibasset, *First results of the Phase II SIMPLE dark matter search*, Phys. Rev. Lett., 105 (2010), p. 211301.

[30] F. Feroz, M. Hobson, and M. Bridges, *Multinest: An efficient and robust bayesian inference tool for cosmology and particle physics*, Monthly Notices of the Royal Astronomical Society, 398 (2009), pp. 1601–1614.

[31] J. P. Filippini, *A Search for WIMP Dark Matter Using the First Five-Tower Run of the Cryogenic Dark Matter Search*, PhD thesis, University of California, Berkeley, 2008.

[32] C. Forbes, M. Evans, N. Hastings, and B. Peacock, *Statistical Distributions*, John Wiley and Sons, 2011.

[33] M. Frank, T. Hahn, S. Heinemeyer, W. Hollik, H. Rzehak, and G. Weiglein, *The higgs boson masses and mixing of the complex MSSM in the feynman-diagrammatic approach*, Journal of High Energy Physics, 2007 (2007), p. 047.

[34] R. Gaitskell, V. Mandic, and J. P. Filippini, *DMToolsBeta database*. http://dmtools.brown.edu:8080/session/new.

[35] T. Girard, F. Giuliani, T. Morlat, M. F. da Costa, J. Collar, C. Limagne, G. Waysand, J. Puibasset, H. Miley, M. Auguste, D. Boyer, A. Cavaillou, J. Marques, C. Oliveira, A. Fernandes, A. Ramos, and R. Martins, *SIMPLE dark matter search results*, Physics Letters B, 621 (2005), pp. 233 – 238.

[36] C. Giunti and C. W. Kim, *Fundamentals of Neutrino Physics and Astrophysics*, Oxford University Press, 2007.

[37] P. Gondolo, J. Edsjö, L. Bergström, P. Ullio, M. Schelke, E. A. Baltz, T. Bringmann, and G. Duda, *DarkSUSY: Manual and long description of routines*, 2009.

[38] P. Gondolo, J. Edsjö, P. Ullio, L. Bergström, M. Schelke, and E. A. Baltz, *DarkSUSY: computing supersymmetric dark matter properties numerically*, Journal of Cosmology and Astroparticle Physics, 2004 (2004), pp. 145–179.

[39] A. Gould, *Resonant enhancements in weakly interacting massice particle capture by the earth*, Astrophysical Journal, 321 (1987), pp. 571–585.

[40] K. Hagiwara et al., *Review of Particle Physics*, Physical Review D, 66 (2002), p. 010001.

[41] F. Halzen and S. R. Klein, *IceCube: An instrument for neutrino astronomy*, Review of Scientific Instruments, 81 (2010), p. 081101.

[42] S. Heinemeyer, W. Hollik, and G. Weiglein, *The masses of the neutral CP-even higgs bosons in the mssm: Accurate analysis at the two-loop level*, European Physics Journal C, 9 (1999), pp. 343–366.

[43] S. Heinemeyer, W. Hollik, and G. Weiglein, *Feynhiggs: a program for the calculation of the masses of the neutral cp-even higgs bosons in the mssm*, Computer Physics Communications, 124 (2000), pp. 76–89.

[44] M. Hindmarsh and O. Philipsen, *WIMP dark matter and the QCD equation of state*, Physical Review D, 71 (2005), p. 087302.

[45] W. Hu and S. Dodelson, *Cosmic microwave background anisotropies*, Annual Review of Astronomy and Astrophysics, (2002).

[46] F. Iocco, G. Mangano, G. Miele, O. Pisanti, and P. D. Serpico, *Primordial nucleosynthesis: From precision cosmology to fundamental physics*, Physics Reports, 472 (2009).

[47] G. Jungman, M. Kamionkowski, and K. Griest, *Supersymmetric dark matter*, Physics Reports, 267 (1996), pp. 195–373.

[48] T. Junk, *Confidence level computation for combining searches with small statistics*, Nuclear Instruments and Methods in Physical Research A, 434 (1999), pp. 435–443.

[49] W. Kilian, *Electroweak Symmetry Breaking: The Bottom-Up Approach*, Springer, 2003.

[50] M. Kuroda, *Complete Lagrangian of MSSM*, arXiv:hep-ph/9902340v3, (2005).

[51] D. Larson, J. Dunkley, G. Hinshaw, E. Komatsu, M. R. Nolta, C. L. Bennet, B. Gold, M. Halpern, R. S. Hill, N. Jarosik, A. Kogut, M. Limon, S. S. Meyer, N. Odegard, L. Page, K. M. Smith, D. N. Spergel, G. S. Tucker, J. L. Weiland, E. Wollack, and E. L. Wright, *Seven-year wilkinson microwave anisotropy probe (WMAP) observations: Power spectra and WMAP-derived parameters*, Astrophysical Journal, Supplement Series, 192 (2011).

[52] V. Lebedenko, H. Araújo, E. Barnes, A. Bewick, R. Cashmore, V. Chepel, A. Currie, D. Davidge, J. Dawson, T. Durkin, B. Edwards, C. Ghag, M. Horn, A. Howard, A. Hughes, W. Jones, M. Joshi, G. Kalmus, A. Kovalenko, A. Lindote, I. Liubarsky, M. Lopes, R. Lüscher, K. Lyons, P. Majewski, A. Murphy, J. Neves, F.and Da Cunha, R. Preece, J. Quenby, P. Scovell, C. Silva, V. Solovov, N. Smith, P. Smith, V. Stekhanov, T. Sumner, C. Thorne, and R. Walker, *Limits on the spin-dependent WIMP-nucleon cross sections from the first science run of the ZEPLIN-III experiment*, Physical Review Letters, 103 (2009). cited By (since 1996) 17.

[53] A. Liddle, *An Introduction to Modern Cosmology*, John Wiley and Sons, 2004.

[54] M. Markevitch, *Chandra observation of the most interesting cluster in the universe*, arXiv:astro-ph/0511345v1, (2005).

[55] G. D. Martinez, J. S. Bullock, M. Kaplinghat, L. E. Strigari, and R. Trotta, *Indirect dark matter detection from dwarf satellites: joint expectations from astrophysics and supersymmetry*, Journal of Cosmology and Astroparticle Physics, 06 (2009).

[56] R. Massey, J. Rhodes, N. Scoville, A. Leathaud, A. Finoguenov, P. Capak, D. Bacon, H. Aussel, J. P. Kneib, A. Koekemoer, H. McCracken, B. Mobasher, S. Pires, A. Refregier, S. Sasaki, J. L. Stark, Y. Taniguchi, A. Taylor, and J. Taylor, *Dark matter maps reveal cosmic scaffolding*, Nature, 445 (2007), pp. 286–290. cited By (since 1996) 103.

[57] D. C. Montgomery and G. G. Runger, *Applied Statistics and Probability for Engineers*, John Wiley and Sons, 4 ed., 2007.

[58] V. Mukhanov, *Physical Foundations of Cosmology*, Cambridge University Press, 2005.

[59] K. Nakamura et al., *Review of particle physics*, Journal of Physics, G37 (2010).

[60] National Nuclear Data Center, *Information extracted from the NuDat 2 database*. http://www.nndc.bnl.gov/nudat2/.

[61] A. A. Penzias and R. W. Wilson, *A measurement of excess antenna temperature at 4080 Mc/s*, Astrophysical Journal, 142 (1965), pp. 419–421.

[62] W. J. Percival, B. A. Reid, D. J. Eisenstein, N. A. Bahcall, T. Budavari, J. A. Frieman, M. Fukugita, J. E. Gunn, Ž. Ivezić, G. R. Knapp, R. G. Kron, J. Loveday, R. H. Lupton, T. A. McKay, A. Meiksin, R. C. Nichol, A. C. Pope, D. J. Schlegel, D. P. Schneider, D. N. Spergel, C. Stoughton, M. A. Strauss, A. S. Szalay, M. Tegmark, M. S. Vogeley, D. H. Weinberg, D. G. York, and I. Zehavi, *Baryon acoustic oscillations in the Sloan Digital Sky Survey Data Release 7 galaxy sample*, Monthly Notices of the Royal Astronomical Society, 401 (2010), pp. 2148–2168.

[63] M. E. Peskin and D. V. Schroeder, *An Introduction to Quantum Field Theory*, Westview Press, 1995.

[64] L. Pieri, A. Pizzella, E. M. Corsini, E. Dalla Bontá, and F. Bertola, *Could the Fermi Large Area Telescope detect $\gamma$-rays from dark matter annihilation in the dward galaxies of the local group?*, Astronomy & Astrophysics, 496 (2009), pp. 351–360.

[65] W. H. Press, S. A. Teukolsky, W. T. Vetterling, and B. P. Flannery, *Numerical Recipes*, Cambridge University Press, 2007.

[66] A. G. Riess, A. V. Filippenko, P. Challis, A. Clocchiatti, A. Diercks, P. M. Garnavich, R. L. Gilliland, C. J. Hogan, S. Jha, R. P. Kirshner, B. Leibundgut, M. M. Phillips, D. Reiss, B. P. Schmidt, R. A. Schommer, R. C. Smith, J. Spyromilio, C. Stubbs, N. B. Suntzeff, and J. Tonry, *Observational Evidence from Supernovae for an Accelerating Universe and a Cosmological Constant*, Astrophysical Journal, 116 (1998), pp. 1009–1038.

[67] V. Rubin and W. K. F. Jr, *Rotation of the Andromeda nebula from a spectroscopic survey of emission regions*, Astrophysical Journal, 159 (1970), p. 379.

[68] V. Rubin, W. K. F. Jr, and N. Thonnard, *Rotational properties of 21 SC galaxies with a large range of luminosities and radii, from NGC 4605 R = 4kpc to UGC 2885 R = 122 kpc*, Astrophysical Journal, 238 (1980), pp. 471–487.

[69] P. Scott, *Searches for Particle Dark Matter*, PhD thesis, Stockholm University, 2010.

[70] P. Scott, J. Conrad, J. Edsjö, L. Bergström, C. Farnier, and Y. Akrami, *Direct constrains on minimal supersymmetry from fermi-lat observations of the dwarf galaxy segue 1*, Journal of Cosmology and Astroparticle Physics, 01 (2010).

[71] P. Scott, M. Fairbairn, and J. Edsjö, *Dark stars at the galactic centre - the main sequence*, Monthly Notices of the Royal Astronomical Society, 394 (2009), pp. 82–104.

[72] P. Scott, C. Savage, J. Edsjö, and the IceCube Collaboration, *Use of event-level neutrino telescope data in global fits for theories of new physics*, arXiv:1207.0810v1 [hep-ph], (2012).

[73] G. Servant and T. M. P. Tait, *Is the lightest Kaluza-Klein particle a viable dark matter candidate?*, Nuclear Physics B, 650 (2003), pp. 391–419.

[74] J. Silk, *Galaxy formation and dark matter*, Lecture Notes in Physics, 720 (2007), pp. 101–121.

[75] F. Stoehr, S. D. M. White, V. Springel, G. Tormen, and N. Yoshida, *Dark matter annihilations in the halo of the Milky Way*, Monthly Notices of the Royal Astronomical Society, 345 (2003), pp. 1313–1322.

[76] M. Tegmark, M. R. Blanton, M. A. Strauss, F. Hoyle, D. Schlegel, R. Scoccimarro, M. S. Vogeley, D. H. Weinberg, I. Zehavi, A. Berlind, T. Budavari, A. Connolly, D. J. Eisenstein, D. Finkbeiner, J. A. Frieman, J. E. Gunn, A. J. S. Hamilton, L. Hui, B. Jain, D. Johnston, S. Kent, H. Lin, R. Nakajima, R. C. Nichol, J. P. Ostriker, A. Pope, R. Scranton, U. Seljak, R. K. Sheth, A. Stebbins, A. S. Szalay, I. Szapudi, L. Verde, Y. Xu, J. Annis, N. A. Bahcall, J. Brinkmann, S. Burles, F. J. Castander, I. Csabai, J. Loveday, M. Doi, M. Fukugita, J. R. G. III, G. Hennessy, D. W. Hogg, Ž. Ivezić, G. R. Knapp, D. Q. Lamb, B. C. Lee, R. H. Lupton, T. A. McKay, P. Kunszt, J. A. Munn, L. O'Connell, J. Peoples, J. R. Pier, M. Richmond, C. Rockosi, D. P. Schneider, C. Stoughton, D. L. Tucker, D. E. V. Berk, B. Yanny, D. G. York, and T. S. Collaboration, *The three-dimensional power spectrum of galaxies from the sloan digital sky survey*, The Astrophysical Journal, 606 (2004), p. 702.

[77] The IceCube Collaboration, *IceCube preliminary design document*, October 2001.

[78] R. Trotta, R. R. de Austri, and C. P. de los Heros, *Prospects for dark matter detection with IceCube in the context of the CMSSM*, Journal of Cosmology and Astroparticle Physics, 2009 (2009).

[79] R. Trotta, F. Feroz, M. Hobson, L. Roszkowski, and R. De Austri, *The impact of priors and observables on parameter inferences in the constrained mssm*, Journal of High Energy Physics, 2008 (2008).

[80] J. A. Tyson, G. P. Kochanski, and I. P. Dell'Antonio, *Detailed mass map of CL 0024+1654 from strong lensing*, Astrophysical Journal Letters, 498 (1998), pp. L107–L110.

[81] D. D. Wackerly, W. Mendenhall, and R. L. Scheaffer, *Mathematical Statistics with Applications*, Duxbury Press, 7 ed., 2007.

[82] S. Weinberg, *The Quantum Theory of Fields Volume III: Supersymmetry*, Cambridge University Press, 2005.

[83] C. Wiebusch, *Physics capabilities of the IceCube DeepCore detector*, Proceedings of the 31st ICRC, Łódź, (2009).

[84] G. Wikström and J. Edsjö, *Limits on the wimp-nucleon scattering cross-sections from neutrino telescopes*, Journal of Cosmology and Astroparticle Physics, 2009 (2009).

[85] D. L. Wiltshire, *Cosmic clocks, cosmis variance and cosmic averages*, New Journal of Physics, 9 (2007), p. 377.

[86] D. L. Wiltshire, *Average observational quantities in the timescape cosmology*, Physical Review D, 80 (2009), p. 123512.

[87] F. Zwicky, *Die rotvershiebung extragalaktischen nebeln*, Helvetica Physica acta, 6 (1933), pp. 110–127.

[88] F. Zwicky, *On the masses of nebulae and of clusters of nebulae*, Astrophysical Journal, 86 (1937), pp. 217–246.